IMPLEMENTING UNMANNED AERIAL SYSTEMS WITHIN A FIELD-BASED MAIZE (*Zea mays* L.) BREEDING PROGRAM: IMPROVING YIELD PREDICTION AND UNDERSTANDING TEMPORAL QTL EXPRESSION OF PLANT HEIGHT

A Dissertation

by

STEVEN LANGLIE ANDERSON II

Submitted to the Office of Graduate and Professional Studies of
Texas A&M University
in partial fulfillment of the requirements for the degree of

DOCTOR OF PHILOSOPHY

Chair of Committee,	Seth Murray
Committee Members,	Sorin Popescu
	Nithya Rajan
	William Rooney
Head of Department,	David D. Baltensperger

August 2019

Major Subject: Plant Breeding

ABSTRACT

Unmanned aerial system (UAS) technologies are becoming common place within field-based agriculture programs allowing breeders to evaluate greater numbers of genotypes, reducing resource inputs and maintaining unbiased data collection. A comprehensive evaluation was conducted focused on the implementation of UAS technologies within a field-based maize breeding program using the plant height phenotype as a proof of concept in implementation and validation. A robust data processing pipeline was developed to extract height measurements from RGB structure from motion (SfM) point clouds. The 95th percentile (P95) height estimates exceeded 70% correlation to manual ground truth measurements across diverse germplasm groups of hybrid (F_1) and inbred lines. Sigmoidal functions were developed to model the overall growth and trajectory of hybrids (R^2: >98%; RMSE: < 14 cm) and inbred (R^2: >99%; RMSE: < 4 cm). UAS-based height estimates demonstrated greater capacity to partition phenotypic variance to genetic components compared to manual measurements; function growth parameters (asymptote, inflection point, and growth rate) were explained by more than 70% of variance with genetics for the hybrid trials. UAS height estimates improved correlations to hybrid grain yield >1.5-fold similar to functional growth parameters. A ~4-fold improvement in indirect selection of hybrid grain yield was achieved using functional growth parameters compared to conventional manual, terminal plant height (PHT_{TRML}). We expanded our implementation of UAS phenotyping to evaluate three inbred line mapping populations aimed at studying functional QTL and temporal QTL expression. Functional growth parameters identified 34 associations explaining 3 to 15% genetic variation. Height was estimated at one-day

intervals to 85 DAS using the Weibull function, identifying 58 unique temporal peak QTL locations. Temporal QTL demonstrated all of the identified significant QTL had dynamic expression patterns. In all, UAS technologies improved phenotypic selection accuracy and have capacity to monitor traits on a temporal scale furthering our understanding of crop development and biological trajectories.

DEDICATION

To my girlfriend Lauren for showing me love, support, patience, and understanding while I follow my passion. Also to my parents, Steve and Wanda, and brother, Jason, for supporting me through all life's endeavors and giving me encouragement to follow my dreams. To my grandmother, Violet Pariseau, and aunts, Jane and Brenda Pariseau, whom have passed, thank you for your support and encouragement throughout my pursuit of my higher education.

ACKNOWLEDGEMENTS

I would like to thank my committee chair, Dr. Seth Murray, for providing me with the opportunity to pursue my graduate education and for the countless times he has challenged me to try new methods and learn alternative techniques to improve my personal and scientific mindset. Thanks are needed for my committee members, Dr. William Rooney, Dr. Sorin Pospescu, and Dr. Nithya Rajan for advising me through my research and providing answers to my questions. Dr. Rooney has been instrumental in graduate development providing insight into challenging research question. Dr. Rooney has pushed me to critically think about why my research is important and how it can directly benefit a breeding program. If it were not for Dr. Popescue's knowledge and remote sensing resources in the field of unmanned aerial systems this research would not have been possible. Dr. Rajan's knowledge of crop physiology coupled with remote sensing has been instrumental in my research. I owe a great deal of gratitude to my committee; as their guidance has helped me complete my dissertation, as well as, my doctoral education.

There were many graduate students who have helped me over the past three years, Dr. Adam Mahan for being a friend and mentor during my graduate studies and Dr. Yuanyuan Chen for developing the mapping populations critical to my research. Additionally I would like to thank the graduate students for their assistance in many aspects of my research: Dr. Nancy Wahl, Colby Ratcliff, Holly Lane, Shakirah Nakasagga, Alper Adak, Nathalia Penna Cruzato, David Horne, Dr. N. Ace Pugh, Dr. Fabian Echeverria, Nolan Bently, and Grant Richardson.

To our former research technician, Jacob Pekar, thank you for all you have done to assist in my field trials; your knowledge of agronomy and long hours planting, spraying and irrigating my trials are greatly appreciated. Thank you for being a great friend and for questioning everything I say to you in a respectful manner. David Rooney it was a pleasure sharing an office space with you and thank you for your knowledge and invaluable experience as our research technician. Thank you above all else for your continual positive attitude. Additionally, Dr. Scott Wilde for your technical support.

My research would not be possible without the foundation framework set forth by the unmanned aerial systems project for precision agriculture and high throughput field phenotyping through Texas A&M AgriLife Research. Specifically, Mrs. Misty Miles for her excellent management of such a large collaborative project and her willingness to always lend a helping hand. Thank you to Dr. Dale Cope's program, specifically Ian Gates and Andrew Vree for conducting the Tuffwing UAS surveys of my trials in 2017. Dr. Jinhu Jung and Dr. Anjin Chang for your expertise in image processing and the development of the UASHub. A special thank you to Dr. Lonesome Malambo for your years of dedication to the UAS projects, conducting weekly UAS surveys and countless hours of image processing. Dr. Malambo was a great mentor and bank of knowledge throughout my journey into the remote sensing research field.

I have had the fortune of being assisted by many great undergraduate student workers. Their assistance, when asked, was greatly appreciated, especially during backpack spraying and note taking times while trudging through the mud. Thank you to Daniel Hillin, Anthony Grassia, Amee R. Bumguardner, Jeremy Garrett, Brett Wheeler, Chase Grey, Cord Wieghat, Dakota Freund, Marvin Wirianto, Caitlin Lakey, Clarissa Conrad, Devin Deluca,

Kyle Dunk, Regan Lindsey, Ya nan “Susie” Lin, Raul Ramirez, Dalton Askew, Aubrey Gilbert, Colton Russell, Mackenzie Arlene, Malik Williams, Johnathan Keck, Josiah Keck, and Grace Keck for putting up with me during the summer/winter seasons and assisting in my research.

Of course, none of my graduate research or education would be possible without financial contributions. Thank you to the Texas A&M University Soil and Crop Sciences department and Texas AgriLife Research for funding my tuition and stipend. Thank you to the Eugene Butler Endowed Chair for Agricultural Biotechnology, Department of Soil and Crop Sciences, Texas A&M AgriLife Research, The Texas Corn Producers Board, USDA-NIFA-HATCH Funds, and the USDA-NIFA-AFRI Award No. 2017-67013-26185 for funding this research. Thank you to the Texas A&M College of Agriculture and Life Sciences for the Tom Slick Senior Graduate Fellowship.

Lastly, thanks to my parents and extended family that I am blessed to be a part of for their thoughts and support that has kept me motivated and determined to obtain my graduate education. Thank you to my lovely girlfriend, Lauren for all of your love, support and positivity while we pursue our graduate educations together.

CONTRIBUTORS AND FUNDING SOURCES

Contributors

Faculty Committee Recognition

This work was supervised by a dissertation committee consisting of Associate Professor Dr. Seth Murray [advisor], Professor Dr. William Rooney, and Associate Professor Dr. Nithya Rajan of the Department of Soil and Crop Sciences and Professor Dr. Sorin Popescu of the Department of Ecosystem Science and Management.

Student/Collaborator Contributions

All of the data presented in the dissertation from rotary wing platform was collected and processed Dr. Popescu Lab, specifically Dr. Lonesome Malabo and Tanner Perkins. All of the image data presented in the dissertation from fixed wing platform was collected by Associate Professor of Practice Dr. Dale Cope's Lab in the Department of Mechanical Engineering, specifically Andrew Vree and Ian Gates. Fixed wing images were processed by Assistant Professor Dr. Jinha Jung and Dr. Anjin Chang at Texas A&M Corpus Christi in the School of Engineering and Computer Sciences. The ground control points used in Chapter 2 for the fixed wing flights were constructed by Professor Dr. Alex Thomasson, specifically Cody Bagnall. All other ground control points were constructed by Dalton Askew, David Horne, and Dr. N. Ace Pugh. The Genomes to Fields germplasm is a result of huge collaborative intuitive (www.genomes2fields.org) and we would like to acknowledge Professor Dr. Natalia de Leon of Agronomy and Naser Alkhalifah at The University of Wisconsin for providing the germplasm for Chapter 2. The manual measurement data analyzed for Chapter 2 was provided by Dalton Askew and Raul Ramirez.

The genetic mapping populations analyzed in Chapter 3 were developed by Dr. Yuanyuan Chen during her doctoral research at Texas A&M. Genotyping data used in Chapter 3 was provided by Dr. Ivan Barrero of Kraft Heinz Company (previously with AgReliant Genetics, LLC) and Dr. Jialiang Chen of AgReliant Genetics, LLC.

All other work conducted for the dissertation was completed by the student independently.

Funding Sources

Graduate study was supported by a fellowship from Texas A&M University Department of Soil and Crop Sciences graduate fellowship and Texas A&M AgriLife Research. A dissertation research fellowship from the Texas A&M College of Agriculture and Life Sciences for the Tom Slick Senior Graduate Fellowship.

This work was made possible, in part by USDA-NIFA-AFRI under Award No. 2017-67013-26185. Its contents are solely the responsibility of the authors and do not necessarily represent the official views of USDA-NIFA-AFRI. Additional funding sources included the Texas A&M College of Agriculture and Life Sciences Eugene Butler Endowed Chair for Agricultural Biotechnology, The Texas Corn Producers Board, and USDA-NIFA-HATCH Funds. AgReliant Genetics, LLC funded the genotyping utilized in Chapter 3.

NOMENCLATURE

AGR	Absolute growth rate
ALS	Airborne laser scanning
ATIN	Adaptive triangulated irregular network
BLUP	Best linear unbiased predictor
CSF	Cloth surface model
CSM	Crop surface model
DAS	Days after sowing
DBM	Difference based method
DEM	Digital elevation model
DG2F	Non-irrigated, optimal planting Genomes to Field trial
dQTL	Deterministic quantitative trait locus
DSM	Digital surface model
DTA	Days to anthesis
DTM	Digital terrain model
DTS	Days to silking
FW	Fixed wing
G2F	Genomes to Fields
G2FE	Irrigated, optimal planting Genomes to Field trial
G2LA	Irrigated, delayed planting Genomes to Field trial
GWAS	Genome wide association study
GxE	Genotype by environment interaction

H^2	Broad sense heritability
HCDH	High canopy density hybrid study site
HTP	High throughput phenotyping
HTTP	High throughput phenotyping platform
HRI	Hierarchical robust interpolation
ICIM	Inclusive composite interval mapping
LAHR	Low altitude, high resolution
LCDH	Low canopy density hybrid study site
LiDAR	Light detection and ranging
MCC	Multiscale curvature classification
MCDI	Medium canopy density inbred study site
MT-CSM	Multi-temporal crop surface model
nDSM	Normalized digital surface model
nlm	Non-linear modeling
oQTL	Oportunistic quantitative trait locus
P95	95^{th} percentile height estimate
PCM	Point cloud method
PHT	Plant height
PHT_{TRML}	Manual measured terminal plant height
PM	Progressive morphological filter
QTL	Quantitative trait locus
R	Repeatability
RCBD	Randomized complete block design

REML	Restricted maximum likelihood
RGB	Red, green, blue
RGR	Relative growth rate
RIL	Recombinant inbred line
RMSE	Root mean squared error
RW	Rotary wing
SfM	Structure from motion
SNP	Single nucleotide polymorphism
TLS	Terrestrial laser scanning
UAS	Unmanned aerial system
UAV	Unmanned aerial vehicle
VIF	Variance inflation factor

TABLE OF CONTENTS

Page

LIST OF FIGURES

Page

LIST OF TABLES

Page

CHAPTER I

INTRODUCTION

1.1 The Rise of Phenomics

A linear improvement of cereal grain yields has been achieved following the green revolution (Hafner, 2003) due to conventional breeding and improved agronomic practices (Duvick, 1997), however, projections of future cereal crop yields indicate that traditional approaches may be reaching a upper yield plateau (Grassini, et al., 2013). Plant scientists and agronomists are faced with the responsibility to develop germplasm and agricultural systems with the capacity to produce an additional 25-70% of current yield production in order to meet the projected increase in food and fiber demand (Hunter, et al., 2017; Tilman, et al., 2011). In order to meet production demands we must find ways to raise the genetic yield ceiling of cereal crops utilizing existing, as opposed to new, farmland (Tilman, et al., 2002) and find agricultural systems that also sustainably increase production.

Advances in next-generation DNA sequencing technologies have seen rapid improvements leading to vast genomic data availability, while phenotypic characterization is drastically lagging in scale, density, and accuracy that of genomic data in agricultural use. Due to resource demands (labor, time, etc…) involved in conventional phenotyping, most traits are acquired at one time point in the growing season leading to a limited elucidation of genomic information associated to the complexity underlying the traits of interest (Furbank and Tester, 2011). Recently, advances in technologies including computer processing, robotics, imaging software, unmanned vehicles and sensors have facilitated the development of high-throughput phenotyping platforms (HTPP) to combat the phenotypic bottleneck

(Araus and Cairns, 2014). These perpetually improving HTPPs will help bridge the phenotype-to-genotype gap critically necessary to make the required gains in crop improvement.

To date, field-based ground and aerial platforms have been developed to conduct non-invasive, dynamic HTPP implementing a diverse group of sensors including VIS-NIR, spectroradiometry (multi- and hyper-spectral imaging), conventional digital photography (RGB), infrared thermometry (thermal imagery), and light detection and ranging (LiDAR); which have been discussed in regards to agricultural applications (Araus and Cairns, 2014; Deery, et al., 2014; Lin, 2015; Perez-Sanz, et al., 2017; Prashar and Jones, 2014; White, et al., 2012; Yang, et al., 2017). Currently, low-altitude, high-resolution unmanned aerial imaging systems (LAHR-UAS), including rotary wing and fixed wings aircrafts, are being more widely used in addressing several issues of ground-based HTTP including: (i) non-simultaneous measurement of different plots, (ii) soil compaction, (iii) vibration due to terrain, (iv) plant damage and (v) wet soil inhibiting field entrance and resulting in excessive soil compaction (Sankaran, et al., 2015; White, et al., 2012).

1.2 Multi-Temporal Crop Surface Models

Although plant height is a key indicator of plant growth and biomass and is easily collected manually via measurement sticks/tapes, it is time consuming, laborious, and prone to subjectivity; because of this, height measurements are nearly always collected only at the end of the growing season prior to harvest. Remote sensing should make collection of height throughout the season less labor intensive. The state of the art procedure used for estimates of large-scale canopy/plant height through remote sensing techniques is to produce of crop surface models (CSM) (Bendig, et al., 2013) or normalized digital surface models (nDSM)

(Granshaw, 2016); calculated as the difference between the digital surface model (DSM) and digital elevation model (DEM). The concept of multi-temporal CSM (MT-CSM) was introduced by Hoffmeister, et al. (2010) with a terrestrial laser scanner (TLS) for monitoring plant growth patterns across physiological development of sugar beets. Vertical structure information (i.e. point clouds) of vegetation canopies can be quantified using laser scanning approaches as a terrestrial laser scanning (TLS) (Hoffmeister, et al., 2010; Keightley and Bawden, 2010; Lumme, et al., 2008; Tilly, et al., 2014; Tilly, et al., 2012) and airborne laser scanning (ALS) (Gao, et al., 2015; Li, et al., 2015). Although ALS is capable of a greater spatial detection range, during early crop growth stages in a crop such as maize, vertical laser pulse resolution may be large in comparison to actual plant height (Li, et al., 2015); therefore, TLS is better suited for monitoring short crops in early growth stages (Hofle, 2014).

Applications of multi-temporal growth modeling have been adopted as a new technology in LAHR-UAS platforms due to their relatively low cost, high flexibility, high temporal range with respect to TLS, and an ability to fly at low altitudes without endangering human wellbeing compared with ALS (Geipel, et al., 2014; Li, et al., 2016; Link, et al., 2013). UAS-derived CSM data is collected, via an RGB camera, in the form of stereo images. Stereo images enable a 3D reconstruction of the topographic geometry, accomplished based on Structure-from-Motion (SfM) photogrammetry methods (Westoby, et al., 2012). Bendig, et al. (2013) demonstrated the transferability of Hoffmeister, et al. (2010) TLS based multi-temporal CSMs to a UAS platform. Accuracy comparisons between SfM UAS- and TLS-derived height estimates have routinely been found to be comparable, explaining ~90% of the manual height measurement variation (Bareth, et al., 2016; Bendig,

et al., 2013; Bendig, et al., 2014; Malambo, et al., 2018; Tilly, et al., 2014) . However, UAS-derived height estimates have been found to consistently underestimate height measurement in barley (Aasen, et al., 2015; Bareth, et al., 2016; Bendig, et al., 2013; Bendig, et al., 2014), maize (Malambo, et al., 2018) ,wheat (Holman, et al., 2016), rice (Willkomm, et al., 2016), sugar cane (De Souza, et al., 2017), and sorghum (Pugh, et al., 2018; Watanabe, et al., 2017).

1.3 Sigmoidal Growth Function

Multi-temporal models are a great resource to plant scientists, UAVs allow for consistent monitoring of growth throughout the plants life span at independent time points. Although MT-CSM allow analysis of the extracted phenomic data, they do not model the growth patterns in a way that can be implemented for predictive purposes, for this regression modeling remains the most appropriate tool. Traditional analysis of plant growth stems from linear regression, assuming constant relative (RGR) and absolute (AGR) growth rates. Nonlinear modeling (nlm) of growth provides a flexible, parsimonious alternative to linear models to accommodating temporal growth variation (Paine, et al., 2012). Once nlm parameters are defined, it is possible to predict growth at any time point within the growth period, whereas, MT-CSM are limited to discrete time points. Furthermore, sigmoidal models (e.g. logistical, beta, etc.) provide unique parameters (e.g. AGR, inflection points, etc.) for understanding growth variations and are commonly applied to model plant growth (Miguez, et al., 2008; Muraya, et al., 2017; Wardhani and Kusumastuti, 2013). Using MT-CSM, fitting sigmoidal functions will enable exploration of maize growth patterns through the growing season in a field-based environment.

1.4 Maize Height and QTL Mapping

Maize (*Zea mays* L.) has been adapted to be grown from tropical to temperate climates, now making it the second largest cultivated crop in the world after wheat (FAO, 2016). The maize genome is twice the size of is closest living relative sorghum (*Sorghum bicolor* L.*)* consisting of ten chromosomes. Maize is a paleopolyploid (Schnable and Freeling, 2011; Woodhouse, et al., 2010) with a medium-sized genome consisting of ~85% long terminal repeats (Huang, et al., 2012). The first genome (B73 RefGen_v1) was sequenced based on Sanger sequencing using the shotgun approach resulting in an assembly 2048 Mbp in length with 32,540 high-confidence protein-coding genes (Schnable, et al., 2009). The most resent assembly (B73 RefGen_v4) was based on PacBio sequencing and high-resolution optical mapping resulting and is considered the most accurate assembly to date. B73 RefGen_v4 is 2,106 Mb in length of which 1268 Mb were structurally intact retrotransposons and 70% of the 39,324 protein-coding genes were annotated by full length transcripts (Jiao, et al., 2017). An estimated one third of maize genes are duplicated at multiple locations in the genome (Gaut, 2001). Maize is also an important model organism in plant biology and genomics. Vast gene duplication and high non-collinearity (Fu and Dooner, 2002; Springer and Stupar, 2007) across maize cultivars has resulted in abundant genetic diversity within the available germplasm for quantitative traits such as plant height (PHT).

The genetic variation of PHT in maize is a highly heritable trait (>90%) and can be explained by the infinitesimal model (i.e. very large numbers of small additive effect loci) with some large effect loci likely fixed during domestication and early selection (Peiffer, et al., 2014). PHT is commonly collected in maize research programs when the plants have

reached maximum growth potential, after the completion of flowering. Trends from 1930-2001 of representative U.S. corn belt hybrids of their era demonstrated no trend in reduced plant height, but rather a reduction in ear height accompanied the genetic gain grain yield (Duvick, et al., 2004; Russell, 1974). Positive correlations between plant height (as measured to tip of tassel on a representative plant) and yield have been observed (Anderson, et al., 2019; Farfan, et al., 2013; Katsvairo, et al., 2003; Machado, et al., 2002; Mallarino, et al., 1999; Yin, et al., 2011). Specifically, PHT being positively correlated to yield in TX (Anderson, et al., 2019; Farfan, et al., 2013) is likely an indication of genetic tolerance to stressed conditions, or some form of hybrid vigor, and is a favorable trait within the TX corn breeding program for yield. Identifying loci associated with PHT will aid in our understanding of underlying pathways associated with maize growth, helping to further improve maize lines for Texas environments.

To date, over 200 QTL associated with height have been reported to the Gramene QTL database (http://archive.gramene.org/qtl/) and multiple more are certainly buried within the literature. Of those PHT QTL entombed within the literature, the majority are centered on temperate genetic germplasm and evaluated in temperate U.S. environments. Inevitably, it is likely that many of the PHT QTL previously discovered will not exhibit similar expression patterns nor effect sizes within a Central Texas public maize breeding program. Furthermore, very little is known about the temporal expression of QTL throughout the growing season for dynamic quantitative traits (Sun and Wu, 2015) such as maize PHT. Improvements in HTP technologies coupled with statistical and computational techniques have made it possible to begin understanding the complexity of temporal QTL expression and the genetics controlling growth trajectories (Wu and Lin, 2006). Functional mapping

(Ma, et al., 2002) implements mathematical functions (e.g., logistic function) within QTL mapping to identify genetic regions that define the developmental trajectory of a trait. Muraya, et al. (2017) conducted univariate association mapping for maize biomass marker trait associations (MTA) across 12 time points up to 42 DAS under greenhouse conditions; discovering significant early growth MTAs where the proportion of genotypic variation explained by the MTA decreased as development progressed. Muraya, et al. (2017) identified an additional four MTA affecting growth dynamics of biomass accumulation through non-parametric functional mapping and multivariate mapping. Wang, et al. (2019) estimated PHT at four developmental stages via UAS imaging, identifying that few PHT related QTL were co-localized across developmental stages. Zhang, et al. (2017) investigated the genetic architecture of maize growth across 16 developmental time points (22-67 DAS) using a greenhouse based HTPP, identified 988 QTL across 109 quantified traits, including three QTL hotspots. To date all temporal growth QTL studies in maize have been conducted at limited time points (Wang, et al., 2019), early developmental stages (Muraya, et al., 2017), or within HTPP under greenhouse environments (Muraya, et al., 2017; Zhang, et al., 2017). Comprehensive temporal phenotyping within field-based experiments is now possible with UAS and may aid in the understanding of the genetic factors controlling growth trajectories and trajectory deviations caused by abiotic and biotic interactions.

CHAPTER II

PREDICTION OF MAIZE GRAIN YIELD BEFORE MATURITY USING IMPROVED TEMPORAL HEIGHT ESTIMATES OF UNMANNED AERIAL SYSTEMS*

2.1. Introduction

2.1.1 Maize Height and Correlation to Grain Yield

Genetic variation of terminal plant height (PHT_{TRML}) in maize (*Zea mays* L.) is a highly heritable trait (Anderson, et al., 2018; Li, et al., 2016; Mahan, et al., 2018; Peiffer, et al., 2014; Wallace, et al., 2016), and is relatively easy to phenotype, for instance, measuring from the ground to the tip of a tassel on a representative plant. However, the labor and time required to collect data is still resource constrained and height measurements collected in maize research programs are generally taken only once, when the plants have reached maximum growth after the completion of flowering.

Plant height is valuable not only as a phenotype in and of itself, it has also been shown to be predictive of maize grain yield in some regions and environments (Katsvairo, et al., 2003; Machado, et al., 2002; Mallarino, et al., 1999; Yin, et al., 2011). Farfan, et al. (2013) observed positive correlations (r = 0.46) between PHT_{TRML} and grain yield within the semi-arid stressed environment of Texas, less correlation (r = 0.19) in the irrigated High Plains, and the highest correlations by combining all Texas environments (r=0.61).

*Reprinted with permission from Prediction of Maize Grain Yield Before Maturity Using Improved Temporal Height Estimates of Unmanned Aerial Systems by Anderson, S.L., Murray, S.C., Malambo, L., Ratcliff, C., Popescu, S., Cope, D., Jung, J., Chang, A., and Thomasson, J.A. 2019. The Plant Phenome Journal, 2:190004, doi: 10.2135/tppj2019.02.0004. Plant Phenome J. 2:190004 (2019) doi:10.2135/tppj2017.02.0004.

Yin, et al. (2011) demonstrated that V10/V12 plant height was highly predictive (R^2=0.26-0.87) of grain yield using an exponential regression model. Previous work has shown that early season plant height can be decoupled from PHT_{TRML} and has been hypothesized to offer additional insight into yield (Mallarino, et al., 1999; Pugh, et al., 2018). The relative ease of plant height measurements via remote sensing in the field (Chang, et al., 2017; Chu, et al., 2018; Han, et al., 2018; Malambo, et al., 2018), and the potential to predict yield at earlier time points (i.e., before harvest) makes plant height an excellent case study for phenotypic data collection via unmanned aerial systems.

Unmanned aerial systems (UAS) include unmanned aerial vehicles (UAV) that have been equipped with light detection and ranging (LiDAR) sensors to generate dense three dimensional (3D) point clouds (Wallace, et al., 2012) or more commonly digital RGB/multispectral cameras (Araus and Kefauver, 2018; Hunt Jr and Daughtry, 2017; Sankaran, et al., 2015) to collect high resolution images and 3D point clouds through post-processing of image sets. Specifically, point clouds have been used to estimate above ground heights of objects and vegetation. Aerial laser scanning technology (i.e., LiDAR) has been a major source of three dimensional data sets via manned aerial vehicles, but is very expensive. New innovations including low cost UAS (Reynolds, et al., 2018; Sankaran, et al., 2015; Shi, et al., 2016), optimized image matching software, and graphical processing units (GPUs) have reduced the inefficiency of image based photogrammetry methods (3D vision) that existed in previous decades (Baltsavias, 1999). The cost and difficulty of LiDAR-UAS system integration (Wallace, et al., 2012) has led to broad adoption of multispectral- and RGB-UAS systems (3D vision UAS) to easily and rapidly produce temporal 3D datasets in agriculture using structure from motion (SfM) photogrammetry

(Burkart, et al., 2018; Holman, et al., 2016; Malambo, et al., 2018; Pugh, et al., 2018; Xavier, et al., 2017).

2.1.2 Ground Filtering and Separation Approaches

A critical step in estimating above ground heights from UAS is the identification of ground points and accurate reconstruction of the digital terrain models (DTM) to produce digital surface models (DSM) from the digital elevation model (DEM). Ground filtering algorithms have been developed to delineate between points belonging to ground and non-ground classes and have been extensively reviewed, but the field has been dominated by LiDAR efforts in regards to urban and forested terrains (Chen, et al., 2017; Korzeniowska, et al., 2014; Meng, et al., 2010; Pfeifer and Mandlburger, 2009; Polat and Uysal, 2015; Serifoglu Yilmaz and Gungor, 2016; Sithole and Vosselman, 2004; Weed, et al., 2002) with little focus on agricultural crop land. Among comparative ground filter studies, Montealegre, et al. (2015) specifically discussed areas covered with cereal crops, concluding that an adaptive triangulated irregular network (ATIN) (Axelsson, 2000) resulted in the most accurate modeling of the terrain within crop/grasslands dominated study areas. Crop heights are commonly estimated using the "difference based method" (DBM) in which DTMs are modeled by pre- or post-season bare earth images (Bareth, et al., 2016; Bendig, et al., 2013; Chu, et al., 2018; Watanabe, et al., 2017). Alternatively, the "point cloud method" identifies ground points within each digital surface model (DSM) and creates an independent DTM for each data set (Malambo, et al., 2018; Pugh, et al., 2018). Holman, et al. (2016) demonstrated that the point cloud method produces reduced root mean square error (RMSE) compared to the DBM due to biased ground representation of the pre/post flight ground model. Correct ground modeling is essential to improving estimation accuracy, so further

studies are necessary to evaluate the most effective technique to model the terrain specific to using SfM photogrammetry from high resolution UAS images of a breeding or genetic field trial.

2.1.3 Estimating Maize Height via UAS

Common trends have been demonstrated in past UAS field studies using 3D vision SfM height. Statistical metrics of UAS point clouds have been shown to be significantly correlated to manual phenotyping and LiDAR datasets in maize (Chu, et al., 2018; Hu, et al., 2018; Li, et al., 2016; Malambo, et al., 2018; Niu, et al., 2018; Pugh, et al., 2018; Shi, et al., 2016; Varela, et al., 2017). In many of these studies, plot level point clouds were divided into quartiles with the 99th (P99) percentile including the top of the plant and the bottom 1% (P01) representing soil and above ground roots. Niu, et al. (2018) demonstrated that the use of higher quantile percentage reduced bias and RMSE in reference to LiDAR data. Similarly, UAS derived heights at the higher percentiles commonly found at P95 and P99 in maize, but excluding the P100/maximum, have shown the greatest correlation to manual plant height measurements and least RMSE (Chu, et al., 2018; Malambo, et al., 2018; Pugh, et al., 2018; van der Voort, 2016). UAS derived height estimates are highly repeatable (R = 0.91–0.99 for P95) and capable of capturing equivalent genotypic variation to manual height measurements; especially at later dates (>50 DAS) in the growing season as greater variability is expressed across genotypes (Pugh, et al., 2018).

Using high throughput technologies such as UAS and ground vehicles is rapidly becoming commonplace in agriculture and breeding programs. The majority of the published research has been focused on validation of UAS measurement to manual phenotyping and it is evident in the literature that UAS derived phenotypes provide highly accurate

measurements, highly correlated to manual phenotyping data. The focus of this study was to expand beyond validation of UAS estimated heights toward using of data as it is presented (i.e. without validation). The objectives of this study were to (i) compare multiple methods of ground point filtering for DSM accuracy, (ii) identify sources of variation across UAS platforms and environmental treatments throughout the growing season, (iii) apply nonlinear modeling approaches to identify critical flight dates and capture new growth parameters, and (iv) evaluate UAS height estimates and nonlinear modeling parameters for their ability predict grain yield in maize. To conduct this work efficiently, an improved method was needed to increase the speed of extracting plot information of large studies in the UAS to knowledge pipeline; a novel plot boundary delineation function to generate plot boundary ESRI shapefiles automatically given two boundary coordinates, the experimental design, and plot dimensions of the breeding field are also described here.

2.2 Materials and Methods

2.2.1 Germplasm Material and Experimental Design

The Genomes to Fields (G2F) initiative (https://www.genomes2fields.org/) is a multidisciplinary umbrella initiative aimed at understanding the genotype-by-environment interaction (GxE) of the maize genome (AlKhalifah, et al., 2018; Gage, et al., 2017). As of 2018 and beginning in 2014, the G2F collaborators have evaluated more than 94,000 field plots involving more than 1,700 hybrid varieties across 77 unique environments being conducted in 23 states and provinces in the United States and Canada. For this study, the 2017 G2F trials were evaluated and imaged via UAS in College Station, Texas. This trial was comprised of 280 unique hybrids, with 230 common hybrids across three different management environments: irrigated, optimal planting (G2FE), non-irrigated, optimal

planting (DG2F), and irrigated, delayed (~30 days) planting (G2LA). Each trial was arranged in a randomized complete block design (RCBD; 2 replicates/trial) with two row plots, 0.76 m row spacing, and 7.62 m plot lengths. The three trials were planted adjacent to each other in a single field of approximately ~1.4 hectares.

2.2.2 Ground Truth Measurements

Manual height measurements were collected on several dates (Appendix A1) throughout the growing season to assess the accuracy of the UAS height estimates. Two heights were taken during manual phenotyping: (i) the apex height which was either the erect emerging leaf (pre-flowering) or the tip of the tassel and (ii) the flat plane of the plot during vegetative growth or the flag leaf height during reproductive stages (Appendix B1a). Furthermore, manual terminal height measurements were taken on all plots at the tip of tassel height (PHT_{TRML}) after flowering was completed. Manual measurements were collected as a visual plot average by measuring a single representative plant.

2.2.3 Unmanned Aerial System Image Collection

Two platforms were used, a rotary wing and a fixed wing UAV. The rotary wing model, a DJI Phantom 3 Professional with a 12 megapixel DJI FC300X camera, was flown at an altitude of 25 m above the ground surface with an 80% forward and side image overlap. Fixed wing images were collected with a Tuffwing UAV Mapper (http://www.tuffwing.com) equipped with a 24 megapixel Sony a6000 RGB camera. Fixed wing surveys were conducted at a 120 m altitude with 80% image overlap. The goal was to collect weekly UAS imagery throughout the early growing season and transition to biweekly flights on a 3 to 4 day interval during the exponential growth phase, based on observations from earlier studies (Malambo, et al., 2018; Pugh, et al., 2018). Twenty-two and nineteen

flights were completed throughout the 2017 growing season by the rotary wing and fixed wing platforms, respectively (Appendix A1).

2.2.4 Image Processing

All UAS images were processed using SfM photogrammetry algorithms in either the Pix4Dmapper (https://www.pix4d.com) or Agisoft PhotoScan Professional (AgiSoft PhotoScan Professional, 2016) software. In general, these software packages are equivalent and used to identify common features (tie points) across images followed by triangulation and distortion adjustment optimization to generate densified 3D point clouds, DSM, and orthomosaic images. Due to the large collaborative effort of this project, the preference of the software was based upon each group's (fixed wing or rotary wing) capability and familiarity. Ground control points were placed throughout the study sites to ensure correct scale, orientation and geographic location of generated outputs. All of the fixed wing flights were processed in Agisoft PhotoScan, while the majority of the rotary wing flights were processed in Pix4Dmapper (excluding flights on 07-14-17 and 07-27-17). Issues with image matching and tie point identification during stages of canopy closure resulted in large "black holes" within the center of some rotary wing flight image mosaics. In an attempt to resolve the holes of missing data, Agisoft Photoscan was used in those mosaics with holes and resulted in improved data for some dates (07-14-17 and 07-27-17). Where Agisoft Photoscan did not improve the data quality, manual tie point assignment was performed.

2.2.5 Data Extraction Pipeline

Following the initial processing of raw images into point clouds, a novel processing pipeline was developed to acquire plot based height estimates from the point clouds (Figure 1A). R/UAStools::plotshpcreate (https://github.com/andersst91/UAStools) was developed

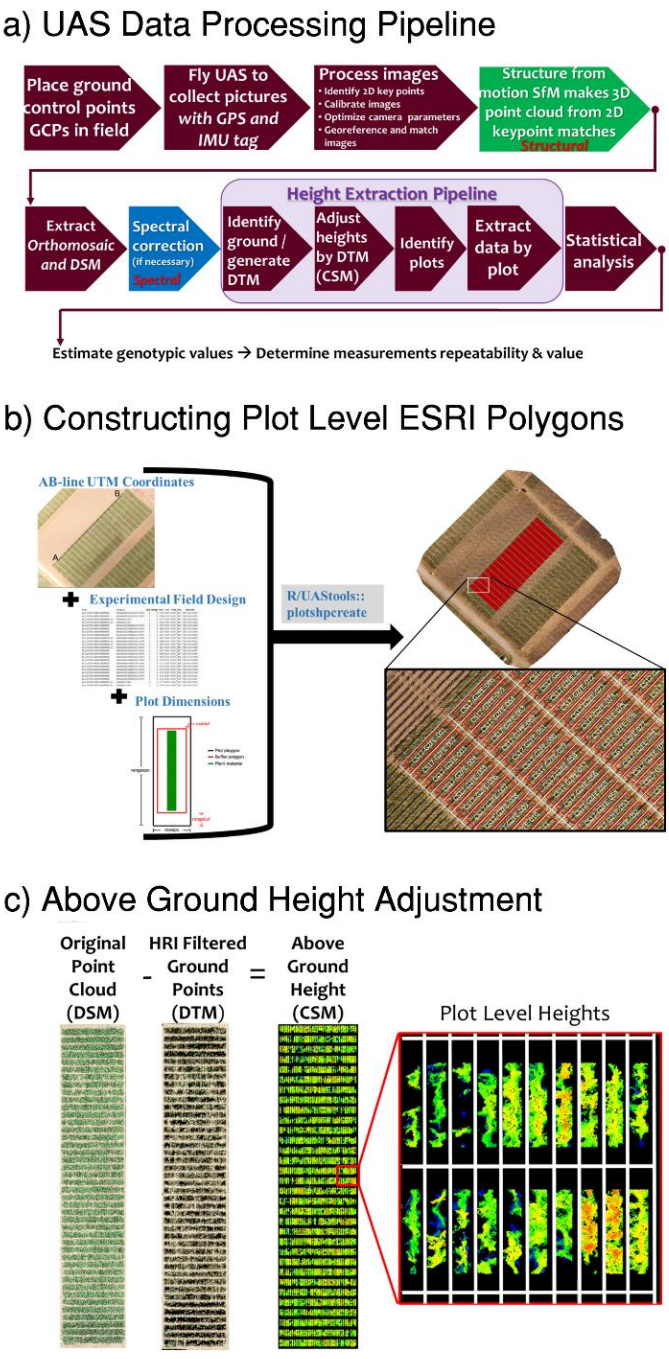

Figure 1. [a] Flow chart depicting UAS data curation pipeline from image acquisition to statistical analysis of phenotype estimates. **[b]** Graphical representation of the R/UAStools::plotshpcreate inputs and plot level polygon ESRI shapefile output. **[c]** Visual conversion of DSM to above ground canopy surface models using digital terrain modeling via hierarchical robust interpolation

to constructs ESRI shapefiles (.shp) of individual research plots for subsequent plot extraction (Figure 1B). The initial assignment of these plots is based on the GPS coordinates of an AB line representing the bottom left corner of the first plot (A) and the top left corner tool in CloudCompare v2.10 (Girardeau-Montaut, 2016). Following manual blunder of the trial within the same row as the A point (B). Using a data frame containing the experimental design, plot dimensions, and unique plot IDs, (i.e. a research 'fieldbook') the script produces an ESRI shapefile that contains all of the plot boundaries necessary to extract plot level measurements. However, we have found that some manual adjustment is needed when visually overlaid on the mosaics due to subtle variances in tractor rows (even when GPS guided) and in the orthomosaics that are exaggerated when overlaying a precise rectangular grid.

The point clouds were first clipped to the trial level and large blunders (i.e. serendipitous point anomalies above/below the point cloud) were manually removed using the segment removal, a custom batch script was run including executable functions from LAStools (Isenburg, 2015; LAStools, 2017) and FUSION/LDV (McGaughey, 2016) software (https://github.com/andersst91/UAS_Height_Pipeline). In brief, the pipeline (i) sorted data points (LAStools\lasssort.exe) to improve processing efficiency, (ii) removed additional blunders (LAStools\lasnoise.exe) closer to the canopy structure, (iii) executed a ground filtering algorithm (FUSION\GroundFilter.exe) to identify ground points, (iv) identified key points (LAStools\lasthin.exe) on the vertex of the hills from the ground filter for DTM modeling, and (v) interpolated/constructed the DTM from the key points (FUSION\GridSurfaceCreate.exe). Following the DTM construction, (vi) the noise filtered point cloud (step ii output) was adjusted to above ground height using the DTM

(LAStools\lasheight.exe) and points below the DEM (i.e. ground) were removed as to not bias the height estimates with negative values (Figure 1C). Using the adjusted "Z" point cloud, the plot level ESRI shapefile was used to clip individual plot point clouds (FUSION/PolyClipData.exe) and calculate statistical metrics within each of the plots (FUSION/CloudMetrics.exe) including estimating height from the point clouds. Further data compiling and processing was conducted in R version 3.3.1 (R Core Team, 2016). All manually collected and extracted phenotypes from this study are publicly available from the Dryad Digital Repository: https://doi.org/10.5061/dryad.3295k54.

2.2.6 Comparison of Terrain Modeling Methods

2.2.6.1 Study Areas

Three flight dates were first chosen for the purpose of comparing ground filtering algorithms based on available manual height measurements and the collection of images from both UAS platforms (Appendix B2). The first site (G2LA 05/09/2017) was characterized with low canopy density, high ground point representation, and young (33 DAS) hybrid maize plants: the "low canopy density hybrid" (LCDH) site. The second site (G2LA 06/02/2017) was characterized with full canopy closure, minimal ground point representation, and mature (57 DAS) hybrid maize plants: the "high canopy density hybrid" (HCDH) site. The third site (YYCP 05/24/2017) was characterized with medium canopy density, medium ground point representation, and young vegetative (61 DAS) inbred maize plants: the "medium canopy density inbred" (MCDI) site. The MCDI study site was separate from G2F consisting of 533 plots from three bi-parental recombinant inbred line mapping populations; these plots provide a useful contrast to address other common research needs (e.g. new line development, QTL mapping, and trait discovery).

2.2.6.2 Terrain Modeling Methods

The DBM of terrain modeling was compared with more advanced point cloud methods commonly used with LiDAR data. The DBM relies on a pre-season (i.e. pre-plant) or post-season flight of the bare ground to model the terrain. This terrain model is then subtracted from the DSMs in-season to obtain CSM (Appendix B1b). The point cloud based methods are algorithms which work iteratively through point clouds of each flight and identify ground points based on classification tuning parameters that the user sets. Three point cloud methods were selected for evaluation including hierarchical robust interpolation (HRI) (Kraus and Pfeifer, 1998), cloth simulation filter (CSF) (Zhang, et al., 2016), and adaptive triangulated irregular network (ATIN) (Axelsson, 2000)) based on: (i) open access software, (ii) computational efficiency, and (iii) accuracy performance as indicated in the literature. Optimized filter parameters were identified through minimization of root mean square error (RMSE) and mean absolute error (MAE) between UAS height estimates and manual ground truth measurements taken the same day as the UAS surveys. Optimized algorithm parameters were then used to compare ground filtering methods across UAS platforms and study sites. Details on the point cloud based methodology and optimized filtering parameters can be found in Appendix C1.

2.2.7 Statistical Inference

2.2.7.1 Variance Component Estimates

From the extracted point cloud derived canopy height metrics (P90, P95, P99, Max), we fit mixed linear models using residual maximum likelihood (REML) in JMP version 14.0.0 (JMP®, 2018) to define best linear unbiased predictors (BLUPs) of the hybrids by their pedigree. Models were fit on a per flight date basis by UAS platform. The individual

G2F trials were evaluated as a randomized complete block design (RCBD, Eq. 1) including spatial regression (range and row [what furrow irrigation runs down], also called row and column, respectively, where furrow irrigation is not used) with terms genotype (σ_G^2),

$$Y = \mu + \sigma_G^2 + \sigma_r^2 + \sigma_i^2 + \sigma_j^2 + \sigma_\varepsilon^2 \quad \text{Eq. [1]}$$

replicate (σ_r^2) range (σ_i^2), row (σ_j^2) and residual error (σ_ε^2). By flying all three trials within the same flight dates, we were able to evaluate the variance components of UAS plant height as a multi-environment RCDB (Eq. 2) with terms: genotype (σ_G^2), environment (σ_E^2),

$$Y = \mu + \sigma_G^2 + \sigma_E^2 + \sigma_{G*E}^2 + \sigma_{E*r}^2 + \sigma_{E*i}^2 + \sigma_{E*j}^2 + \sigma_\varepsilon^2 \quad \text{Eq. [2]}$$

genotype-by-environment interaction (σ_{G*E}^2), replicate (r) nested within environment (σ_{E*r}^2), range (i) nested within environment (σ_{E*i}^2), and row (j) nested within environment (σ_{E*j}^2).

2.2.7.2 Repeatability

Repeatability (R) estimates represent the percentage of genetic variation explained by the data compared with the experimental variation explained excluding identifiable environmental effects. Repeatability was calculated on an entry means basis similar to broad sense heritability (H^2) with the key differentiation of presence (H^2) or absence (R) of familial structure. Within environment repeatability (Eq. 3) estimates calculated on single

$$R = \frac{\sigma_G^2}{\sigma_G^2 + \sigma_\varepsilon^2/\mathrm{r}} \quad \text{Eq. [3]}$$

replicates (r). Multi-environment repeatability (Eq. 4) was calculated by expanding equation 3 to include the entry-by-environment interaction variation component (and the number of environments (E).

$$R = \frac{\sigma_G^2}{\sigma_G^2 + \sigma_{G*E}^2/\mathrm{E} + \sigma_\varepsilon^2/\mathrm{rE}} \quad \text{Eq. [4]}$$

2.2.7.3 Nonlinear Logistic Function

Implementation of nonlinear modeling was assessed to further reduce the dimensionality of the dataset of multiple flights throughout the growing season. Maize being an annual crop, we assumed that plant height should follow an asymptotic model that begins with zero at planting and concludes its lifespan with a terminal growth parameter (Archontoulis and Miguez, 2015). The three parameter logistic model (Eq. 5) best followed

$$f(x) = \frac{L}{1 + e^{-k(x - x_0)}} \quad \text{Eq. [5]}$$

these assumptions,modeling height as a function of DAS (x) with the asymptote (L; m), inflection point (x_0; DAS), and the growth rate (k; DAS^{-1}) of the fitted curve (Verhulst, 1838). The asymptote is the maximum value of the curve which represents terminal PHT. The inflection point indicates the DAS where the rate of growth is maximized. The growth rate parameter defines the steepness of the logistic curve. Logistic curves were fit using the Fit Curve tool in JMP 14 (Analyze→Specialized Modeling→Fit Curve) and parameters were

estimated on a UAS height estimates on a plot basis, as well as, on a pedigree basis using the BLUPs of the individual environment REML models (Eq. 1). Significance of the logistic parameters were evaluated using the chi squared (X^2) test ($\alpha = 0.05$, df = 1) to identify logistical curves with poor fits to UAS height estimates. Plots with a non-significant parameter fits were excluded in further analysis, as the logistical function would not accurately represent that plot/pedigree's growth model.

2.2.7.4 Stepwise Regression of Predictive Models

Forward and reverse stepwise regression were performed in JMP 14 using the "Fit Model" function to identify the most predictive UAS height parameters with respect to grain yield (tonnes per hectare, t ha^{-1}). Parameters identified by the stepwise regression procedure were then fit as continuous effects in a linear model to assess their ability to predict yield based on their coefficient of determination (R^2) and RMSE. The parameters tested for each UAS platform included three sets of predictors: (i) the logistic parameters, (ii) pedigree BLUPs by flight date, and (iii) the combination of logistic parameter and pedigree BLUPs by flight date. Predictors were removed if they were not significant in the fit model. Due to the time series nature of our dataset, collinearity between the predictor variables was evaluated using the variance inflation factor (VIF). The VIF ($1/(1-R^2)$) cutoff was set to VIF ≤ 4.0 and the variable that caused the least reduction in R^2 of the model was removed.

2.3 Results and Discussion

Extraction of informative UAS height data from SfM photogrammetry point clouds required the optimization of terrain modeling and selection of the optimal point cloud metric to be implemented within the data extraction pipeline. We first optimized the terrain modeling procedure through the comparison of four ground modeling methods (HRI, ATIN,

CSF, DBM) across three survey sites varying in canopy structure (LCDH, MCDH, HCDH) and two UAV platforms (rotary wing and fixed wing). Based on these results, comparison across UAS platforms at each flight date were made using HRI to identify sources of variation throughout the growing season. Following the comparison of UAS platforms by flight date, nonlinear logistic functions were fit to identify critical flight dates and capture new growth parameters. Finally, we evaluated UAS height estimates and nonlinear modeling parameters for their ability predict maize grain yield.

2.3.1 Optimizing Terrain Modeling and Point Cloud Metric

A subset of three flight dates (LCDH: G2LA 05/09/2017, HCDH: G2LA 06/02/2017, and MCDI: YYCP 05/24/2017*)* were chosen to evaluate terrain modeling methods and point cloud metric comparisons across different maize canopy structures to optimize the data extraction pipeline prior to processing the complete season datasets. Selection of the three flight dates was based on availability of manual height measurements while maintaining high qualitative appearance (i.e. minimal noise) from both UAS platforms all on the same date (Pugh, et al., 2018). Comparisons were made between the DBM and three point cloud methods (HRI, ATIN, CSF) to identify the optimal terrain modeling method to be implemented within the data extraction pipeline. Further comparisons were made between four point cloud metrics (P90, P95, P99, Max) to identify the most informative metric based on RMSE, MAE, percent genetic variance explained, and repeatability.

2.3.1.1 Accuracy of Ground Filtering Methods to Ground Truth Measurements

Across both UAS platforms and canopy structures all of the algorithms performed similarly (Figure 2a) when their parameters were optimized (Sithole and Vosselman, 2004),

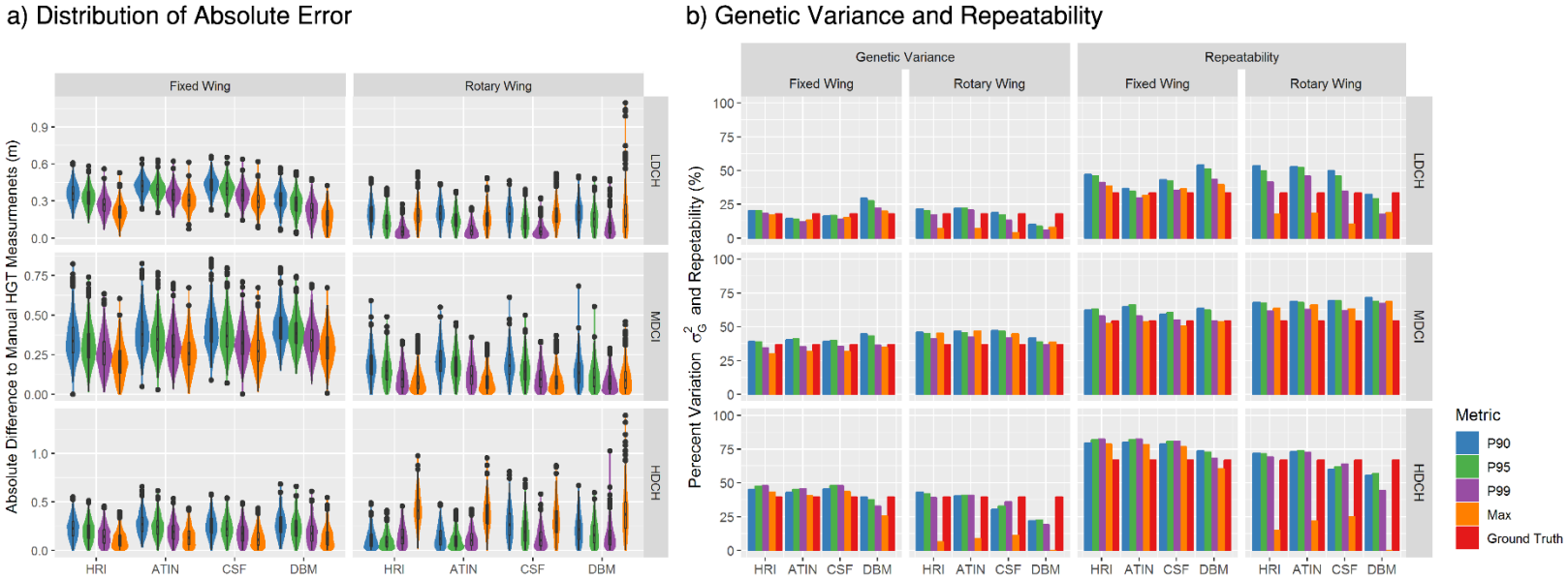

Figure 2. [a] Violin plots comparing distribution of absolute difference between UAS height metrics and ground truth measurements across UAS platforms (fixed wing and rotary wing) and study sites (LCDH: Low Canopy Density Hybrids, MCDI: Medium Canopy Density Inbred, and HCDH: High Canopy Density Hybrids) for each of the ground filtering methods (HRI: Hierarchical Robust Interpolation, ATIN: Adaptive Triangulated Irregular Network, CSF: Cloth Simulation Filter, DBM: Difference Based Method). **[b]** Comparison percent genetic variation explained (left) and repeatability (right) across UAS platforms and study sites for each of the ground filtering methods.

likely due to the relative flat plane of the study sight (irrigation furrows not withstanding) compared with the more varied natural terrain these algorithms were designed around. Across both UAS platforms, halving the resolution (fixed wing ~2 cm pixel^{-1}; rotary wing ~1 cm pixel^{-1}; Appendix A1) via fixed wing flights had a noticeable impact on the MAE (FW_{P95} 19-40 cm; RW_{P95} 10-21 cm) of the height estimates compared to ground truth (Figure 2A). The fixed wing achieved its best MAE to ground truth across the canopy structures 16, 20, and 11 cm within LDCH-DBM-Max, MDCI-HRI-Max, and HCDH-HRI-Max, respectively. The rotary wing achieved its best MAE to ground truth across the canopy structures within 6, 8, and 10 cm for LDCH-CSF-P99, MDCI-DBM-Max, and HCDH-HRI-P95, respectively. Within the LCDH and MCDI sites, the MAE of the fixed wing ranged from ~18 to ~45 cm, whereas the rotary wing ranged from ~8 to ~25 cm, dependent upon the filter method and metric.

These results demonstrated that sparse canopy structure (e.g tassels, young plants) were better captured by the low altitude rotary wing rather than the fixed wing. We hypothesize that the reduced resolution results in triangulating pixels (i.e. smoothing of the canopy structure) at lower elevations in the canopy, as well as, failure to capture less dense features at the canopy apex (e.g. tassel, erect leaf, flag leaf). In general, plant height was consistently underestimated by UAS estimates from the high altitude fixed wing and overall accuracy improved with increased crop maturity. In contrast, low altitude rotary wing transition from underestimated to overestimated heights as the metric percentile was increased, indicating increased error blunders above the canopy surface within the rotary wing datasets (Appendix B3).

2.3.1.2 Genetic Variation and Repeatability of Terrain Model Comparisons

Absolute accuracy relative to traditional manual measurements as tested above is important to validate plant height estimates. However, plant breeders (focused on selecting the best variety) and geneticists (focused on distributions for mapping) can sufficiently use and are more interested in relative rankings, genetic variation captured, and repeatability across germplasm. Genetic variation (σ^2_G) explained and repeatability (R) are two metrics that have been used to compare the precision of different point cloud percentiles (Pugh, et al., 2018), but can also be used to compare the precision of different UAS platforms, different canopy structures, and different ground filtering algorithms. Overall, both genetic variation and repeatability showed similar results between each factor individually (UAS platforms, canopy densities, ground filtering algorithms, and point cloud percentiles) when looking at only a single factor (Figure 2b), however specific interactions of these factors are notable and can inform best practices.

The P90 and P95 metrics most consistently captured the greatest genetic variation across study sites and ground filtering methods (Figure 2b); consistent with other findings using a different experiment (Pugh, et al., 2018). The P_{max} metric captured the least genetic variation and had the increased noise in low altitude flights despite showing the most consistency with the ground data (Figure 2b). The P90 and P95 metrics of the HRI and ATIN methods consistently explained greater genetic variation and repeatability than the ground truth measurements (Figure 2b; red bar) across all sites and platforms, with HRI tending to outperform ATIN. Although the DBM outperformed HRI in genetic variation and repeatability at some sites (FW-LDCH and RW-MDCI), the majority of situations result in lower genetic variation and repeatability (less desirable) in comparison to the three point

cloud based methods and lower variation than ground truth data (FW-LCDH, RW-MDCI, and FW-HDCH) (Figure 2b).

Several important discoveries were made from this comparative study for implementing UAS SfM height estimates. First, high accuracy to manual measurements did not result in genetic variation and repeatability being maximized (e.g. CSF and DBM approaches; Figure 2; Appendix B3) because the ground measurements themselves are likely flawed (biased across data curators consistency/experience phenotyping a trait of interest). Second, although specific point cloud percentiles had greater accuracy that did not always correlate to the highest repeatability/genetic variation (e.g. P99 vs P95/P90; Figure 2). Third, one of the greatest benefits of UAS height estimates was the ability to substantially improve repeatability over manual measurements. While genetic variation was improved somewhat across study sites and platforms, repeatability increased by reducing error and better partitioning spatial variance; for example the HRI method across all canopy densities and UAS platforms (R_{P95}: 50-80% and σ_G^2: 20-50%; Figure 2b) outperformed ground truth measurements (R : 30-60% and σ_G^2: 18-40%; Figure 2b) with more useful variance decomposition (Appendix B4). Finally, if adequate ground representation is available throughout the study area (alleys between plots for example) in each flight, point cloud filtering (specifically HRI) methods are a more robust alternative to the difference-based method. The HRI method was easy to optimize, robust across study sites and UAS platforms, and improved repeatability over manual measurements. Based on these results, digital terrains were modeled off ground points identifies with the HRI ground filtering method and the P95 metric was used to estimate plant height from point clouds in our data extraction pipeline for the rest of the study.

2.3.2 Comparison of UAS Platforms Across Flight Dates

2.3.2.1 Statistics of UAS Survey Flight Dates

Throughout the growing season, most UAS surveys had either no difference or one day difference between flight dates of two UAS platforms (Appendix A1). During the beginning of the growing season, minimal plant structure was captured by UAS imagery due to a sparse canopy density and a small physical size of the maize seedlings. Plant structure was not represented within the fixed wing point clouds until 48 DAS for G2FE/DG2F and 35 DAS for G2LA (later plantings have faster germination and growth) while the rotary wing first detected plant structure at 27 DAS for G2FE/DG2F and 21 DAS for G2LA (Figure 3). The early plantings (G2FE and DG2F) demonstrate that higher flight altitudes require increased canopy structure before being represented in the SfM point clouds. This 48 day delay was likely due to a 13 day gap in fixed wing flights during early growth stages (biweekly) in which the date that structure became capturable was missed. Understanding the date at which structure can be captured is important to reduce resources from UAS surveys of non-informative dates but is also critical for nonlinear modeling of growth.

The goal of increasing flights to twice weekly (every 3 to 4 d) rather than once a week, was to capture the exponential growth period of maize where a few days has been shown to make a large difference (Pugh, et al., 2018). Unfortunately, the complete exponential stage was missed for the fixed wing flights in the first plantings (G2FE and DG2E) due to limited knowledge of when this stage would begin. With the delayed planting of G2LA, surveys were collected biweekly and the exponential growth stage was captured effectively by both fixed and rotary wings (Figure 3). The fixed wing surveys of G2LA

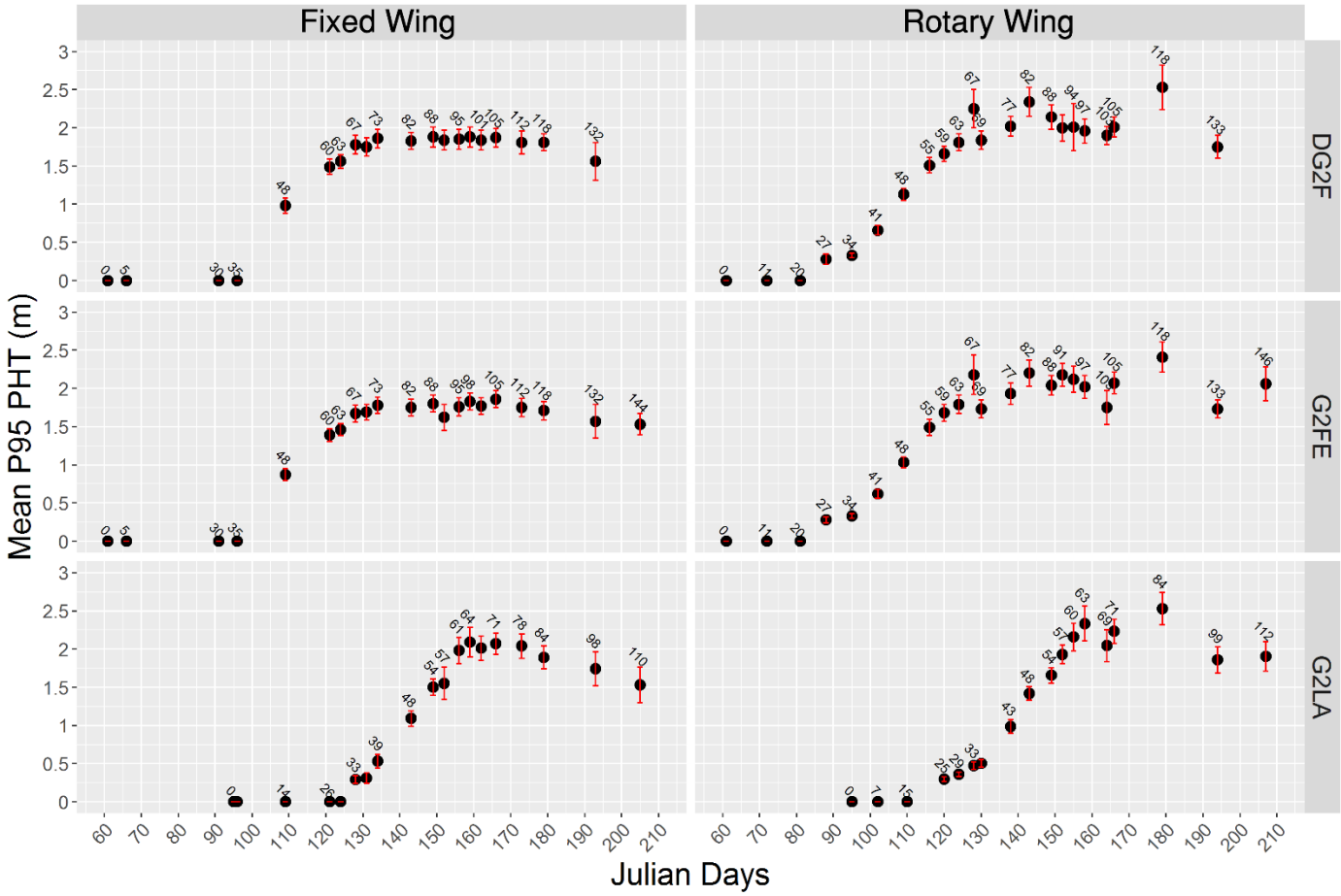

Figure 3. Mean P95 height estimate on a plot basis across the G2F trials (DG2F: Optimal planted, non-irrigated trial; G2FE: Optimal planted, irrigated trial; G2LA: Delay planted, irrigated trial) and UAS platforms (fixed wing and rotary wing). Red error bars indicate the 95% confidence intervals scaled by one order of magnitude for visualization purposes. Numbers above the confidence intervals indicate days after sowing.

captured the exponential growth stage beginning around ~35 DAS and P95 height effectively increased by ~42 cm wk^{-1} at a rate of ~6 cm d^{-1} (Appendix A2; Figure 3). Within the rotary wing surveys the exponential growth stage began around ~35 DAS and P95 height effectively increased by 37, 37, and 42 cm per week at a rate of 5, 5, and 7 cm per day across the G2FE, DG2F, and G2LA trials, respectively (Appendix A2; Figure 3). The higher resolution of the rotary wing coupled with weekly flights rather than once every two weeks, resulted in better observations of the exponential growth phase via temporal flight dates in all trials.

Analysis of temporal P95 height data indicated that a combination of survey methods should be used to successfully capture the growth patterns of maize hybrids. We have identified that weekly or fortnightly UAS surveys should begin three weeks after sowing and continue through the flowering stage to accurately model the exponential growth stage, and may require the combination of different flight altitudes based on the maturity of the trial. Early season flights should be flown at lower altitudes ($\leq$ 25 m) to increase the detection of sparse plant structure by SfM photogrammetry, while later season flights should be flown at higher altitudes (>25 m) to ensure image matching, tie point identification, and point cloud densification. The ability to capture early season plant structure is still limited and will require improved SfM functionality or methods that do not rely on SfM photogrammetry (e.g. LiDAR or stereo sensors).

2.3.2.2 Variance Components and Repeatability of UAS Flight Dates

As the crop grew, total variance throughout the growing season increased in a quadratic manner across both platforms and all trials, although the trend was less consistent in low altitude rotary wing (black circles; Figure 4). The repeatability estimates (white

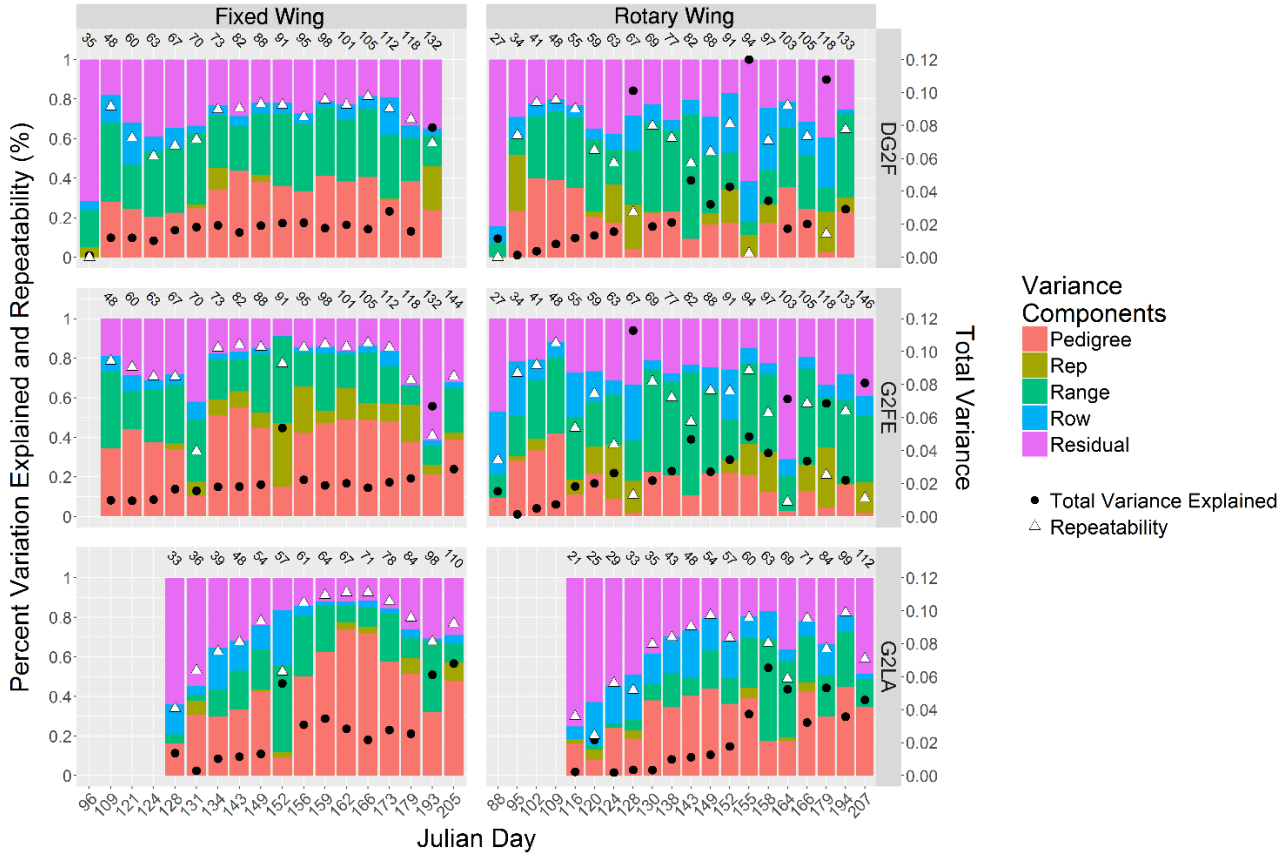

Figure 4. Stack bar graphs of percent variation explain by variables of Eq. 3 for individual UAS surveys of individual UAS platforms (fixed wing and rotary wing) and experimental trials (DG2F: Optimal planted, non-irrigated trial; G2FE: Optimal planted, irrigated trial; G2LA: Delay planted, irrigated trial). Julian day of UAS image collection are indicated by the x-axis and days after sowing (DAS) are indicated by the numbering above the bars. Total variance captured (black circle) per image set, defined by the right y-axis, puts repeatability and genetic variance explained into perspective of other flight dates. Repeatability is indicated by the white triangles.

triangles; Figure 4) were moderate (>60%) to very high (>90%) excluding uninformative image sets (e.g. flight dates with noticeably increased total variance like the rotary wing flight on Julian day 128 of the optimal planted trials, the DSM of which was also visibly distorted). We determined that distorted flights were caused by a failure to identify key tie points in the mature canopies of the early plantings (DG2F, G2FE), leading to poor modeling of the canopy structure; this resulted in increased error variance, reduced consistency between replicates, and reduced genetic variance. Fixed wing surveys captured ~10-40 % increase in greater genetic variation compared to PHT_{TRML} (σ_G^2: ~30%). The rotary wing itself did not improve explaining genetic variance within the early planted trials (Figure 4) and increased genetic variance by ~10% in the late planting (G2LA) compared to PHT_{TRML}. Specifically, estimates from low altitude images became inconsistent during canopy closure accompanied with (DG2F, G2FE), leading to poor modeling of the canopy structure; this resulted in increased error variance, reduced consistency between replicates, and reduced genetic variance. Fixed wing surveys captured ~10-40% increase in greater genetic variation compared to PHT_{TRML} (σ_G^2: ~30%). The rotary wing itself did not improve explaining genetic variance within the early planted trials (Figure 4) and increased genetic variance by ~10% in the late planting (G2LA) compared to PHT_{TRML}. Specifically, estimates from low altitude images became inconsistent during canopy closure accompanied with serendipitous spikes/dips in P95 height estimates and shrinkage of pedigree BLUP variance (e.g. rotary wing in Appendix B5).

Variance component decomposition demonstrated that the majority of UAS surveys were informative. The authors recommend temporal data collection which allows for identification of flights that deviate from normal trend (e.g. spikes in total variance, reduced

genetic variance, increased residual error). It would be difficult to identify if images collected from a single UAS survey should be used in downstream analysis without temporal comparison. Continued research is required to develop tools and methodologies for classifying an individual UAS flight as informative without a comparison group.

2.3.3 Nonlinear Logistic Growth Curves

These and previous UAS surveys of plant height captured appeared as a sigmoidal growth pattern (Figure 3), which is commonly applied to plant growth (Archontoulis and Miguez, 2015; Wardhani and Kusumastuti, 2013). While this data is highly informative, completing UAS surveys over 20 times in a season is resource intensive, impractical and the data can be redundant (assuming quality data is collected on every flight) for some dates. Furthermore, it is not possible to compare data across environments with different planting dates. A model that can both reduce the number of flights needed and predict the optimal flight dates after sowing would be valuable to maximize flight efficiency. Nonlinear models that capture the sigmoidal growth, specifically the logistical function (Eq. 5), provide tools to model temporal crop growth and reduced dimensionality. Nonlinear models were fit on a plot level basis and BLUPs of the logistical parameters were extracted on a pedigree basis within each trial.

The fit of the logistic function had a RSME of 0.06-1.13 m across the trial environments with fixed wing (0.06-0.10 m) having a slightly better fit than the rotary wing (0.10-0.13 m). Similarly, the mean R^2 across plots ranged from 0.98 to 0.99 demonstrating that the logistic function accurately explained the variation in P95 height, regardless of environmental conditions or UAS platform (Appendix A3).

Variance component and repeatability estimates demonstrated that the three parameters of the plot level logistic function captured equivalent or greater genetic variation then PHT_{TRML} (σ_G^2 = ~30 %, R = 60-67% within environments). The inflection point explained the greatest genetic variation in the early planted trials ranging from 43 to 65% of the total variation and met or exceeded the genetic variance captured by any single flight date or PHT_{TRML} (Appendix B6). High genetic variation of the inflection point demonstrated that there was wide genetic variability in PHT at mid-season growth (half way between zero and asymptote). Inflection point is a novel predictive phenotype not captured by single height estimates alone. The variance explained by the asymptote, exceeded the genetic variation of PHT_{TRML}, excluding the G2FE and DG2F rotary wing where tie point identification was poor. The asymptote, indicating terminal growth of the logistic curve, should be equivalent to the PHT_{TRML} measurement. Growth rate explained greater genetic variation than the asymptote in three data sets (fixed wing DG2F, fixed wing G2FE, and rotary wing DG2F) and was never greater than the genetic variation explained by inflection point. The fixed wing comparisons demonstrated that variation in growth rate is reduced if planting is delayed (G2LA trial vs early planting). Reduced variation is explainable by increased growing degree days later within the season leading to more consistent, rapid growth across genetic backgrounds. The rotary wing effectively captured the genetic variation in the inflection point, which occurred during periods of lower canopy density when tie points could be better identified.

Although repeatability of logistic parameters was reduced (did not exceed 60%; Appendix B6) in comparison to the best individual flight date UAS P95 estimates, logistic parameter provided an opportunity to use multi-environment UAS data sets in a combined

Table 1. Combined analysis (Eq. 2) across G2F trials for manual terminal height logistic curve parameters for each UAS platform. Top values are raw variance component estimates, values within parentheses are percent genetic variation explained by each model variable and entry means. UAS estimates used HRI ground modeling and P95 height estimate.

		Fixed wing			Rotary wing		
	PHT_{TRML}	Asymptote	Growth rate	Inflection point	Asymptote	Growth rate	Inflection point
Genotype	$9.9e^{-3}$ (48)	$1.3e^{-2}$ (29)	$1.3e^{-4}$ (23)	1.7 (50)	$7.9e^{-3}$ (37)	$4.1e^{-5}$ (16)	1.3 (16)
Environment	$2.1e^{-3}$ (10)	$2.5e^{-2}$ (55)	$1.8e^{-4}$ (33)	0.5 (16)	$3.4e^{-3}$ (16)	$5.4e^{-5}$ (21)	5.5 (70)
G x E	0 (0)	$8.0e^{-4}$ (2)	$5.4e^{-5}$ (10)	0.1 (4)	$1.8e^{-4}$ (1)	$1.9e^{-6}$ (1)	$5.4e^{-2}$ (1)
Rep [Env]	0 (0)	$1.5e^{-3}$ (3)	$4.5e^{-5}$ (8)	$5.9e^{-2}$ (2)	$4.3e^{-5}$ (0)	$3.2e^{-5}$ (12)	0.2 (2)
Range [Env]	$2.1e^{-3}$ (10)	$1.1e^{-3}$ (2)	$4.7e^{-5}$ (8)	0.2 (7)	$3.2e^{-3}$ (15)	$2.4e^{-5}$ (9)	0.1 (1)
Row [Env]	$3.2e^{-3}$ (2)	$7.9e^{-4}$ (2)	$1.7e^{-5}$ (3)	0.3 (7)	$2.1e^{-3}$ (10)	$2.2e^{-5}$ (8)	0.2 (2)
Residual	$6.1e^{-3}$ (30)	$3.2e^{-3}$ (7)	$8.9e^{-5}$ (16)	0.5 (14)	$4.4e^{-3}$ (21)	$8.3e^{-5}$ (32)	0.6 (7)
Repeatability	0.70	0.85	0.62	0.82	0.73	0.42	0.77

analysis. Specifically, logistical parameters do not confine UAS surveys to similar DAS or calendar dates across environments or years (e.g. P95 at 60 DAS). Combined analysis of PHT_{TRML} measurements (σ_G^2 = 48%, R = 70%, Table 1) was only exceeded by the fixed wing P95 inflection point (σ_G^2 = 50%, R = 82%, Table 1). Although, limited improvement was made in capturing greater genetic variation of the logistic parameter over $PHT_{TRML,}$ a noticeable reduction (23-77%) of residual variation (excluding rotary wing growth rate) was observed (Table 1). Specifically, variance was partitioned to a greater extent within environment, GxE, and spatial variables resulting in a 3%-15% increase in repeatability estimates over PHT_{TRML} (excluding growth rate). The results demonstrated that nonlinear logistic modeling could provide highly repeatable, genetically informative phenotypes which would alleviate the need for capturing of UAS surveys at equivalent days after planting across trial, years, or locations, allowing for more efficient targeting of flight dates, as well as providing novel phenotypes beyond simple height measurements. Incorporation of growing degree days, weather patterns, or other time dependent parameters as the dependent factor (x) of the growth curve could improve comparisons of growth curves across sites, and warrants further investigation.

2.3.4 Correlation to Grain Yield

While the plant height trait is of interest in and of itself, it is of greater interest as a phenotype correlated with and help in predicting the highest yielding genotypes. Pearson's correlations between PHT_{TRML} and grain yield demonstrated 0.28, 0.25, and 0.23 for DG2F (Figure 5), G2FE, and G2LA trials, respectively (Table 2, Appendix B7, Appendix B8, and Appendix B9). These correlations are slightly lower than generally seen in the Texas A&M

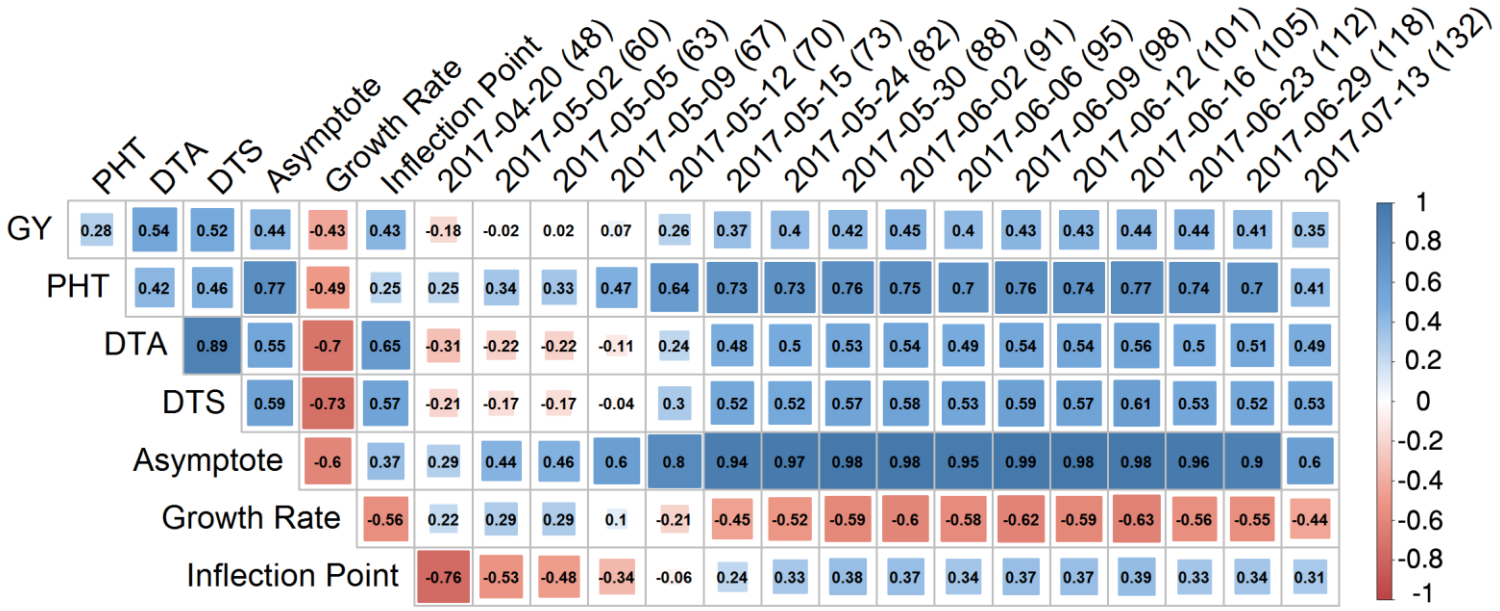

Figure 5. Heat map comparing correlations between grain yield (GY), manual terminal plant height (PHT), flowering time (DTA/DTS), logistic parameters (asymptote, growth rate, inflection point), and UAS P95 estimates by flight date for the DG2F trial surveyed via the fixed wing UAS.

Table 2. Pedigree BLUP correlation between of grain yield and manual terminal plant height (PHT_{TRML}), the flight date with the highest correlation, and the logistic parameters across trials (DG2F: Optimal planted, non-irrigated trial; G2FE: Optimal planted, irrigated trial; G2LA: Delay planted, irrigated trial). Combined columns indicated the correlations based on the pedigree BLUPs of a combined trial analysis.

	Fixed wing				Rotary wing			
	DG2F	G2FE	G2LA	Combined	DG2F	G2FE	G2LA	Combined
PHT_{TRML}	0.28**	0.25***	0.23***	0.27***	0.28**	0.25***	0.23***	0.27***
Best flight date	0.45***	0.42***	0.43****	-	0.41***	0.36****	0.47***	-
Asymptote	0.44***	0.42***	0.42***	0.39***	0.44***	0.38***	0.45***	0.41***
Growth rate	-0.46***	-0.42***	-0.34***	-0.42***	-0.30***	-0.13***	-0.13**	-0.29***
Inflection point	0.46***	0.42***	0.18	0.36***	0.42***	0.36***	0.15*	0.36***

* Significant at $\alpha < 0.05$

** Significant at $\alpha < 0.01$

*** Significant at $\alpha < 0.001$

breeding program and substantially lower than that found in Farfan, et al. (2013); likely due to the G2F experiment including hybrids of diverse origins which contained a variety of unadapted factors that affect the yield and plant height relationship in different ways (e.g. photoperiod sensitivity, temperature stress, drought stress, etc.). The UAS P95 height estimates showed higher correlations to grain yield than PHT_{TRML} beginning ~70 DAS for DG2F and G2FE, while flights after ~50 DAS show higher correlation to yield in the G2LA trial. Furthermore, fixed wing UAS P95 heights maximum yield correlations of 45, 42, and 42 percent; while rotary wing reach 41, 36, and 46 percent correlation to yield for DG2F, G2FE, and G2LA, respectively (Table 2). The ~20% increase in correlation to yield from UAS P95 estimates over PHT_{TRML} measurements demonstrate that UAS P95 height estimates can serve as an improved method for collecting phenotypes to improve genetic gain.

Correlation between temporal measures of UAS P95 height and yield increased with time and were least informative to grain yield prior to the reproductive growth and grain fill stages. If using only plant height to predict yield, late season flights are more informative than flight prior to the vegetative to growth transition. However, both plant height and grain yield are sculpted by daily interactions between the genetics of the plants and the environment up to that point. This lack of correlation between early season UAS P95 height and yield suggests the genetic variation in early season height is under independent genetic control. We hypothesize that vigorous early season growth could be pyramided into the terminally taller, higher yielding plants to develop varieties improved across all growth stages; UAS P95 height estimates would be critical for practically testing this hypothesis.

While individual flight dates were highly correlated to grain yield, the logistic parameters correlation to grain yield equaled the highest correlated single flight date P95 height measurement. The asymptote parameter was 38 to 45 percent correlated to grain yield across trials and platforms (Table 2). The asymptote parameter describes the maximum plant height of the logistic curve and was 69% to 76% correlated to PHT_{TRML} (Figure 5, Appendix B7, Appendix B8, and Appendix B9). The inflection point was also 36% to 46% correlated to grain yield in DG2F and G2FE, while becoming less informative (15% to 18%) in the later G2LA trial (Table 2). We speculate that the high correlation of inflection point and asymptote to grain yield may be equivalent to the previously reported predictive power of V6 and V10/12 height to grain yield (Machado, et al., 2002; Yin, et al., 2011), although a leaf counting study would be necessary to validate this hypothesis. Growth rate depicted a negative trend to grain yield while showing a significant reduction in correlation from fixed wing (-30 to -46 %) to rotary wing (-13 to - 30%). The negative correlations between growth rate with both grain yield and plant height relates to the negative correlation between flowering time (37 -73%) and growth rate (Appendix B7, Appendix B8, and Appendix B9). Early maturity results in less vegetative growth and shorter plants. In addition, early hybrids are more likely to originate from the far northern U.S. and may be maladapted to Texas conditions.

2.3.5 Predicting Grain Yield from UAS Height Phenotypes

While simple correlations provided relationships between grain yield and a single P95 estimate/logistic parameter, it is possible that multiple height factors could be combined to make more robust predictions of yield. Forward and reverse stepwise regression was performed to identify the most predictive UAS height parameters for grain yield (tonnes per

hectare, t ha^{-1}), the best of these were then fit as continuous effects in a linear model. Models were developed for each UAS platform separately with three sets of possible predictors: (i) the logistic parameters, (ii) pedigree P95 height BLUPs by flight date, and (iii) the combination of logistic parameter and pedigree P95 height BLUPs by flight date.

Initially PHT_{TRML} was used as the predictor of grain yield which resulted in a R^2 of 0.08, 0.06, and 0.07 with a RMSE of 1.02, 1.05, and 0.68 t ha^{-1} for DG2F, G2FE, and G2LA, respectively, and R^2=0.16, RMSE=0.50 t ha^{-1} from a combined trial analysis. Excluding logistic parameters, the fixed wing flights identified the two flight dates most informative in yield prediction at ~ 40 to 50 DAS and ~110 to 120 DAS significantly increasing R^2 (0.28-0.38) and reducing RMSE by ~0.06 t ha^{-1} (Table 3, Appendix A4).

Similar R^2 and RSME were obtained with rotary wing flights with the addition of a third predictor around 70 DAS. Using only the logistic parameters, predictive power was slightly reduced (fixed wing R^2: 0.26 – 0.34; rotary wing R^2: 0.25 – 0.33) compared to the best sets of individual flight dates (Table 3), but were significantly improved compared to PHT_{TRML}. Combining individual flight data and logistic parameters showed no improvement in predictive power and was inconsistent in the inclusion of only flight dates or a combination of flight dates and logistic parameters in the selected models (Appendix A4). The individual flight dates identified through stepwise regression co-localize with the inflection point period (40-53 DAS) and terminal plant height (i.e. asymptote) which indicates why the logistic parameter model achieved equivalent predictive power to the specific flight date model.

The comparison of relative rankings of hybrids from the models using logistic parameters versus PHT_{TRML} measurements demonstrated improved selection accuracy of

Table 3. Coefficient of determination (R^2) for the best prediction models of yield defined by stepwise regression (Appendix A4) by UAS platform (fixed wing and rotary wing) and G2F trial (DG2F: Optimal planted, non-irrigated trial; G2FE: Optimal planted, irrigated trial; G2LA: Delay planted, irrigated trial). Values in parentheses are the root mean squared error of grain yield (t ha^{-1}). Combined columns indicated the combined trial analysis.

Grain yield predictors	Fixed wing				Rotary wing			
	DG2F	G2FE	G2LA	Combined	DG2F	G2FE	G2LA	Combined
Logistic parameters†	0.34 (0.92)	0.26 (0.95)	0.27 (0.62)	0.32 (0.49)	0.33 (0.94)	0.32 (0.99)	0.25 (0.62)	0.32 (0.49)
Flight dates‡	0.38 (0.92)	0.35 (0.97)	0.28 (0.60)	NA	0.39 (0.90)	0.33 (0.99)	0.26 (0.61)	NA
Logistic parameters and flight dates§	0.37 (0.92)	0.35 (0.97)	0.28 (0.60)	NA	0.38 (0.92)	0.33 (0.98)	0.26 (0.61)	NA

† Prediction model defined using logistic parameters in the stepwise regression.

‡ Prediction model defined using UAS estimates by flight date in the stepwise regression. The same flight date was at different growth stages for early and late (G2LA) plantings, so they could not be combined (NA).

§ Prediction model defined using logistic parameters and UAS estimates by flight date in the stepwise regression.

UAS derived logistic curves over PHT_{TRML} measurements (Appendix A5). Prediction of grain yield using logistic parameters improved ranking error by 7-10 ranks over PHT_{TRML} prediction (MAE= 59-78 ranks; Appendix A5). Although improvement in relative ranking is ideal, plant breeders generally select a subset (e.g. top 10% yielding hybrids) of their evaluated material to advance in evaluation trials. UAS logistic based prediction improved the selection accuracy of the top 10% yielding hybrids by ~50% - 150% over PHT_{TRML} predictions (21%), and the combined analysis demonstrated a 7% and 12% increase in selection accuracy for the fixed wing and rotary wing, respectively (Appendix A5).

For a plant breeding program, selecting material to advance by UAS a month or more before maturity can speed the breeding cycle, substantially decrease the cost and time compared to combine harvesting, and allow more environments to be screened. However, it is acknowledged that the prediction of grain yield solely upon height measurements is not an acceptable model of yield prediction in these trials; nevertheless, significant improvements in predictive power were obtained by using UAS technologies temporally. Additional UAS estimated phenotypes (vegetation indices, canopy cover, plant population, etc.) need to be developed and included with height for better predictions of yield if plant breeders will ever be able to select based on remote sensing data.

For fundamental research into plant physiology, genetics, and development these UAS findings open up interesting avenues to identify differences in growth trajectories, impractical to measure previously. Most importantly, such studies can be conducted on mature plants, non-destructively, in a field setting, which is important if discoveries are ever to be used in practical crop or agronomic improvement.

2.4 Conclusion

This study is one of the first applications of UAS phenotyping of agriculture research at representative scale (>1,500 plots) of a breeding/agriculture research program. The comparisons of different UAS platforms and flight altitudes have provided additional insights towards reliable application of UAS imagery within an agricultural field trial setting, specifically within crops with dense canopy structure yet sparse apex canopy features (e.g. tassels). To our knowledge, this is one of the first empirical studies to move beyond UAS phenotype validation towards phenotypic predictive modeling across a large set of plant material (280 hybrids), while validating a previous finding (Pugh, et al., 2018) in a different germplasm pool and environment. Four of the most important findings were: (i) the dense canopy structure at later growth stages of maize restricts execution of SfM photogrammetry, returning inconsistent data quality, specifically at low flight altitudes. (ii) Increased genetic variation (10-40%) was captured by UAS P95 compared to conventional manual terminal plant height, accompanied with reduced residual error, resulting in increased measurement repeatability. (iii) Logistic functions accurately model UAS maize height estimates, which can be used in place of independent flight dates to develop robust prediction models and allow for execution of combined environment analysis with relative ease. (iv) Predictive modeling of grain yield via UAS height estimates or logistic function parameters demonstrated substantial improvements in the proportion of grain yield variation explained and overall selection accuracy compared to traditional PHT_{TRML} in model selection accuracy.

CHAPTER III

UNMANNED AERIAL SYSTEMS REVEAL DYNAMIC EXPRESSION OF QUANTITATIVE TRAIT LOCI ASSOCIATED WITH PLANT HEIGHT IN MAIZE (*Zea mays* L.)

3.1 Introduction

Phenotypic characterization of agricultural plant populations have been lagging in scale, density, and accuracy when compared with genomic data (Pauli, et al., 2016). Due to resource demands (labor, time, etc.) involved in conventional phenotyping, most manually measured traits are acquired at one time point in the growing season, leading to a limited scope of interest for the genomic information associated with the underlying the traits of interest (Furbank and Tester, 2011). Recently, advances in technologies including computer processing, robotics, imaging software, unmanned vehicles and sensors have facilitated the development of high-throughput phenotyping platforms (HTPP) to improve phenotypic bottlenecks (Araus and Cairns, 2014; Araus, et al., 2018).

Implementation of HTTP systems now provides the ability to collect temporal phenotypic measurements on representative breeding populations within a field based setting (Araus and Cairns, 2014; Sankaran, et al., 2015; Shi, et al., 2016). Currently, unmanned aerial systems (UAS) are being used to collect RGB images and reconstructed three dimensional representations of field trials using structure from motion methodology for height estimates in field crops (Anderson, et al., 2019; Bendig, et al., 2014; Chang, et al., 2017; Chu, et al., 2018; De Souza, et al., 2017; Holman, et al., 2016; Malambo, et al., 2018; Pugh, et al., 2018; Shi, et al., 2016; Watanabe, et al., 2017). UAS height estimates of maize

have been extensively validated by both high correlations to traditional manual measurements and by having equivalent or greater phenotypic variation partitioned to genetic factors (Anderson, et al., 2019; Chu, et al., 2018; Pugh, et al., 2018). To our knowledge the majority of reported field based phenotyping of maize with HTTP platforms has been with respect to hybrid trials (Anderson, et al., 2019; Chu, et al., 2018; Geipel, et al., 2014; Li, et al., 2016; Malambo, et al., 2018; Pugh, et al., 2018; Shi, et al., 2016; Varela, et al., 2017) and limited reports have been published on the evaluation of inbred trials (Han, et al., 2019; Han, et al., 2018; Wang, et al., 2019), specifically genetic mapping populations.

Maize height is both an important and a highly heritable agronomic trait (Anderson, et al., 2018; Li, et al., 2016; Peiffer, et al., 2014; Wallace, et al., 2016) that is commonly collected due to its ease in measurement, agronomic importance, and correlation to hybrid grain yield in some situations. Manually measured plant height is commonly collected after reproductive maturity at the distance from the ground to the tip of the tassel. The genetic architecture of plant height in maize has been explained as an infinitesimal model (i.e. very large numbers of small additive effect loci) with some large effect loci likely fixed during domestication and early selection (Peiffer, et al., 2014). Genetic variation in terminal plant height have been shown to have functional control through other hormones; mutations within the (i) gibberellin biosynthesis pathways (Lawit, et al., 2010) and crosstalk with other phytohormomes including: (ii) auxin (Multani, et al., 2003) and (iii) brassinosteriods (Hartwig, et al., 2011; Makarevitch, et al., 2012; Wang, et al., 2017; Winkler and Helentjaris, 1995). Traditional QTL studies using phenotypic data at a single terminal time point can only represent the accumulated QTL effects while ignoringthe dynamic nature of many

agronomically important traits which change and should be mapped as a function of time (Wu and Lin, 2006).

Patterns of temporal QTL expression using field-based HTTP systems have been demonstrated for soybean canopy cover (Xavier, et al., 2017), cotton stress-response traits (Pauli, et al., 2016), spring barley biomass accumulation (Neumann, et al., 2017), rice yield components (Tanger, et al., 2017), and tricticale plant height (Würschum, et al., 2014). Temporal patterns of QTL have been evaluated in maize within greenhouse setting using automated phenotyping platforms (Muraya, et al., 2017; Zhang, et al., 2017), to our knowledge Wang, et al. (2019) is the only reported field based temporal QTL study in maize. The agronomic importance, high heritability, depth of QTL knowledge and validated UAS phenotyping procedures make plant height an excellent phenotype for evaluating temporal patterns of QTL expression in maize as a proof of concept. Using UAS we evaluated three recombinant inbred line (RIL) linkage mapping populations under field conditions and captured the dynamic growth patterns of plant height in maize inbreds. The objectives of this study were to (i) assess the ability to of UAS to estimate heights within inbred maize populations as seen in hybrid trials, (ii) compare growth patterns across genetic populations via sigmoidal modeling, (iii) evaluate temporal patterns of QTL expression through the growing season for maize height, and (iv) compare with previously reported QTL to determine if they undergo changes in temporal expression.

3.2 Materials and Methods

3.2.1 Germplasm Material and Experimental Design

Three bi-parental mapping populations were developed from breeding lines by Dr. Yuanyuan Chen (Chen, 2016) specifically to validate three height quantitative trait

nucleotides (QTN) for which they segregated within the Texas environment. The three QTN were discovered in an earlier genome wide association study (GWAS) (Farfan, et al., 2015) for height and grain yield. The recombinant inbred line (RIL) progeny were derived from the crosses of Tx740/NC356 (tropical/tropical; 110 RILs), Ki3/NC356 (tropical/tropical; 239 RILs) and LH82/LAMA-YC (temperate/tropical; 178 RILs). Tx740 (LAMA2002-12-1-B-B-B) (Mayfield, et al., 2012) is a parent in the "LAMA" inbred line which has the pedigree ((LAMA2002-12-1-B-B-B-B/LAMA2002-1-5-B-B-B-B)-3-2-B-1-B3-B). In 2018, the mapping populations were planted in a randomized complete block design (RCBD) with two replications across two environments (irrigated and non-irrigated) with dimensions of 0.76 m row spacing, and 3.81 m plot lengths.

3.2.2 Unmanned Aerial System Image Collection

Two platforms were used, a rotary wing and a fixed wing UAV. For the rotary wing, a DJI Phantom 3 Professional with a 12 megapixel DJI FC300X camera was flown at an altitude of 25 m with to 80% forward and side image overlap. Fixed wing images were collected with a Tuffwing UAV Mapper (http://www.tuffwing.com) equipped with a 24 megapixel Sony a6000 RGB camera. Fixed wing surveys were conducted at a 120 m altitude with 80% image overlap. A total of 19 DJI Phantom 3 Professional flights were conducted throughout the growing season, while 11 Tuffwing UAV Mapper flights (starting 05/17/2018) were conducted due to mechanical setbacks of the Tuffwing. After QC/QA a total of 16 flights were used for height estimates based on mosaicking quality and limited data blunders.

All of the Tuffwing flights were processed in Agisoft PhotoScan (AgiSoft PhotoScan Professional, 2016), while the majority of the DJI Phantom flights were processed in

Pix4Dmapper, based on collaborators comfort and preference with the associated software. In general, these software packages are equivalent and used to identify common features (tie points) across images followed by triangulation and distortion adjustment optimization to generate densified 3D point clouds, DSM, and orthomosaic images. Height estimates were extracted from the three dimensional point clouds following the procedures of (Anderson, et al., 2019). In short, the ground points were identified from the point cloud using the hierarchical robust interpolation algorithm within FUSION/LDV. Identified ground points were used to interpolate the digital elevation model, followed by subtracting the DEM from the original point cloud to produce the canopy surface model. The plot level polygon shapefiles were created using the R/UAStools::plotshpcreate (Anderson, et al., 2019) function in R and the 95th percentile height estimates were extracted for each experimental plot.

3.2.3 Statistical Inference

3.2.3.1 Variance Component Estimates and Heritability

From the extracted point cloud derived canopy height metrics (P95), we fit mixed linear models utilizing residual maximum likelihood (REML) in JMP version 14.0.0 (JMP®, 2018) to define best linear unbiased predictors (BLUPs) of the inbreds by their entry number. Models were fit on a per flight date basis. The individual mapping populations were evaluated as a randomized complete block design (RCBD, Eq. 6) including spatial regression (range and row [furrow irrigation runs down rows], but this is also called row and column, respectively, where furrow irrigation is not used).

$$Y = \mu + \sigma_G^2 + \sigma_r^2 + \sigma_i^2 + \sigma_j^2 + \sigma_\varepsilon^2 \qquad \text{Eq. [6]}$$

with terms entry (σ_G^2), replicate (σ_r^2) range (σ_i^2), row (σ_j^2) and residual error (σ_ε^2).

Broad sense heritability (H^2) estimates were calculated on an entry means basis (Eq.7).

$$H^2 = \frac{\sigma_G^2}{\sigma_G^2 + \sigma_\varepsilon^2/\mathrm{r}}$$

Eq. [7]

Within each environment, H^2 estimates were calculated for each population separately while including replicates (r) for each of the UAS flight dates.

3.2.3.2 Nonlinear Function

The three parameter Weibull sigmoid growth model (Eq. 8) was used to summarize the

$$f(x) = L * \left(1 - e^{\left(-\left(\frac{x}{x_0}\right)^k\right)}\right)$$

Eq. [8]

height as a function of DAS (x) with the asymptote (L), inflection point (x_0), and the growth rate (k) of the fitted curve. The asymptote (L; m) is maximum value of the curve which represents maximum/terminal plant height (PHT_{TRML}). The inflection point **(**x_0; DAS)

indicates the DAS where the slope of the logarithmic phase is at its absolute maximum. The growth rate (k; DAS^{-1}) estimates the steepness of the curve. Sigmoidal curves were fit using the Fit Curve tool in JMP 14 (Analyze→Specialized Modeling→Fit Curve) and parameters were estimated on an entry basis utilizing the extracted BLUPs or the individual environment REML models described above. Heights of zero were assigned to the day of planting and days pre-planting to fit the curve. Significance of the logistic parameters were evaluated using the chi squared (X^2) test ($\alpha = 0.05$, $df = 1$) to identify logistical curves with poor fits to UAS height estimates, these were subsequently removed from future analysis. Using the associated Weibull growth curve parameter, height estimates were imputed on a one day interval (1 to 85 DAS) for each inbred entry in their associated environment.

3.2.4 Genotyping and Linkage Map Construction

The genotyping was described in Chen 2016, and is paraphrased here. Genotype samples were collected from $F_{3:4}$ seedlings grown under greenhouse conditions, where eight samples were bulked per genotype. The CTAB method (Chen and Ronald, 1999) was used to extract DNA and samples were sent to AgReliant Genetics LLC, where they were genotyped by Infinium® assays for 17,444 single nucleotide polymorphisms (SNPs). The linkage groups and physical locations were provided with the SNP chip of which 716 markers locations were unknown or withheld due to intellectual property rights, resulting in 17,019 SNPs with known reference locations (B73 RefGEN_v3).

Individuals with >10% missing values and SNPs with >10% missing values were dropped from the data set resulting in 5316, 5628, and 6231 polymorphic SNPs for the Ki3/NC356, Tx740/NC356, and LH82/LAMA populations, respectively. Crosspoints were predicted using the crosspoint subcommand of SNPbinner (Gonda, et al., 2018) to clean data

set of double recombinants. The emission probability was set to 0.9 (-p 0.9), the continuous genotype region was set to 0.1% (-r 0.001) of the chromosome size, and the transition probability was calculated using a crosscount of 7,500,000 (-c 7,500,000). The visualize subcommand was used to evaluate the efficiency of the calculated break points to the original SNP calls and identify satisfactory crosspoint parameters. The crosspoint output identified break point locations for each RIL and the prediction of genotypic homogeneity of each region between breakpoint and the SNP calls were adjusted accordingly. Marker datasets filtered by SNPbinner were constructed into linkage maps using the MAP function of QTL IciMapping version 4.1.0.0 (http://www.isbreeding.net/) software. Linkage groups were defined by "By Anchor Only" setting and the marker orders were defined by their physical locations using the "By Input" ordering algorithm. Recombination frequencies between markers were calculated based on F_3 marker frequencies by denoting the "POP.ID" to eight.

The final genetic maps consisted of 1530, 2571, and 2324 SNPs after removal of redundant markers. The genetic map distances were calculated in QTL IcIMappering using the Kosambi mapping function, and the total map lengths were estimated to be 1315, 1207, and 1474 cM for the Tx740xNC356, Ki3xNC356, and LH82xLAMA populations, respectively.

3.2.5 Linkage Mapping

The entries phenotyped in 2018 were advanced several generations following initial DNA extraction and were evaluated in the field at F_6 generation or greater. For this reason, heterozygous calls (1) were set to missing (-1) and QTL analysis was performed assuming RIL genotype frequencies ("POP.ID" = 4). Analysis by other methods (e.g. treating as F_3) were also tested to ensure conclusions were similar, but detection power was much lower,

likely due to the software trying to fit dominance effects, which are expected to be very rare in an F_6 generation . Inclusive Composite Interval Mapping (Li, et al., 2007) of Additive (ICIM-ADD) QTL was conducted in the QTL IciMapping v4.1 using the BIP (QTL mapping for bi-parental populations) function. The step parameters was set to 1.0 cM and the probability of inclusion in the stepwise regression (PIN) was set to 0.001. The focus of this study was on understanding the temporal shifts in the marker trait associations of plant height, rather than identifying regions of high confidence that could be used in later marker assisted selection. For these reasons, we defined QTL of interest liberally as those with LOD > 2.0 and percent variation explained $\geq 3\%$ (Li, et al., 2008), however LOD and other metrics are provided to extract more conservative thresholds. Using the imputed heights from 1 to 85 DAS, ICIM-ADD was performed on each DAS, for each population in each environment separately to access the temporal shifts in allelic effects and marker–trait associations.

Candidate genes list was obtained from Wallace, et al. (2016). In short, candidate genes were identified from (i) literature, (ii) mining the MaizeGDB database for known height mutants, and (iii) searching the maize genome annotation on Phytozome genes annotated with “auxin”, “brassinosteroid” and/or “gibberellin”. Distance for the center of the QTL confidence interval to nearest candidate gene with the same chromosome were identified.

3.3 Results and Discussion

3.3.1 UAS Surveys and Image Processing Quality

A total of 18 and 11 flights were conducted over the bi-parental mapping populations for the DJI Phantom 3 Pro and Tuffwing UAV Mapper, respectively (Appendix A6). Early season DJI flights prior to 35 DAS resulted in limited to no plant structure being

reconstructed within the 3D point clouds, indicating that higher resolution imaging is necessary to reconstruct early seasons plant structure. Due to mechanical issues, Tuffwing image surveys did not begin until 64 DAS (05-17-2018). Qualitative, visual assessment of point clouds and image processing reports demonstrated reduced tie point matching leading to "black holes" in point clouds in later season flights (>70 DAS), with the vast majority occurring in the low altitude DJI flights. We hypothesize that the increased homogenous canopy appearance, coupled with reduced frame of reference of the low-altitude images led to the failure of the SfM algorithms to identify tie points for three dimensional point cloud construction in these cases. Our image processing results of inbred populations surveys are similar to image processing results of hybrid maize trial UAS surveys (Anderson, et al., 2019), demonstrating that the level of inbreeding did not result in differential image processing quality. Following qualitative assessment for blunders and black holes, six DJI (35-72 DAS) and ten Tuffwing (64-133 DAS) flights (16 total) were identified as high quality point clouds for extraction of height estimates.

3.3.2 Statistics Inference

It is well documented that the quality of information contained within UAS image derived datasets fluctuates by flight date (Anderson, et al., 2019). For these reasons we have used several statistical and qualitative approaches to further filter our temporal dataset. First, we fit our RCBD design using REML approaches and extracted P95 entry based BLUPS by flight date, grouped by population and irrigation treatment. Using the entry BLUPs, Tukey HSD mean comparisons were made across flight dates for each population in each environment to identify flights that did not follow the standard sigmoidal growth pattern of maize (Anderson, et al., 2019; Archontoulis and Miguez, 2015). Flights on 64, 68, and 71

DAS produced a canopy of plants (all entries) far shorter than expected and were removed, which significantly lowered means during the exponential phase of growth. Days 72 and 96 were removed due to significantly larger means in comparison to other dates past the curve's upper vertex within the period of terminal growth (>65 DAS), where height should be consistent. In theory, phenotypic variance of plant height should increase throughout the growing season and become consistent across terminal growth dates. Following this theory, we conducted an unequal variances test across flight dates and identified days 71, 83, 86, 96, 124, and 133 as dates which deviate from theory in two or more populations by environment grouping. Ignoring those flights with unequal variance resulted in eight high quality flight dates (35, 43, 57, 62, 65, 69, 100, and 117 DAS) used for the remainder of this study (Figure 6).

The mean height of the Tx740xNC356 non-irrigated RILS increased from 0.08 m (35 DAS) to 1.12 m (100 DAS) with an average range of 0.35 m and the irrigated trial increased from 0.07 m (35 DAS) to 1.39 m (100 DAS) with an average range of 0.34 m (Table 4). Tx740 and NC356 reached a max estimated height of 1.17 m in the non-irrigated trial and a max estimated height of 1.06 m and 1.11 m in the irrigated trial, respectively. KixNC356 non-irrigated RILS increases from 0.07 (35 DAS) to 1.07 m (100 DAS) with an average range of 0.41 m and the irrigated trial increased from 0.00 (35 DAS) to 1.11 m (100 DAS) with an average range of 0.44 m. Ki3 and NC356 reached a max estimated height of 1.05 and 1.17m in the non-irrigated trial and a max estimated height of 1.02 and 1.11 m in the irrigated trial, respectively. LH82xLAMA non-irrigated RILS increases from 0.08 (35 DAS) to 1.10 m (100 DAS) with an average range of 0.40 m and the irrigated trial increased

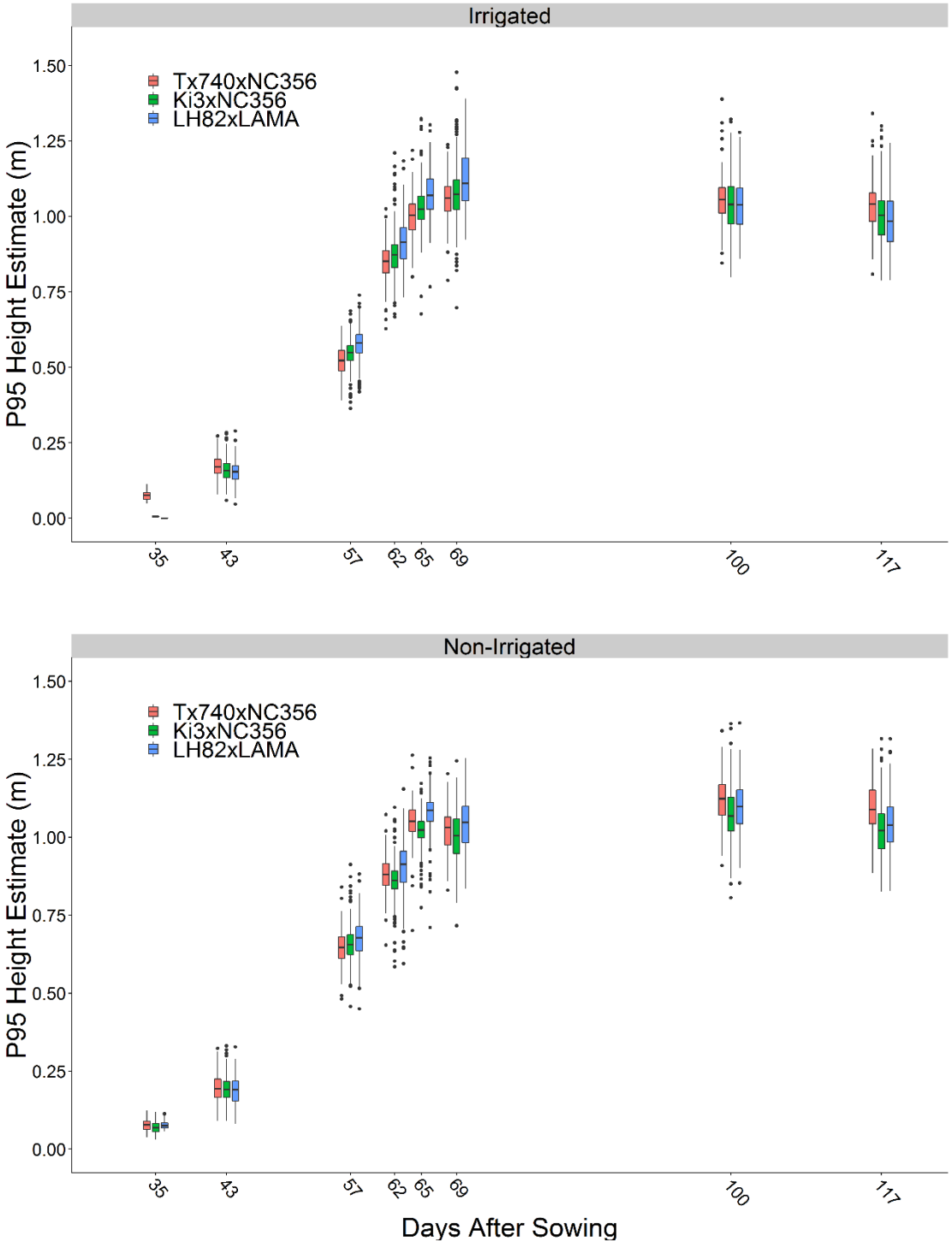

Figure 6. Boxplot representations of mapping populations (Tx740xNC356, Ki3xNC356, and LH82xLAMA) across the eight identified flight dates with high quality point clouds for the irrigated (top) and non-irrigate (bottom) trials.

Table 4. Summary statistics of the entries for each population (Tx740xNC356, Ki3xNC356, and LH82xLAMA) across the eight identified flight dates with high quality point clouds for the irrigated and non-irrigated trials.

		Non-Irrigated Trial							Irrigated Trial						
Population	DAS†	N Genotypes	Mean	Std. Dev.	Min	Max	Female Mean	Male Mean	N	Mean	Std. Dev.	Min	Max	Female Mean	Male Mean
Tx740xNC356	35	101	0.08	0.02	0.04	0.12	0.08	0.11	87	0.07	0.01	0.06	0.11	0.05	0.11
Tx740xNC356	43	101	0.19	0.05	0.09	0.32	0.17	0.24	100	0.17	0.04	0.08	0.27	0.11	0.21
Tx740xNC356	57	101	0.65	0.06	0.48	0.84	0.63	0.69	100	0.52	0.05	0.39	0.64	0.49	0.59
Tx740xNC356	62	101	0.88	0.06	0.65	1.07	0.88	0.90	100	0.85	0.07	0.63	1.03	0.82	0.88
Tx740xNC356	65	101	1.05	0.07	0.70	1.26	1.07	1.08	100	1.00	0.07	0.80	1.22	0.96	1.02
Tx740xNC356	69	101	1.03	0.07	0.83	1.20	1.05	0.95	100	1.06	0.07	0.79	1.24	1.01	1.10
Tx740xNC356	100	101	1.12	0.08	0.91	1.34	1.17	1.17	100	1.07	0.09	0.88	1.39	1.06	1.11
Tx740xNC356	117	101	1.10	0.07	0.91	1.28	1.13	1.08	100	1.04	0.08	0.86	1.34	1.05	1.06
Ki3xNC356	35	237	0.07	0.02	0.04	0.12	0.05	0.11	196	0.01	0.00	0.01	0.01	0.01	0.01
Ki3xNC356	43	237	0.19	0.04	0.09	0.33	0.17	0.24	238	0.16	0.04	0.06	0.28	0.17	0.17
Ki3xNC356	57	237	0.66	0.06	0.46	0.91	0.64	0.68	238	0.55	0.05	0.36	0.69	0.54	0.51
Ki3xNC356	62	237	0.86	0.07	0.58	1.10	0.87	0.88	238	0.88	0.08	0.67	1.21	0.82	0.88
Ki3xNC356	65	237	1.02	0.06	0.77	1.17	1.03	1.05	238	1.03	0.08	0.68	1.32	0.97	1.00
Ki3xNC356	69	237	1.00	0.09	0.72	1.24	1.00	1.04	238	1.08	0.10	0.70	1.48	1.02	1.10
Ki3xNC356	100	237	1.07	0.08	0.81	1.36	1.05	1.17	238	1.04	0.10	0.80	1.32	1.02	1.11
Ki3xNC356	117	237	1.02	0.09	0.82	1.32	1.02	1.07	238	1.01	0.09	0.79	1.30	0.98	1.06

Table 4. Continued.

		Non-Irrigated Trial							Irrigated Trial						
Population	**DAS†**	**N**	**Mean**	**Std. Dev.**	**Min**	**Max**	**Female Mean**	**Male Mean**	**N**	**Mean**	**Std. Dev.**	**Min**	**Max**	**Female Mean**	**Male Mean**
LH82xLAMA	35	174	0.08	0.01	0.06	0.11	0.06	0.06	101	0.00	0.00	0.00	0.00	0.00	0.00
LH82xLAMA	43	174	0.19	0.04	0.08	0.33	0.24	0.09	175	0.15	0.04	0.05	0.29	0.18	0.07
LH82xLAMA	57	174	0.68	0.06	0.45	0.88	0.72	0.58	175	0.58	0.05	0.42	0.74	0.61	0.45
LH82xLAMA	62	174	0.90	0.09	0.59	1.15	0.91	0.78	175	0.92	0.08	0.73	1.18	0.95	0.81
LH82xLAMA	65	174	1.08	0.07	0.71	1.25	1.05	1.07	175	1.08	0.08	0.77	1.30	1.05	1.00
LH82xLAMA	69	174	1.04	0.07	0.87	1.25	0.84	0.89	175	1.13	0.10	0.92	1.39	1.02	1.08
LH82xLAMA	100	174	1.10	0.08	0.85	1.37	0.92	1.16	175	1.04	0.09	0.86	1.28	0.89	1.09
LH82xLAMA	117	174	1.04	0.08	0.83	1.32	0.84	1.14	175	0.99	0.10	0.79	1.24	0.81	1.06

† DAS: Days after sowing.

from 0.00 (35 DAS) to 1.04 m (100 DAS) with an average range of 0.36 m. LH82 and LAMA reached a max estimated height of 0.92 and 1.16 m in the non-irrigated trial and a max estimated height of 0.89 and 1.09 m in the irrigated trial, respectively.

3.3.2.1 Variance Components and Heritability of UAS Height Estimates

Variance component decomposition demonstrated total phenotypic variance increased throughout the growing season for all inbred populations (Figure 7, black circles)

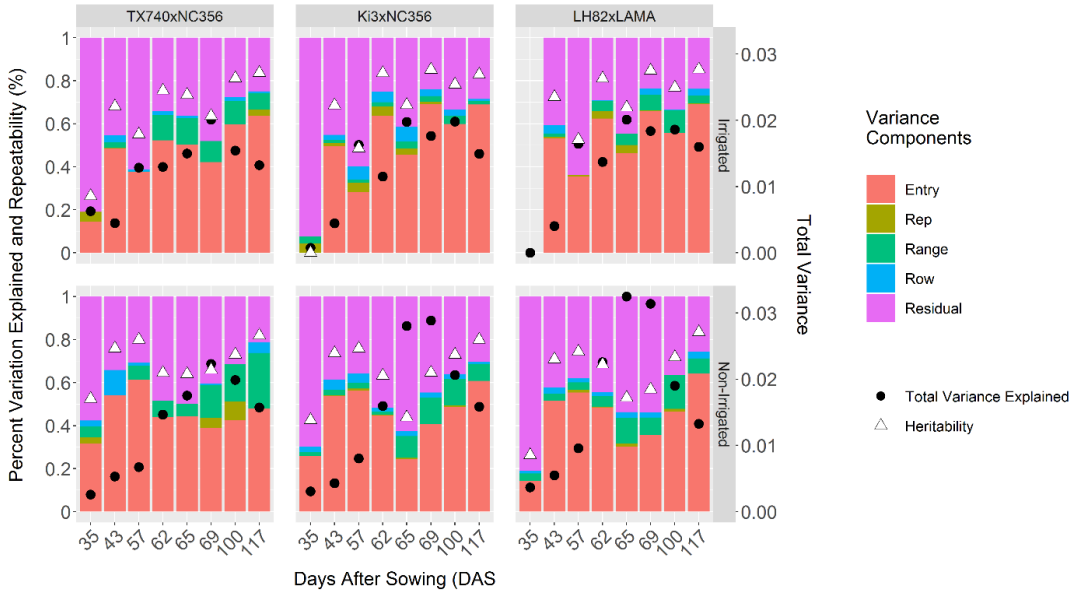

Figure 7. Stack bar graphs of percent variation explain by variables of Eq. 1 for individual UAS surveys of experimental mapping populations (Tx740xNC356, Ki3xNC356, and LH82xLAMA) for each irrigation regimen (irrigated and non-irrigated). Days after planting (DAS) of UAS image collection are indicated by the x-axis. Total variance captured (black circle) per image set, defined by the right y-axis, puts repeatability and genetic variance explained into perspective of other flight dates. Heritability is indicated by the white triangles.

similar to hybrid trials. Genetic variance fluctuated from flight to flight throughout the growing season, based on quality of the flights, but had an increasing general trend. The proportion of variation attributed to genetics (σ^2_G) was 51±7, 55±11, and 55±9% within the irrigated trial and 49±6, 48±10, and 49±9% within the non-irrigated trial for Tx740xNC356, Ki3xNC356, and LH82xLAMA, respectively. Manual terminal height measurements within the irrigated trial partitioned 65, 59, and 76% and the non-irrigated trial attributed 51, 50, and 54 % of the phenotypic variation to genetics for Tx740xNC356, Ki3xNC356, and LH82xLAMA, respectively. Broad sense heritability (H^2) estimates peaked at 84, 85, and 85% with mean H^2 of 72±7, 74±13, and 74±12% for the irrigated trials. Within the non-irrigated trial, H^2 peaked at 82, 80, and 83 with mean H^2 of 73±6, 68±11, and 70±8% for Tx740xNC356, Ki3xNC356, and LH82xLAMA, espectively. Broad sense heritability of the terminal manually measured plant height (PHT_{TRML}) was estimated at 81, 76, and 76% in the irrigated trial and 80, 70, and 73% in the non-irrigated trial for Tx740xNC356, Ki3xNC356, and LH82xLAMA, respectively.

3.3.2.2 Sigmoidal Modeling of UAS Height Estimates

Sigmoidal growth functions are an accurate way of modeling the dynamic growth of an annual crop, such as maize (Archontoulis and Miguez, 2015). The Weibull function showed an improved fit to the data over the logistic and Gompertz functions based on information criteria statistics (AIC, BIC, etc.) and was used in this analysis. The Weibull function effectively modeled the temporal growth with mean R^2>0.99 and mean RMSE ranging from 2.4 to 3.7 cm across all populations and environment (Figure 8). Significant differences in asymptote were found between Tx740xNC356 (1.10 m) and LH82xLAMA (1.08 m) with a 2 cm difference in means under irrigation; LH82 is the earliest and shortest

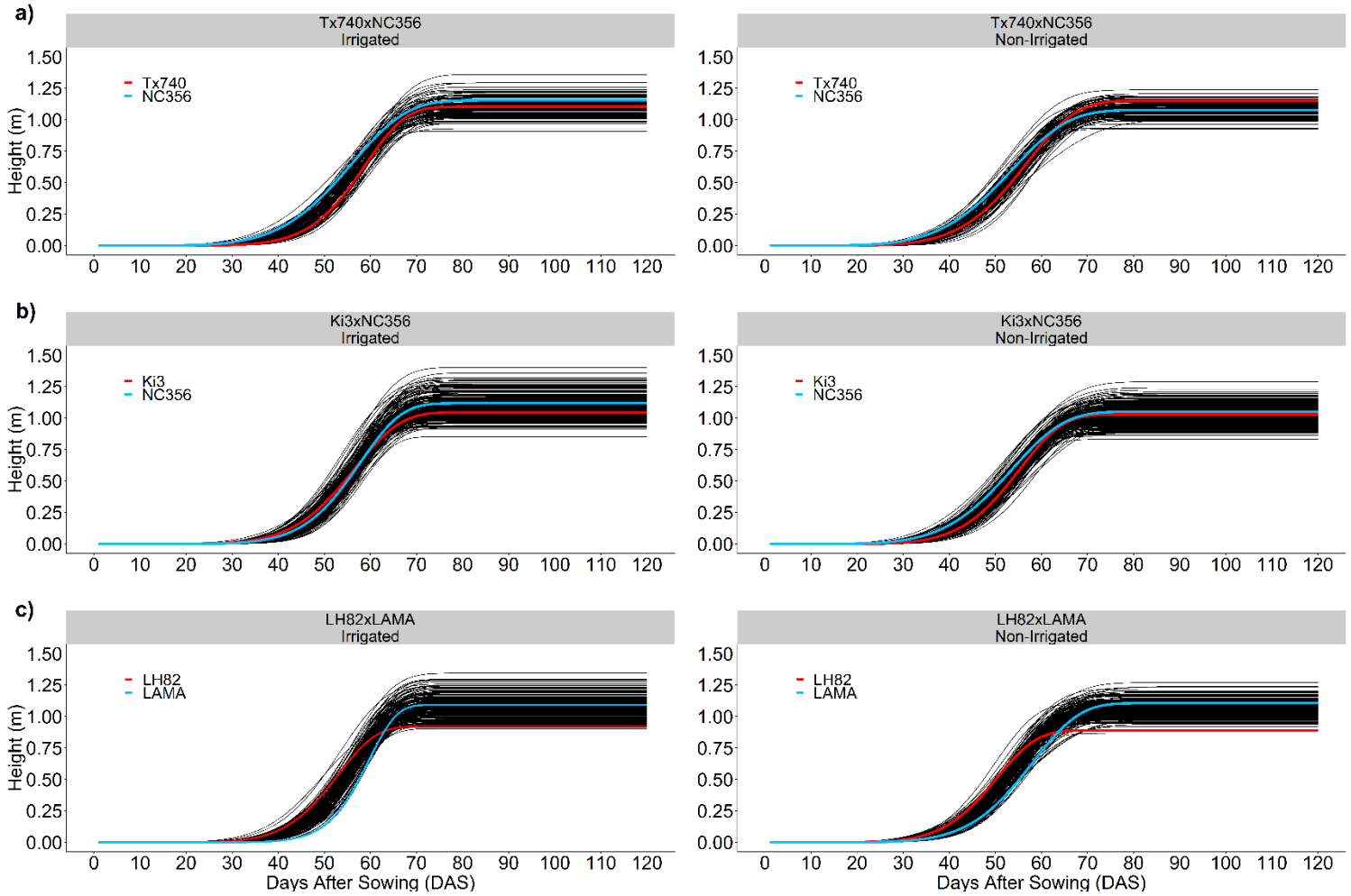

Figure 8. Fitted sigmoidal curves based off the Weibull function (Eq. [3]) of each entry within each population: **[a]** Tx740xNC356, **[b]** Ki3xNC356, and **[c]** LH82xLAMA. Female parent is represented by the red line and the male parent is represent by the blue line.

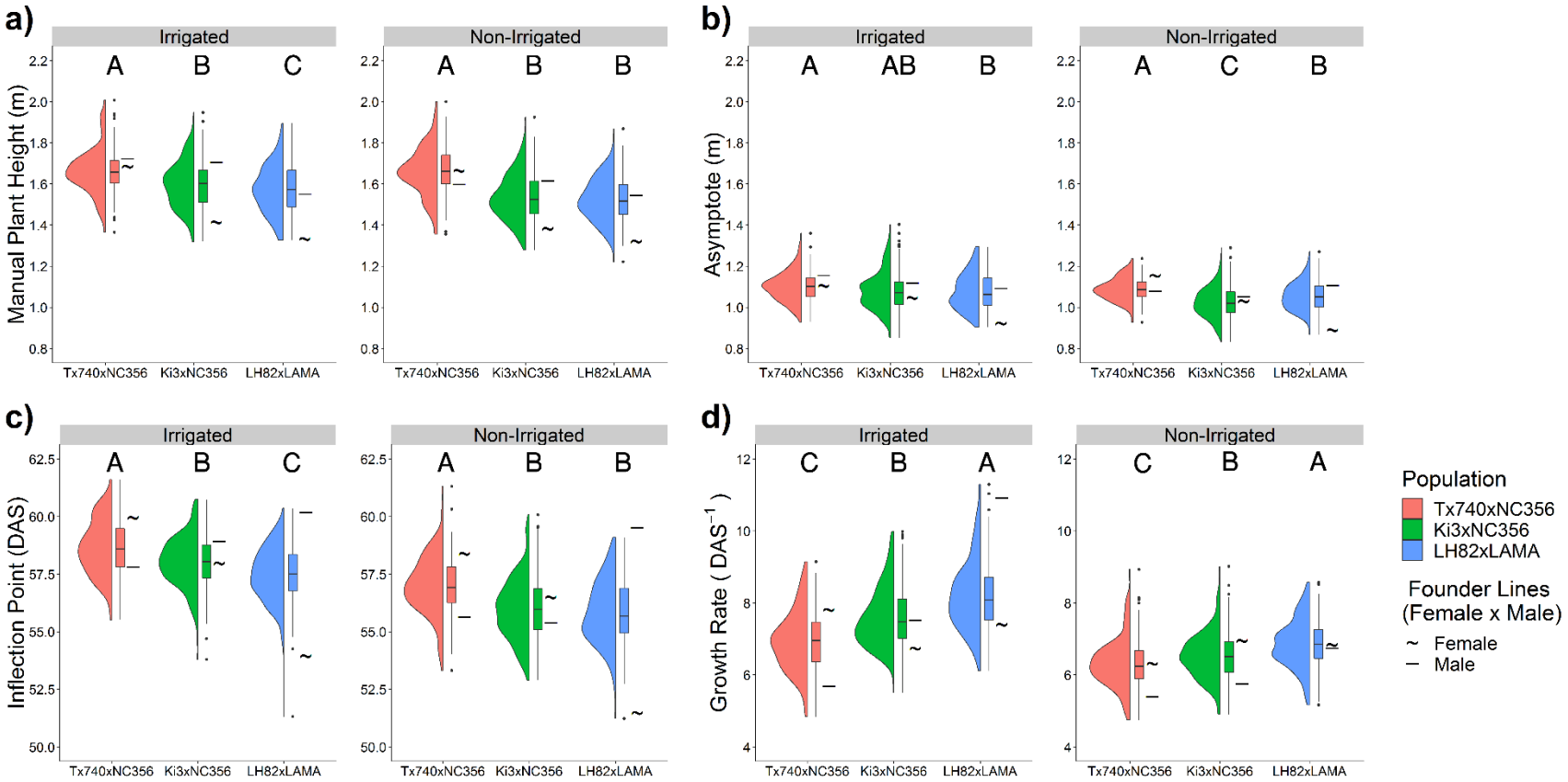

Figure 9. Boxplots summarizing entry BLUPS of **[a]** manual terminal plant height, **[b]** Weibull asymptote, **[c]** Weibull inflection point, and **[d]** Weibull growth rate for each mapping population (Tx740xNC356, Ki3xNC356, and LH82xLAMA) within each irrigation regimen (irrigated vs. non-irrigated). Histograms to the left of the boxplot represent the distribution of the data and symbols to the right depict the phenotypes of the female (~) and male (-) parents of each population. Letter define significant differences in means at α=0.05.

of the inbred lines adaptable to central Texas. Significant differences were found across all populations (1.02-1.09 m) within the non-irrigated trial (Figure 9b).

In comparison, PHT_{TMRL} was significantly different across populations (1.66, 1.59, and 1.57 m) under irrigated conditions for Tx740xNC356, Ki3xNC356, and LH82xLAMA, respectively. Tx740xNC356 (1.65 m) was significantly taller than the other populations (1.54 and 1.52 m) under the non-irrigated treatment (Figure 9a). The reduced means of the asymptote demonstrates the inherent biases of UAS estimation of plant height in maize compared with manual measurements. The ~0.5 m underestimate of height is slightly higher but within the range of previous studies in hybrid maize at similar flight altitudes (120 m). We speculate that the combination of flight altitude combined with reduced plant canopy density of the inbreds (as opposed to hybrids reported in past studies) influenced the UAS bias towards shorter estimates. Bias aside, numerical rankings between asymptote and PHT_{TRML} were consistent in ranking Tx740xNC356, Ki3xNC356, and LH82xLAMA population means from tallest to shortest and Pearson correlations (r) (Irrigated: 77, 74, and 74%; Non-Irrigated: 66, 72, and 74%; Appendix B10, Appendix B11, and Appendix B12) indicated highly significant (α=0.05), positive linear correlations between UAS asymptotes estimates and PHT_{TRML} measurements.

Significant differences were found between each population's mean for inflection point (58.6, 58.0, and 57.5 d for Tx740xNC356, Ki3xNC356, and LH82xLAMA) within the irrigated trial while Tx740xNC356 (60.0 d) was significantly (α=0.05) one day later in the non-irrigated trials (Figure 9c). Comparison of irrigation treatments demonstrated that limiting abiotic stress caused by water limitation delayed the inflection point by two days on average across the populations. Inflection point had low positive correlations to PHT_{TRML}

(Irrigated: 30, 27, and 34%; Non-Irrigated: 2, 22, and 24%; Appendix B10, Appendix B11, and Appendix B12) with high correlations to flowering time (DTA/DTS) (Irrigated: 60/45, 59/58, and 64/59%; Non-Irrigated: 61/56, 55/53, and 68/66%; Appendix B10, Appendix B11, and Appendix B12). Correlations between inflection points and UAS P95 estimates by flight date consistently demonstrated a high negative correlation to PHT estimates during the early season that gradually progressed toward a positive correlation ~10 days after the mean inflection point (Appendix B10, Appendix B11, and Appendix B12). We hypothesize that the later inflection points demonstrate extended vegetative growth periods leading to taller plants, indicating the possibility of pleiotropic QTL across the functional curve parameters. Since the correlation is high but not perfect we hypothesize that taller genotypes with earlier inflection points could potentially indicate better fitness in stressful environments, as they are determined to reach their terminal height quickly.

The growth rate parameter, which influences the steepness of the Weibull curve, was significantly different in its means across the populations in both environments (Irrigated: 6.9, 7.6, and 8.2 DAS^{-1}; Non-irrigated: 6.3, 6.5, and 6.8 DAS^{-1}), though a greater range of the means was present in the irrigated trial (Figure 9d). Using the first derivative of the Weibull function the absolute growth rate (AGR) was calculated at the inflection point which equates to the maximum growth rate of the curves. Significant differences were found in the maximum AGR across populations within the irrigated trial (48, 52, and 56 mm day^{-1}) and LH82xLAMA was 3 mm day^{-1} greater than the other populations in the non-irrigated trial. Comparison across irrigation trials demonstrates a 4, 7, and 8 mm day^{-1} reduction in absolute growth rate within the non-irrigated trial for Tx740xNC356, Ki3xNC356, and LH82xLAMA, respectively.

3.3.3 QTL Mapping

3.3.3.1 Manual Terminal Height Associations

Nine QTL were identified for PHT_{TRML} across the three populations and two environments (Table 1) with genetic variation explained of each ranging from 5.1 to 9.4%. All PHT_{TRML} associations had an additive effect of ~3 cm (Table 5). One region of interest was identified across two populations *q*1_172 (LH82xLAMA; irrigated) and *q*1_176 (Tx740xNC356; non-irrigated), localizing to the 280 to 284 Mbs region of chromosome 1. We identified a single genomic region, 98 to 128 Mbs on chromosome 2 that co-localized within the same genetic background (Ki3xNC356) across different environmental treatments (*q*2_70 irrigated and *q*2_69 non-irrigated). The limited co-localization of QTLs across genetic populations demonstrates the difficulty of identifying genomic regions that can be utilized in genetic backgrounds beyond those they were discovered within. They also demonstrated a lack of statistical power in the smaller of the three populations Tx740xNC356 (n=110). It has been empirically shown that population size is the most critical factor in QTL linkage mapping (Anderson, et al., 2018).

3.3.3.2 Functional Parameter Associations

A main intention of this study was to evaluate the use of UAS estimates in modeling temporal growth of maize for the purpose of identifying dynamic QTL (Wu and Lin, 2006). Analysis of QTLs using functional parameters of the Weibull curve as phenotypes identified 13, 9, and 12 significant associations with the asymptote, growth rate, and inflection point, respectively (Appendix A8). Asymptote QTLs explained genetic variation ranging from 3.4% to 14.3% with additive effects ranging from 2 to 5 cm, consistent with PHT_{TRML}. High correlations between asymptote and PHT_{TRML} indicated that similar QTL should be detected

Table 5. Summary of QTL identified using manual terminal plant height as the associated phenotype.

Population	Trt†	Chromosome	Position (cM)	LOD§	PVE‡	Add (m)¶	Left Marker Position (cM)	Right Marker Position (cM)	Left Marker Position (bp)	Right Marker Position (bp)
Ki3xNC356	D	2	69	4.3	8.2	-0.03	68.5	69.5	98,935,095	101,781,010
Ki3xNC356	D	8	12	3.0	5.6	-0.03	10.5	13.5	5,024,449	5,912,287
Ki3xNC356	I	2	70	3.0	5.8	-0.03	69.5	70.5	113,899,778	127,959,743
Ki3xNC356	I	6	62	2.6	5.1	-0.03	61.5	62.5	148,942,282	149,680,023
Ki3xNC356	I	8	14	2.9	5.5	-0.03	13.5	15.5	6,810,510	7,748,559
LH82xLAMA	D	3	86	2.8	6.4	0.03	85.5	86.5	169,071,582	169,218,337
LH82xLAMA	I	1	172	2.8	6.4	-0.03	171.5	172.5	280,342,748	280,578,622
LH82xLAMA	I	8	65	2.2	6	-0.03	61.5	66.5	125,523,343	128,428,318
Tx740xNC356	D	1	176	2.0	9.4	-0.04	171.5	178.5	281,709,021	283,430,713

† Trt: Irrigation regimen; irrigated (I) and non-irrigated (D).
§ LOD: Logarithm of odds calculated as LOD = $-\log_{10}$(p-value).
‡ PVE: Prevent variation explained.
¶ Add: Estimated additive effect size of the QTL.

Table 6. Selective summary of QTL identified using fitting parameters asymptote (Asym), inflection point (IP), and growth rate (GR) of the sigmoidal curve as the associated phenotypes. QTL presented are within 1 Mbp of a plausible candidate gene.

Population	Trt†	Trait	Chr§	Position (cM)	Left Marker Position (bp)	Right Marker Position (bp)	Gene/QTL < 1Mbp	Function
Ki3xNC356	I	Asym	4	61	156,517,564	156,384,593	GRMZM2G134023	Brassinosteroid-responsive RING-H2
Ki3xNC356	I	IP	4	61	156,384,593	156,517,564	GRMZM2G134023	Brassinosteroid-responsive RING-H2
Ki3xNC356	D	IP	4	119	237,391,404	237,610,499	AC196708.3_FG006	SAUR-like auxin-responsive protein family
Ki3xNC356	I	IP	4	119	237,391,404	237,610,499	AC196708.3_FG006	SAUR-like auxin-responsive protein family
LH82xLAMA	I	GR	2	117	212,246,084	212,544,633	GRMZM2G064941	Auxin efflux carrier family protein
LH82xLAMA	D	Asym	3	72	159,817,878	158,668,137	sdw2	Short plant (Neuffer, 1992)
LH82xLAMA	D	GR	9	14	5,289,590	6,124,392	GRMZM2G307440	Gibberellin receptor GID1L2
LH82xLAMA	D	GR	10	20	6,537,612	5,874,629	cr4	Crinkly4; short plant (Stinard and Robertson, 1987)
LH82xLAMA	D	IP	10	20	5,874,629	6,537,612	cr4	Crinkly4; short plant (Stinard and Robertson, 1987)
LH82xLAMA	D	Asym	10	58	136,247,247	136,083,608	GRMZM2G397684	Brassinosteroid-responsive RING-H2
LH82xLAMA	I	Asym	10	58	136,247,247	136,083,608	GRMZM2G397684	Brassinosteroid-responsive RING-H2
Tx740xNC356	D	IP	2	87	182,727,527	183,505,515	GRMZM2G045243	SAUR-like auxin-responsive protein family
Tx740xNC356	I	GR	5	119	205,748,909	206,263,616	GRMZM2G074267	Auxin efflux carrier family protein
Tx740xNC356	D	Asym	6	67	143,997,309	141,909,772	dwil1	Dwarf & irregular leaf1 (Jiang, et al., 2012)

† Trt: Irrigation regimen; irrigated (I) and non-irrigated (D).

§ Chr: Chromosome.

using the two phenotyping methods. Two PHT_{TRML} QTLs, *q*1_172 LH82xLAMA (irrigated) and *q*1_176 Tx740xNC356 (non-irrigated), co-localized with an asymptote QTL, *q*1_173 of LH82xLAMA (irrigated) (Table2). Additional co-localizations were found between *q*6_67 Tx740xNC356 (irrigated) asymptote and *q*6_62 Ki3xNC356 (irrigated) PHT_{TRML}, as well as, *q*8_10 LH82xLAMA (non-irrigated) asymptote with *q*8_14 Ki3xNC356 (irrigated) PHT_{TRML} and *q*8_12 Ki3xNC356 (non-irrigated) PHT_{TRML}.

Growth rate QTL each explained 5.6 to 15% of the genotypic variance with an additive effect ranging from 0.2 to 0.3 DAS^{-1} (Appendix A8). Inflection point QTL each explained 4.3 to 13% of the genotypic variance with an additive effect ranging from 0.2 to 0.5 d (Appendix A8). Irrigated Ki3xNC356 trial *q*4_61 and irrigated LH82xLAMA *q*1_173/*q*1_176 were associated with inflection point and asymptote, while non-irrigated LH82xLAMA *q*10_20 was associated with inflection point and growth rate (Table 6). The co-localization of QTL associated with multiple parameters of the sigmoidal growth function indicate that these regions more than others may have an effect on defining the overall developmental trajectory of maize height.

Multiple QTL were identified within the LH82xLAMA trials for PHT_{TRML}, asymptote, inflection point, and flowering time (DTA/DTS) within the 273 to 287 Mbs region of chromosome 1 and the 140 to 176 Mbs region of chromosome 3 (Table 5, Appendix A7 and Appendix A8). This region of chromosome 3 harbors ZmMADS69 (GRMZM2G171650; Chr3: 158979321..159007265), a regulator of flowering time with pleiotropic effects on plant height. ZmMADS69 has higher expression levels in temperate germplasm compared to tropical, which may explain why the region is identified in the temperate by tropical cross (Liang, et al., 2019), such as LH82xLAMA and others

(Anderson, et al., 2018; Hirsch, et al., 2014; Peiffer, et al., 2014). The identified region on chromosome 1 contains the viviparous8 (vp8; GRMZM2G010353; Chr1: 286390345..286398537) loci which has exhibits dwarfism due to reduced cell proliferation (Lv, et al., 2014). ZmMADS69 effect was not influenced by day length (Liang, et al., 2019) and vp8 exhibited normal plant hormone response (Lv, et al., 2014) demonstrating that these QTL may be deterministic QTL (dQTL) represented as the differential allelic variation which affect the whole growth process (Wu, et al., 2004) unaffected by environmental stimuli. Conducting temporal phenotyping on large scale multi-environment trials, such as the Genomes to Fields Intuitive (AlKhalifah, et al., 2018; Gage, et al., 2017), using a diverse association panel such as the nested association maize (NAM) populations (McMullen, et al., 2009) could further the scientific understanding of allelic variation of dQTL and biotic/abiotic stimuli of opportunistic QTL (oQTL) and their effects on growth trajectories.

3.3.3.3 Temporal QTL Expression

In addition to the three parameters of the Weibull function, height estimates were predicted daily from 20 to 85 DAS using the Weibull function on individual entry specific curve parameters to evaluate their change over time. A total of 58 significant QTLs were identified with 6, 5, 4, 10, 13, and 20 unique QTLs based on the position of the QTL peak for the irrigated Tx740xNC356, non-irrigated Tx740xNC356, irrigated Ki3xNC356, non-irrigated Ki3xNC356, irrigated LH82xLAMA and non-irrigated LH82xLAMA trials, respectively (Figure 10, Appendix A9). Comparison of mean physical distance between the left and right marker of each the 58 unique QTLs to the physical position of candidate genes demonstrated that 23 of the

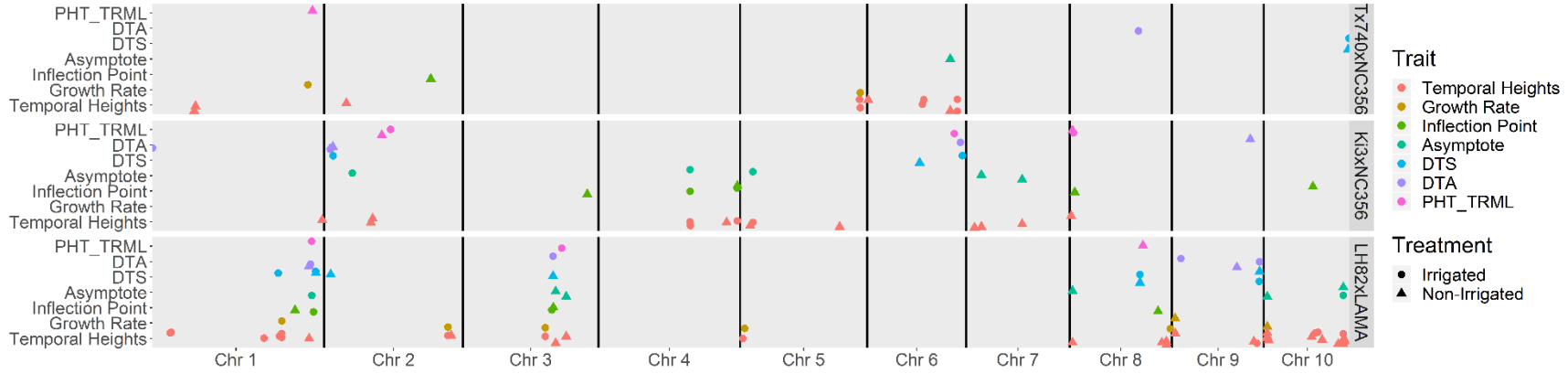

Figure 10. Summary of significant QTL identified for agronomic traits (PHT_TRML: Manual, terminal plant height; DTA: Days to anthesis; DTS: Days to silking), functional growth parameters (asymptote, inflection point, growth rate) and temporal height estimates from the Weibull curves. Temporal expression of temporal height QTL can be visualized in **Appendix B13**. Points indicate the mean physical location between the left and right flanking markers of the QTL.

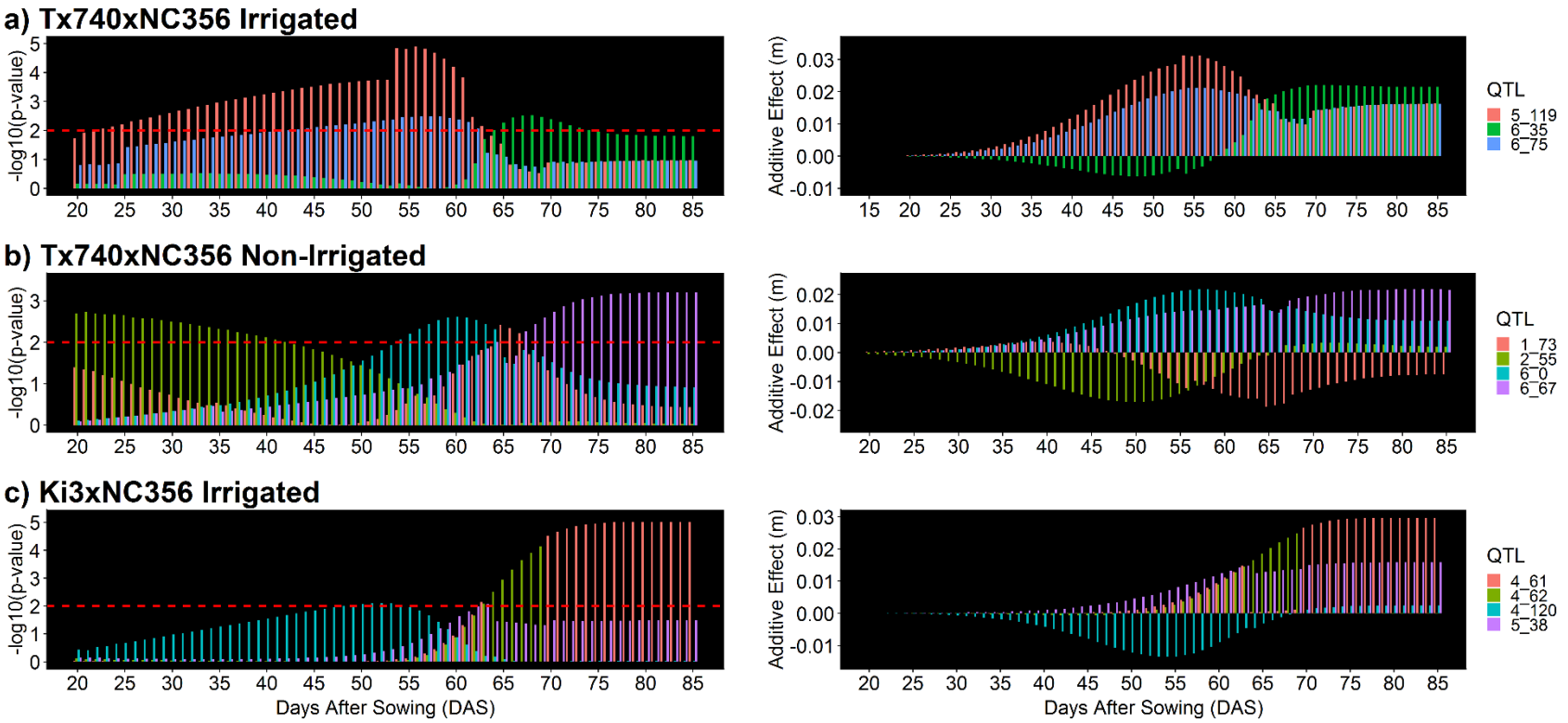

Figure 11. Temporal trends in QTL expression for the [a] Tx740xNC356 irrigated trial, [b] Tx740xNC356 non-irrigated trial, and [c] Ki3xNC356 irrigated trial. Bars are colored based on unique QTL (e.g. chromosome position) within each trial and represent the LOD score (left) or estimated additive effect (right) for each day from 20 to 85 DAS. Red dashed line represent significance threshold of LOD=2.

QTLs were within 1 Mbp of a candidate gene region and an additional 18 QTL were less than 5 Mbp from a candidate gene region.

Temporal analysis of the 58 unique QTLs identified through height estimates of the fitted sigmoidal curve demonstrated the dynamic nature of height QTL throughout the growing season. Within the irrigated Tx740xNC356 trial, q5_119 was detected from 22 to 62 DAS explaining 21% of the genetic variation at 54 DAS (Figure 10a, Appendix A9). In comparison, q5_35 of irrigated Tx740xNC356 trial was detected from 66 to 74 DAS explaining 11% of the genetic variation at 67 DAS (Figure 11a, Appendix A9, Appendix B13). Temporal QTL expression across environmental treatments (i.e. irrigation) demonstrated differential genomic localization while maintaining similarities in temporal expression for each population. Specifically, within the Tx740xNC356 population both irrigation regimens (i.e. environments) have a temporally broad QTL (*q*5_119 irrigated and *q*2_55 non- irrigated) prior to inflection point (~58 DAS), followed by QTLs detected at shorter temporal intervals after the inflection point. Additionally, trends in QTL temporal expression across populations exhibited unique temporal expression patterns. For example, Tx740xNC356 exhibited QTLs prior to the inflection point at early growth stages, whereas Ki3xNC356 exhibited no detectable QTLs until ~50 DAS.

Identified QTLs demonstrated dynamic trends in additive phenotypic effect. In general, these results show that the additive effect found at the peak significance DAS of a temporal QTL is a result of the cumulative effect of a gradual increase in the effect size of each genomic region (Figure 11). QTLs with peak expression early within the season had significantly smaller additive effect estimates than at later points in the growing season; due to reduced overall variation across the individuals in the population at early growth stages

(e.g. Figure 11b *q*2_55). Temporally, we observed both additive effects of individual QTL either maintained a constant directional effect (Figure 11a; q5_119 and *q*6_75; Appendix A9) or switched effect directions within the growing season (q6_35). Understanding the biological basis of this switching phenomena would be both interesting and important for optimizing plant growth.

When discussing the implementation of identified QTL within marker assisted selection protocols, targeting consistent directional effects may result in greater gains than those of temporal bi-directional effects. The temporal effect size should first be validated through near isogenic lines or heterogeneous inbred families. However, we speculate that the temporal trend of the effect size, like many QTL effects will remain dependent on the genetic background, abiotic, and biotic interactions. Interval mapping across the entire linkage map demonstrated that directional changes in additive effect size are present throughout the growing season throughout the genome (Appendix B14). If temporal shifts in directional effect are valid and not due to over inflations via false positives and limited population size; statistical models accounting for directional effect shifts will be necessary to incorporate temporal datasets of dynamic, quantitative traits within prediction modeling (e.g. genomic selection).

3.4 Conclusion

In this study we present one of the first applications of UAS phenotyping of temporal growth across the growing season using UAS imagery on several genetic mapping populations. To our knowledge, this is first empirical study to expand beyond selective developmental time points (Wang, et al., 2019), evaluating functional and temporal QTL expression in maize throughout the growing season within a field-based environment. Four

of the most important findings were: (i) UAS height estimates of RIL mapping populations are highly heritable although less phenotypic variance was portioned to genetic components compared to PHT_{TRML}. (ii) Significant differences among the functional parameter phenotypes identified 32 functional QTL compared to the nine QTL identified by PHT_{TRML}. Limited co-localization between functional, temporal, and PHT_{TRML} QTL demonstrate novel genetic loci effecting the overall growth trajectory of maize. (iii) Temporal mapping of height estimates demonstrated unique dynamic patterns in QTL expression and effect sizes across different genetic background and environments. (iv) The additive effect of a QTL is a cumulative effect of a gradual increase in effect size of each genomic region. Efficient integration of temporal phenotyping via HTPP, such as UAS, will improve our scientific understanding of dynamic, quantitative traits and developmental trajectories of important agronomic crops leading to hypotheses to test in both breeding and fundamental plant biology.

CHAPTER IV

SUMMARY

Weekly unmanned aerial system (UAS) imagery was collected over the College Station, Texas 2017 Genomes to Fields (G2F) hybrid trial, across three environmental stress treatments, using two UAS platforms. The high-altitude (120 m) fixed wing platform increased the fraction of variation attributed to genetics and had highly repeatable (R: >60%) height estimates, increasing genetic variance explained (10-40%) over traditional terminal height measurement (PHT_{TRML}; ~30%), as well as, over the low-altitude rotary wing UAS platform (10-20%). A logistic function reduced the dimensionality (>20 flights) of each UAS dataset to three parameters (inflection point, growth rate, and asymptote) and produced a more robust predictive model than independent flight dates, effectively summarizing (R^2>0.98) the UAS flight dates. The logistic model overcame the need to use specific flight dates when comparing different environments. UAS height estimates (r = 0.36-0.48) doubled the correlations to grain yield in this G2F experiment compared to PHT_{TRML} (r = 0.23-0.28). Parameters of the logistical function achieved equivalent correlations (r = 0.30-0.46) to individual flight dates (r = 0.36-0.48), improving grain yield prediction in this study by ~400% (R^2= 0.25-0.34) over PHT_{TRML} (R^2 = 0.06-0.08). Incorporating other UAS derived parameters beyond plant height, such as vegetation indicies, may allow yield to be accurately predicted before maturity, speeding breeding programs. A new public R function to generate ESRI shapefiles for plot research was also described.

Using three bi-parental RIL mapping populations, Tx740xNC356, Ki3xNC356, and LH82xLAMA, we evaluated the ability of UAS imagery to estimate plant heights within

inbred germplasm. Temporal UAS surveying fit sigmoidal Weibull growth curves (R^2>0.99 and mean RMSE ranging from 2.4 to 3.7 cm) to summarize the growth trajectories of each genetic entry. Significant differences were identified between the populations and irrigation regimens for function growth parameter (asymptote, inflection point, and growth rate) signifying the presence of differential QTL expression throughout the growing season. Inclusive composite interval mapping was performed on PHT_{TRML} measurements identifying nine significant QTL. Using functional growth parameters 34 significant QTL were with 3 to 15% genetic variation explained. Few functional QTL co-localized with PHT_{TRML} demonstrating unique genomic regions which may have an effect on the overall growth trajectory of maize. Height was estimated at one-day intervals to 85 DAS using the Weibull function, identifying 58 unique temporal peak QTL locations. Temporal QTL expression demonstrated all of the identified significant QTL to have dynamic expression patterns (i.e., no QTL were found with permanent significant expression through the entire growing season). Allelic effect estimates of significant temporal QTL demonstrated the dynamic nature of QTL effect size, which gradually increased with QTL expression. Permanent directional additive effect was identified for the majority of QTL, although one-directional scanning of the entire linkage map demonstrated that directional changes in additive effect size are present throughout the growing season throughout the genome.

4.1 Reflection

Three years of experience implementing UAS within the maize breeding program at Texas A&M has seen great scientific progress towards everyday usage as a phenotyping platform. We have advanced from small scale validation trials (<40 plot) trials to surveying several hectares of inbred and hybrid trials for QTL mapping, indirect selection, and novel

trait discovery. This research presented the challenge of effectively communicating ideas and research objective across diverse disciplines towards common goals. Each research group has unique research objectives and interest which the collaborative group as a whole needs to keep in mind and work towards to maintain engagement from all parties. In all, this doctoral research has demonstrated successful implementation of UAS phenotyping within a maize breeding program. The direct collaboration across diverse disciplines has created a novel scientific community of experts specialized in implementation of remote sensing technologies within plot-based agriculture systems.

The Texas A&M UAS project relied heavily on remote sensing, geoscience, and agricultural engineering collaborators for tedious, melancholy data collection and image processing. Although this was critical during the initial implementation of UAS phenotyping, if a research group plans to use UAS for the foreseeable future they should look towards in-house data collection and processing. Same day image processing, rather than quality analysis of an entire growing season of UAS surveys after that fact, will be critical to consistent collection of high data quality. Rapid turn-around of image processing, followed by QC/QA allows for identification of data issues within an actionable timeframe so solutions can be proposed and implemented during the same growing season rather than looking towards the next season.

One of the most consistent issue we encountered with image processing was failure of image stitching and key point matching for point cloud construction. We hypothesis that the failures of image processing were a result of the homogeneous canopy structure and reduce frame of reference of low altitude (25 m) images. We attempted to resolve the stitching issues through increased GCP representation, with limited quality improvement.

We are currently conducting flights at 25, 40, 60, and 80 m with the rotary wing platform to determine the optimal flying altitudes which result in high quality image processing. In hindsight, this experiment should have been conducted as soon as the image stitching issues were first identified but will prove critical to identifying optimal flight altitudes. Furthermore, this study should help to identify critical flight altitudes at different growth stages of maize and result in reduced flight accompanied with image processing issues.

Upon reflection if I could go back and make changes to my doctoral research several ideas come to mind. First, I entered the project during the second year of UAS implementation. In hindsight I would have started working with UAS during the first year as the transition into the remote sensing field was challenging and further delayed the pipeline development and data extraction timeline. Second, height estimates presented a unique set of challenges but most of them were due to lack of knowledge and experience with remote sensing datasets. If I were to go back I would have expanded my analysis to additional image-based phenotypes beyond height. In reference to chapter II, the indirect selection of grain yield may have seen significant improvement and with the inclusion of additional imaged based phenotypes. Third, chapter III identified unique trends in marker-trait associations throughout the growing season. Due to the limited sample size of the mapping populations and limited detection of associated loci across genetic backgrounds and environments; implementation of findings would need extensive validation and lead to limited direct application. If I could go back I would have taken a genomic selection approach combining temporal UAS data with marker information to predict and advance relevant genetic materials focused on improving the genetic gains within the maize breeding program.

4.2 Future Direction of Research

Full implementation of UAS phenotyping demands accurate and consistent data collection. Future work will continue to understand data collection methods (e.g., flight altitudes, weather conditions, new UAV platforms, etc.) towards identifying optimal parameters/conditions to collect consistent, informative imagery. Improvements in stereoscopic image collection or swarm based UAS surveys will further improve our data collection quality. Ongoing work is being conducted in collaboration with statistics colleagues to improve spatial variance estimates and predict growth trajectories based on early season data. Additionally, predictive modeling will be expanded to a greater variety of image based phenotypes to identify optimal combinations that maximize the predictable variance in grain yield.

The G2F experiment was an excellent opportunity to demonstrate proof of concepts finding but has limited genetic material relevant to the Texas maize breeding program. Optimal predictive models will be developed and applied to trials relevant to genetic improvement of the breeding program's germplasm. Efforts will be turned to direct application within the breeding program through training and validation trials, accompanied with multi-year trials to evaluate genetic gain based on phenomic selection. Furthermore, continual evaluation of improved light weight sensor technologies (LiDAR, hyper-spectral, thermal) will be evaluated for novel phenotypes and everyday utilization within agriculture.

REFERENCES

Aasen, H., A. Burkart, A. Bolten and G. Bareth. 2015. Generating 3D hyperspectral information with lightweight UAV snapshot cameras for vegetation monitoring: From camera calibration to quality assurance. ISPRS Journal of Photogrammetry and Remote Sensing 108: 245-259.

AgiSoft PhotoScan Professional. 2016. (Version 1.2.6) (Software). Retrieved from http://www.agisoft.com/downloads/installer/.

AlKhalifah, N., D.A. Campbell, C.M. Falcon, J.M. Gardiner, N.D. Miller, M.C. Romay, et al. 2018. Maize Genomes to Fields: 2014 and 2015 field season genotype, phenotype, environment, and inbred ear image datasets. BMC Research Notes 11: 452.

Anderson, S.L., A.L. Mahan, S.C. Murray and P.E. Klein. 2018. Four parent maize (FPM) population: Effects of mating designs on linkage disequilibrium and mapping quantitative traits. The Plant Genome 11. doi:10.3835/plantgenome2017.11.0102.

Anderson, S.L., S. Murray, L. Malambo, C. Ratcliff, S. Popescu, D. Cope, et al. 2019. Prediction of maize grain yield before maturity using improved temporal height estimates of unmanned aerial systems. The Plant Phenome Journal 2. doi:10.2135/tppj2019.02.0004.

Araus, J.L. and J.E. Cairns. 2014. Field high-throughput phenotyping: the new crop breeding frontier. Trends in Plant Science 19: 52-61.

Araus, J.L. and S.C. Kefauver. 2018. Breeding to adapt agriculture to climate change: affordable phenotyping solutions. Current Opinion in Plant Biology 45: 237-247.

Araus, J.L., S.C. Kefauver, M. Zaman-Allah, M.S. Olsen and J.E. Cairns. 2018. Translating high-throughput phenotyping into genetic gain. Trends in Plant Science 23(5): 451-466.

Archontoulis, S.V. and F.E. Miguez. 2015. Nonlinear regression models and applications in agricultural research. Agronomy Journal 107: 786-798.

Axelsson, P. 1999. Processing of laser scanner data—algorithms and applications. ISPRS Journal of Photogrammetry and Remote Sensing 54: 138-147.

Axelsson, P. 2000. DEM generation from laser scanner data using adaptive TIN models. International Archives of Photogrammetry and Remote Sensing 33: 110-117.

Baltsavias, E.P. 1999. A comparison between photogrammetry and laser scanning. ISPRS Journal of Photogrammetry and Remote Sensing 54: 83-94.

Bareth, G., J. Bendig, N. Tilly, D. Hoffmeister, H. Aasen and A. Bolten. 2016. A comparison of UAV-and TLS-derived plant height for crop monitoring: using polygon grids for the analysis of crop surface models (CSMs). Photogrammetrie-Fernerkundung-Geoinformation 2016: 85-94.

Bendig, J., A. Bolten and G. Bareth. 2013. UAV-based imaging for multi-temporal, very high resolution crop surface models to monitor crop growth variability monitoring des Pflanzenwachstums mit Hilfe multitemporaler und hoch auflösender Oberflächenmodelle von Getreidebeständen auf Basis von Bildern aus UAV-Befliegungen. Photogrammetrie-Fernerkundung-Geoinformation 2013: 551-562.

Bendig, J., A. Bolten, S. Bennertz, J. Broscheit, S. Eichfuss and G. Bareth. 2014. Estimating biomass of barley using crop surface models (CSMs) derived from UAV-based RGB imaging. Remote Sensing 6: 10395-10412.

Burkart, A., V. Hecht, T. Kraska and U. Rascher. 2018. Phenological analysis of unmanned aerial vehicle based time series of barley imagery with high temporal resolution. Precision Agriculture 19: 134-146.

Chang, A., J. Jung, M.M. Maeda and J. Landivar. 2017. Crop height monitoring with digital imagery from unmanned aerial system (UAS). Computers and Electronics in Agriculture 141: 232-237.

Chen, D.-H. and P. Ronald. 1999. A rapid DNA minipreparation method suitable for AFLP and other PCR applications. Plant Molecular Biology Reporter 17: 53-57.

Chen, Y. 2016. High-density linkage map construction, mapping of agronomic traits in tropical maize (Zea Mays L.) and validating SNPs controlling maize grain yield and plant height in southern hybrid testcrosses. Doctoral dissertation. Texas A&M University. Available electronically from http : / /hdl .handle .net /1969 .1 /158620.

Chen, Z., B. Gao and B. Devereux. 2017. State-of-the-art: DTM generation using airborne LIDAR data. Sensors 17: 150.

Chu, T., M.J. Starek, M.J. Brewer, S.C. Murray and L.S. Pruter. 2018. Characterizing canopy height with UAS structure-from-motion photogrammetry—results analysis of a maize field trial with respect to multiple factors. Remote Sensing Letters 9: 753-762.

De Souza, C.H.W., R.A.C. Lamparelli, J.V. Rocha and P.S.G. Magalhães. 2017. Height estimation of sugarcane using an unmanned aerial system (UAS) based on structure from motion (SfM) point clouds. International Journal of Remote Sensing 38: 2218-2230.

Deery, D., J. Jimenez-Berni, H. Jones, X. Sirault and R. Furbank. 2014. Proximal remote sensing buggies and potential applications for field-based phenotyping. Agronomy 4: 349-379.

Duvick, D., J. Smith and M. Cooper. 2004. Long-term selection in a commercial hybrid maize breeding program. Plant Breeding Reviews 24: 109-152.

Duvick, D.N. 1997. Heterosis: feeding people and protecting natural resources. Book of Abstracts. The Genetics and Exploitation of Heterosis in Crops; An International Symposium. . CIMMYT, Mexico, D.F., Mexico. . p. 19-29.

Farfan, I.D.B., N. Gerald, S.C. Murray, T. Isakeit, P.-C. Huang, M. Warburton, et al. 2015. Genome wide association study for drought, aflatoxin resistance, and important agronomic traits of maize hybrids in the sub-tropics. PloS One 10: e0117737.

Farfan, I.D.B., S.C. Murray, S. Labar and D. Pietsch. 2013. A multi-environment trial analysis shows slight grain yield improvement in Texas commercial maize. Field Crops Research 149: 167-176.

Furbank, R.T. and M. Tester. 2011. Phenomics–technologies to relieve the phenotyping bottleneck. Trends in Plant Science 16: 635-644.

Gage, J.L., D. Jarquin, C. Romay, A. Lorenz, E.S. Buckler, S. Kaeppler, et al. 2017. The effect of artificial selection on phenotypic plasticity in maize. Nature Communications 8: 1348. doi:10.1038/s41467-017-01450-2.

Gao, S., Z. Niu, G. Sun, D. Zhao, K. Jia and Y. Qin. 2015. Height extraction of maize using airborne full-waveform LIDAR data and a deconvolution algorithm. IEEE Geoscience and Remote Sensing Letters 12: 1978-1982.

Gaut, B.S. 2001. Patterns of chromosomal duplication in maize and their implications for comparative maps of the grasses. Genome Research 11: 55-66.

Geipel, J., J. Link and W. Claupein. 2014. Combined spectral and spatial modeling of corn yield based on aerial images and crop surface models acquired with an unmanned aircraft system. Remote Sensing 6: 10335-10355.

Girardeau-Montaut, D. 2016. CloudCompare. Version 2.8 [computer software]. https://www.danielgm.net/cc/.

Gonda, I., H. Ashrafi, D.A. Lyon, S.R. Strickler, A.M. Hulse-Kemp, Q. Ma, et al. 2018. Sequencing-based bin map construction of a tomato mapping population, facilitating high-resolution quantitative trait loci detection. The Plant Genome 12.

Granshaw, S.I. 2016. Photogrammetric terminology. The Photogrammetric Record 31: 210-252.

Grassini, P., K.M. Eskridge and K.G. Cassman. 2013. Distinguishing between yield advances and yield plateaus in historical crop production trends. Nature communications 4: 2918.

Hafner, S. 2003. Trends in maize, rice, and wheat yields for 188 nations over the past 40 years: a prevalence of linear growth. Agriculture, Ecosystems & Environment 97: 275-283.

Han, L., G. Yang, H. Dai, B. Xu, H. Yang, H. Feng, et al. 2019. Modeling maize above-ground biomass based on machine learning approaches using UAV remote-sensing data. Plant Methods 15: 10.

Han, L., G. Yang, H. Yang, B. Xu, Z. Li and X. Yang. 2018. Clustering field-based maize phenotyping of plant-height growth and canopy spectral dynamics using a UAV remote-sensing approach. Frontiers in Plant Science 9: 1638.

Han, X., J.A. Thomasson, G.C. Bagnall, N. Pugh, D.W. Horne, W.L. Rooney, et al. 2018. Measurement and calibration of plant-height from fixed-wing UAV images. Sensors 18: 4092.

Hartwig, T., G.S. Chuck, S. Fujioka, A. Klempien, R. Weizbauer, D.P.V. Potluri, et al. 2011. Brassinosteroid control of sex determination in maize. Proceedings of the National Academy of Sciences 108: 19814-19819.

Hirsch, C.N., J.M. Foerster, J.M. Johnson, R.S. Sekhon, G. Muttoni, B. Vaillancourt, et al. 2014. Insights into the maize pan-genome and pan-transcriptome. The Plant Cell 26: 121-135.

2010. High-resolution Crop Surface Models (CSM) and Crop Volume Models (CVM) on field level by terrestrial laser scanning. Proc. SPIE.

Hofle, B. 2014. Radiometric correction of terrestrial LiDAR point cloud data for individual maize plant detection. IEEE Geoscience and Remote Sensing Letters 11: 94-98.

Holman, F.H., A.B. Riche, A. Michalski, M. Castle, M.J. Wooster and M.J. Hawkesford. 2016. High throughput field phenotyping of wheat plant height and growth rate in field plot trials using UAV based remote sensing. Remote Sensing 8: 1031.

Hu, P., S.C. Chapman, X. Wang, A. Potgieter, T. Duan, D. Jordan, et al. 2018. Estimation of plant height using a high throughput phenotyping platform based on unmanned aerial vehicle and self-calibration: Example for sorghum breeding. European Journal of Agronomy 95: 24-32.

Huang, C.R.L., K.H. Burns and J.D. Boeke. 2012. Active transposition in genomes. Annual Review of Genetics 46: 651-675.

Hunt Jr, E.R. and C.S. Daughtry. 2017. What good are unmanned aircraft systems for agricultural remote sensing and precision agriculture? International Journal of Remote Sensing 39: 5345-5376.

Hunter, M.C., R.G. Smith, M.E. Schipanski, L.W. Atwood and D.A. Mortensen. 2017. Agriculture in 2050: Recalibrating targets for sustainable intensification. BioScience 67: 386-391.

Isenburg, M. 2015. LAStools-efficient tools for LiDAR processing. Version 130506.

Jiang, F., M. Guo, F. Yang, K. Duncan, D. Jackson, A. Rafalski, et al. 2012. Mutations in an AP2 transcription factor-like gene affect internode length and leaf shape in maize. PLoS One 7: e37040.

Jiao, Y., P. Peluso, J. Shi, T. Liang, M.C. Stitzer, B. Wang, et al. 2017. Improved maize reference genome with single-molecule technologies. Nature 546: 524.

JMP®. 2018. Version 14.0.0. SAS Institute Inc., Cary, NC, 1989-2018.

Katsvairo, T.W., W.J. Cox and H.M. Van Es. 2003. Spatial growth and nitrogen uptake variability of corn at two nitrogen levels. Agronomy Journal 95: 1000-1011.

Keightley, K.E. and G.W. Bawden. 2010. 3D volumetric modeling of grapevine biomass using tripod LiDAR. Computers and Electronics in Agriculture 74: 305-312.

Korzeniowska, K., N. Pfeifer, G. Mandlburger and A. Lugmayr. 2014. Experimental evaluation of ALS point cloud ground extraction tools over different terrain slope and land-cover types. International Journal of Remote Sensing 35: 4673-4697.

Kraus, K. and N. Pfeifer. 1998. Determination of terrain models in wooded areas with airborne laser scanner data. ISPRS Journal of Photogrammetry and remote Sensing 53: 193-203.

Kraus, K. and N. Pfeifer. 2001. Advanced DTM generation from LIDAR data. International Archives Of Photogrammetry Remote Sensing And Spatial Information Sciences 34: 23-30.

1999. Processing of laser scanning data for wooded areas. Photogrammetric Week.

LAStools. 2017. Efficient LiDAR Processing Software. Version 170628, academic. http://rapidlasso.com/LAStools.

Lawit, S.J., H.M. Wych, D. Xu, S. Kundu and D.T. Tomes. 2010. Maize DELLA proteins dwarf plant8 and dwarf plant9 as modulators of plant development. Plant and Cell Physiology 51: 1854-1868.

Li, H., J.-M. Ribaut, Z. Li and J. Wang. 2008. Inclusive composite interval mapping (ICIM) for digenic epistasis of quantitative traits in biparental populations. Theoretical and Applied Genetics 116: 243-260.

Li, H., G. Ye and J. Wang. 2007. A modified algorithm for the improvement of composite interval mapping. Genetics 175: 361-374.

Li, W., Z. Niu, H. Chen, D. Li, M. Wu and W. Zhao. 2016. Remote estimation of canopy height and aboveground biomass of maize using high-resolution stereo images from a low-cost unmanned aerial vehicle system. Ecological Indicators 67: 637-648.

Li, W., Z. Niu, N. Huang, C. Wang, S. Gao and C. Wu. 2015. Airborne LiDAR technique for estimating biomass components of maize: A case study in Zhangye City, Northwest China. Ecological Indicators 57: 486-496.

Li, X., Z. Zhou, J. Ding, Y. Wu, B. Zhou, R. Wang, et al. 2016. Combined linkage and association mapping reveals QTL and candidate genes for plant and ear height in maize. Frontiers in Plant Science 7: 833.

Liang, Y., Q. Liu, X. Wang, C. Huang, G. Xu, S. Hey, et al. 2019. Zm MADS 69 functions as a flowering activator through the ZmRap2. 7-ZCN 8 regulatory module and contributes to maize flowering time adaptation. New Phytologist 221: 2335-2347.

Lin, Y. 2015. LiDAR: An important tool for next-generation phenotyping technology of high potential for plant phenomics? Computers and Electronics in Agriculture 119: 61-73.

Link, J., D. Senner and W. Claupein. 2013. Developing and evaluating an aerial sensor platform (ASP) to collect multispectral data for deriving management decisions in precision farming. Computers and Electronics in Agriculture 94: 20-28.

Lumme, J., M. Karjalainen, H. Kaartinen, A. Kukko, J. Hyyppä, H. Hyyppä, et al. 2008. Terrestrial laser scanning of agricultural crops. The International Archives of the Photogrammetry, Remote Sensing and Spatial Information Sciences 37: 563-566.

Lv, H., J. Zheng, T. Wang, J. Fu, J. Huai, H. Min, et al. 2014. The maize d2003, a novel allele of VP8, is required for maize internode elongation. Plant Molecular Biology 84: 243-257.

Ma, C.-X., G. Casella and R. Wu. 2002. Functional mapping of quantitative trait loci underlying the character process: a theoretical framework. Genetics 161: 1751-1762.

Machado, S., E. Bynum, T. Archer, R. Lascano, L. Wilson, J. Bordovsky, et al. 2002. Spatial and temporal variability of corn growth and grain yield. Crop Science 42: 1564-1576.

Mahan, A.L., S.C. Murray and P.E. Klein. 2018. Four-parent maize (FPM) population: Development and phenotypic characterization. Crop Science 58: 1106-1117.

Makarevitch, I., A. Thompson, G.J. Muehlbauer and N.M. Springer. 2012. Brd1 gene in maize encodes a brassinosteroid C-6 oxidase. PloS One 7: e30798.

Malambo, L., S. Popescu, S. Murray, E. Putman, N. Pugh, D. Horne, et al. 2018. Multitemporal field-based plant height estimation using 3D point clouds generated from small unmanned aerial systems high-resolution imagery. International Journal of Applied Earth Observation and Geoinformation 64: 31-42.

Mallarino, A., E. Oyarzabal and P. Hinz. 1999. Interpreting within-field relationships between crop yields and soil and plant variables using factor analysis. Precision Agriculture 1: 15-25.

Mayfield, K., F.J. Betrán, T. Isakeit, G. Odvody, S.C. Murray, W.L. Rooney, et al. 2012. Registration of maize germplasm lines Tx736, Tx739, and Tx740 for reducing preharvest aflatoxin accumulation. Journal of Plant Registrations 6: 88-94.

McGaughey, R. 2016. FUSION/LDV: Software for LIDAR data analysis and visualization. October 2016–FUSION Version 3.60+. Pacific Northwest Research Station, United States Department of Agriculture Forest Service. Google Scholar.

McGaughey, R.J. 2009. FUSION/LDV: Software for LIDAR data analysis and visualization. US Department of Agriculture, Forest Service, Pacific Northwest Research Station: Seattle, WA, USA 123.

McMullen, M.D., S. Kresovich, H.S. Villeda, P. Bradbury, H. Li, Q. Sun, et al. 2009. Genetic properties of the maize nested association mapping population. Science 325: 737-740.

Meng, X., N. Currit and K. Zhao. 2010. Ground filtering algorithms for airborne LiDAR data: A review of critical issues. Remote Sensing 2: 833-860.

Miguez, F.E., M.B. Villamil, S.P. Long and G.A. Bollero. 2008. Meta-analysis of the effects of management factors on Miscanthus × giganteus growth and biomass production. Agricultural and Forest Meteorology 148: 1280-1292.

Montealegre, A.L., M.T. Lamelas and J. de la Riva. 2015. A comparison of open-source LiDAR filtering algorithms in a Mediterranean forest environment. IEEE Journal of Selected Topics in Applied Earth Observations and Remote Sensing 8: 4072-4085.

Multani, D.S., S.P. Briggs, M.A. Chamberlin, J.J. Blakeslee, A.S. Murphy and G.S. Johal. 2003. Loss of an MDR transporter in compact stalks of maize br2 and sorghum dw3 mutants. Science 302: 81-84.

Muraya, M.M., J. Chu, Y. Zhao, A. Junker, C. Klukas, J.C. Reif, et al. 2017. Genetic variation of growth dynamics in maize (Zea mays L.) revealed through automated non-invasive phenotyping. The Plant Journal 89: 366-380.

Neuffer, M. 1992. Location and designation of 8 dominant mutants from chemical mutagenesis and spontaneous origin. Maize Genet. Coop. News Lett 66: 39-40.

Neumann, K., Y. Zhao, J. Chu, J. Keilwagen, J.C. Reif, B. Kilian, et al. 2017. Genetic architecture and temporal patterns of biomass accumulation in spring barley revealed by image analysis. BMC Plant Biology 17: 137.

Niu, Q., H. Feng, G. Yang, C. Li, H. Yang, B. Xu, et al. 2018. Monitoring plant height and leaf area index of maize breeding material based on UAV digital images. Transactions of the Chinese Society of Agricultural Engineering 34: 73-82.

Paine, C., T.R. Marthews, D.R. Vogt, D. Purves, M. Rees, A. Hector, et al. 2012. How to fit nonlinear plant growth models and calculate growth rates: an update for ecologists. Methods in Ecology and Evolution 3: 245-256.

Pauli, D., P. Andrade-Sanchez, A.E. Carmo-Silva, E. Gazave, A.N. French, J. Heun, et al. 2016. Field-based high-throughput plant phenotyping reveals the temporal patterns of quantitative trait loci associated with stress-responsive traits in cotton. G3: Genes| Genomes| Genetics 6: 865-879.

Pauli, D., S.C. Chapman, R. Bart, C.N. Topp, C.J. Lawrence-Dill, J. Poland, et al. 2016. The quest for understanding phenotypic variation via integrated approaches in the field environment. Plant Physiology 172: 622-634.

Peiffer, J.A., M.C. Romay, M.A. Gore, S.A. Flint-Garcia, Z. Zhang, M.J. Millard, et al. 2014. The genetic architecture of maize height. Genetics 196: 1337-1356.

Perez-Sanz, F., P.J. Navarro and M. Egea-Cortines. 2017. Plant phenomics: an overview of image acquisition technologies and image data analysis algorithms. GigaScience 6.

Pfeifer, N. and G. Mandlburger. 2009. LiDAR data filtering and DTM generation. CRC Press, Taylor and Francis Group, Boca Raton, Florida. p. 307-334.

Polat, N. and M. Uysal. 2015. Investigating performance of airborne LiDAR data filtering algorithms for DTM generation. Measurement 63: 61-68.

Prashar, A. and H.G. Jones. 2014. Infra-red thermography as a high-throughput tool for field phenotyping. Agronomy 4: 397-417.

Pugh, N., D.W. Horne, S.C. Murray, G. Carvalho, L. Malambo, J. Jung, et al. 2018. Temporal estimates of crop growth in sorghum and maize breeding enabled by unmanned aerial systems. The Plant Phenome Journal 1.

R Core Team. 2016. R: A language and environment for statistical computing. R Foundation for Statistical Computing. Vienna, Austria. Version 3.3.1. https://www.R-project.org.

Reynolds, D., F. Baret, C. Welcker, A. Bostrom, J. Ball, F. Cellini, et al. 2018. What is cost-efficient phenotyping? Optimizing costs for different scenarios. Plant Science 282: 14-22.

1974. Comparative performance for maize hybrids representing different eras of maize breeding. Proc. 29th Annu. Corn Sorghum Res. Conf.

Sankaran, S., L.R. Khot, C.Z. Espinoza, S. Jarolmasjed, V.R. Sathuvalli, G.J. Vandemark, et al. 2015. Low-altitude, high-resolution aerial imaging systems for row and field crop phenotyping: A review. European Journal of Agronomy 70: 112-123.

Schnable, J.C. and M. Freeling. 2011. Genes identified by visible mutant phenotypes show increased bias toward one of two subgenomes of maize. PloS One 6: e17855.

Schnable, P.S., D. Ware, R.S. Fulton, J.C. Stein, F. Wei, S. Pasternak, et al. 2009. The B73 maize genome: complexity, diversity, and dynamics. Science 326: 1112-1115.

Serifoglu Yilmaz, C. and O. Gungor. 2016. Comparison of the performances of ground filtering algorithms and DTM generation from a UAV-based point cloud. Geocarto International 33: 522-537.

Shi, Y., J.A. Thomasson, S.C. Murray, N.A. Pugh, W.L. Rooney, S. Shafian, et al. 2016. Unmanned aerial vehicles for high-throughput phenotyping and agronomic research. PloS One 11: e0159781.

Sithole, G. and G. Vosselman. 2004. Experimental comparison of filter algorithms for bare-earth extraction from airborne laser scanning point clouds. ISPRS Journal of Photogrammetry and Remote Sensing 59: 85-101.

Stinard, P. and D. Robertson. 1987. Dappled: A putative mu-induced aleurone developmental mutant. Maize Genet. Coop. Newsl 61: 7-9.

Sun, L. and R. Wu. 2015. Mapping complex traits as a dynamic system. Physics of Life Reviews 13: 155-185.

Tanger, P., S. Klassen, J.P. Mojica, J.T. Lovell, B.T. Moyers, M. Baraoidan, et al. 2017. Field-based high throughput phenotyping rapidly identifies genomic regions controlling yield components in rice. Scientific Reports 7: 42839.

Tilly, N., D. Hoffmeister, Q. Cao, S. Huang, V. Lenz-Wiedemann, Y. Miao, et al. 2014. Multitemporal crop surface models: accurate plant height measurement and biomass estimation with terrestrial laser scanning in paddy rice. Journal of Applied Remote Sensing 8: 083671-083671.

Tilly, N., D. Hoffmeister, H. Liang, Q. Cao, Y. Liu, V. Lenz-Wiedemann, et al. 2012. Evaluation of terrestrial laser scanning for rice growth monitoring. Int. Arch. Photogramm. Remote Sens. Spat. Inf. Sci 39: B7.

Tilman, D., C. Balzer, J. Hill and B.L. Befort. 2011. Global food demand and the sustainable intensification of agriculture. Proceedings of the National Academy of Sciences 108: 20260-20264.

Tilman, D., K.G. Cassman, P.A. Matson, R. Naylor and S. Polasky. 2002. Agricultural sustainability and intensive production practices. Nature 418: 671.

van der Voort, D. 2016. Exploring the Usability of Unmanned Aerial Vehicles for Non-Destructive Phenotyping of Small-Scale Maize Breeding Trials. Wageningen: Wageningen University and Research Centre.

Varela, S., Y. Assefa, P.V. Prasad, N.R. Peralta, T.W. Griffin, A. Sharda, et al. 2017. Spatio-temporal evaluation of plant height in corn via unmanned aerial systems. Journal of Applied Remote Sensing 11: 036013.

Verhulst, P.-F. 1838. Notice sur la loi que la population suit dans son accroissement. Corresp. Math. Phys. 10: 113-126.

Wallace, J.G., X. Zhang, Y. Beyene, K. Semagn, M. Olsen, B.M. Prasanna, et al. 2016. Genome-wide association for plant height and flowering time across 15 tropical maize populations under managed drought stress and well-watered conditions in Sub-Saharan Africa. Crop Science 56: 2365-2378.

Wallace, L., A. Lucieer, C. Watson and D. Turner. 2012. Development of a UAV-LiDAR system with application to forest inventory. Remote Sensing 4: 1519-1543.

Wang, X., R. Zhang, W. Song, L. Han, X. Liu, X. Sun, et al. 2019. Dynamic plant height QTL revealed in maize through remote sensing phenotyping using a high-throughput unmanned aerial vehicle (UAV). Scientific Reports 9: 3458.

Wang, Y., J. Zhao, W. Lu and D. Deng. 2017. Gibberellin in plant height control: old player, new story. Plant Cell Reports 36: 1-8.

Wardhani, W.S. and P. Kusumastuti. 2013. Describing the Height Growth of Corn using Logistic and Gompertz Model. Agrivita 35: 237.

Watanabe, K., W. Guo, K. Arai, H. Takanashi, H. Kajiya-Kanegae, M. Kobayashi, et al. 2017. High-throughput phenotyping of sorghum plant height using an unmanned

aerial vehicle and its application to genomic prediction modeling. Frontiers in Plant Science 8.

2002. Classification of LIDAR data using a lower envelope follower and gradient-based operator. Geoscience and Remote Sensing Symposium, 2002. IGARSS'02. 2002 IEEE International, IEEE.

Westoby, M., J. Brasington, N. Glasser, M. Hambrey and J. Reynolds. 2012. 'Structure-from-Motion'photogrammetry: A low-cost, effective tool for geoscience applications. Geomorphology 179: 300-314.

White, J.W., P. Andrade-Sanchez, M.A. Gore, K.F. Bronson, T.A. Coffelt, M.M. Conley, et al. 2012. Field-based phenomics for plant genetics research. Field Crops Research 133: 101-112.

Willkomm, M., A. Bolten and G. Bareth. 2016. Non-Destructive Monitoring of Rice by Hyperspectral In-Field Spectrometry and UAV-Based Remote Sensing: Case Study of Field-Grown Rice in North Rhine-Westphalia, Germany. International Archives of the Photogrammetry, Remote Sensing & Spatial Information Sciences 41.

Winkler, R.G. and T. Helentjaris. 1995. The maize Dwarf3 gene encodes a cytochrome P450-mediated early step in Gibberellin biosynthesis. The Plant Cell 7: 1307-1317.

Woodhouse, M.R., J.C. Schnable, B.S. Pedersen, E. Lyons, D. Lisch, S. Subramaniam, et al. 2010. Following tetraploidy in maize, a short deletion mechanism removed genes preferentially from one of the two homeologs. PLoS Biology 8: e1000409.

Wu, R. and M. Lin. 2006. Functional mapping—how to map and study the genetic architecture of dynamic complex traits. Nature Reviews Genetics 7: 229-237.

Wu, R. and M. Lin. 2006. Functional mapping—how to map and study the genetic architecture of dynamic complex traits. Nature Reviews Genetics 7: 229.

Wu, R., Z. Wang, W. Zhao and J.M. Cheverud. 2004. A mechanistic model for genetic machinery of ontogenetic growth. Genetics 168: 2383-2394.

Würschum, T., W. Liu, L. Busemeyer, M.R. Tucker, J.C. Reif, E.A. Weissmann, et al. 2014. Mapping dynamic QTL for plant height in triticale. BMC Genetics 15: 59.

Xavier, A., B. Hall, A.A. Hearst, K.A. Cherkauer and K.M. Rainey. 2017. Genetic Architecture of Phenomic-Enabled Canopy Coverage in Glycine max. Genetics 206: 1081-1089.

Xavier, A., B. Hall, A.A. Hearst, K.A. Cherkauer and K.M. Rainey. 2017. Genetic architecture of phenomic-enabled canopy coverage in Glycine max. Genetics 206: genetics. 116.198713.

Yang, G., J. Liu, C. Zhao, Z. Li, Y. Huang, H. Yu, et al. 2017. Unmanned aerial vehicle remote sensing for field-based crop phenotyping: Current status and perspectives. Frontiers in Plant Science 8: 1111.

Yin, X., M.A. McClure, N. Jaja, D.D. Tyler and R.M. Hayes. 2011. In-season prediction of corn yield using plant height under major production systems. Agronomy Journal 103: 923-929.

Zhang, W., J. Qi, P. Wan, H. Wang, D. Xie, X. Wang, et al. 2016. An easy-to-use airborne LiDAR data filtering method based on cloth simulation. Remote Sensing 8: 501.

Zhang, X., C. Huang, D. Wu, F. Qiao, W. Li, L. Duan, et al. 2017. High-throughput phenotyping and QTL mapping reveals the genetic architecture of maize plant growth. Plant Physiology 173: 1554-1564.

APPENDIX A

SUPPLEMENTAL TABLES

Appendix A1. Summary of 2017 UAS flight dates of G2F population, including: days after sowing (DAS), the number of images captured, spatial resolution of the mosaic image and dates in which manual phenotype measurements were collected for each trial (DG2F: Optimal planted, non-irrigated trial; G2FE: Optimal planted, irrigated trial; G2LA: Delay planted, irrigated trial).

								GCP Geolocation details			
Flight date	**UAS Platform†**	**DAS‡**	**Number Images§**	**Resolution (cm/pix)§**	**G2FE Manual Date**	**DG2F Manual Date**	**G2LA Manual Date**	**No. GCP**	**Mean RSME(X) (cm)**	**Mean RSME(Y) (cm)**	**Mean RSME(Z) (cm)**	**Mean RMSE (cm)**
DJI Phantom 3 Pro												
3/14/17	RW	11/-23	491	0.98	-	-	-	6	6.5	7.3	0.8	4.9
3/23/17	RW	20/-14	539	1.06	-	-	-	6	7.5	7.6	0.7	5.2
3/30/17	RW	27/-7	529	1.04	-	-	-	12	26.5	30.6	17.0	24.1
4/6/17	RW	34/0	487	1.01	-	-	-	9	33.6	30.9	6.9	23.7
4/13/17	RW	41/7	519	1.00	-	-	-	12	43.2	38.1	18.4	33.2
4/20/17	RW	48/14	550	1.06	4/24/17	4/24/17	-	12	40.2	35.9	20.0	32.0
4/27/17	RW	55/21	548	1.01	4/28/17	-	-	7	10.6	8.0	2.3	7.0
5/1/17	RW	59/25	514	1.05	5/1/17	5/1/17	-	8	11.3	12.9	7.0	10.4
5/5/17	RW	63/29	485	1.04	5/5/17	5/5/17	-	7	14.0	10.3	7.0	10.4
5/9/17	RW	67/33	499	1.05	5/9/17	5/9/17	5/9/17	12	5.0	5.4	1.7	4.0
5/11/17	RW	69/35	523	1.06	5/11/17	5/11/17	-	12	38.0	32.6	13.9	28.1
5/19/17	RW	77/43	556	1.08	5/16/17	5/16/17	5/19/17	12	10.7	9.5	3.7	7.9
5/24/17	RW	82/48	562	1.05	-	-	5/24/17	12	12.1	9.3	3.6	8.3
5/30/17	RW	88/54	501	1.10	-	-	5/30/17	12	11.6	9.5	3.5	8.1
6/2/17	RW	91/57	519	1.06	-	-	6/2/17	12	3.9	4.5	0.9	3.1
6/5/17	RW	94/60	568	1.04	-	-	6/5/17	12	11.2	10.2	2.8	8.1
6/8/17	RW	97/63	535	1.05	6/8/17	6/8/17	6/8/17	12	8.2	9.2	2.9	6.7

Appendix A1. Continued.

Flight date	UAS Platform†	DAS‡	Number Images§	Resolution (cm/pix)§	G2FE Manual Date	DG2F Manual Date	G2LA Manual Date	GCP Geolocation details				
								No. GCP	Mean RSME(X) (cm)	Mean RSME(Y) (cm)	Mean RSME(Z) (cm)	Mean RMSE (cm)
6/16/17	RW	105/71	770	1.08	-	-	-	12	5.1	6.0	1.7	4.2
6/29/17	RW	118/84	501	1.08	-		-	12	0.8	2.0	0.2	1.0
7/14/17	RW	133/99	456	1.06	-	-	-	12	7.3	7.2	4.6	11.2
7/27/17	RW	146/112	484	1.07	-	-	-	10	7.1	11.9	5.0	8.0
Tuffwing UAV Mapper												
3/8/17	FW	5/-29	374	1.95	-	-	-	16	4.2	5.2	2.2	3.9
3/21/17	FW	18/-16	163	2.79	-	-	-	16	3.0	4.2	1.4	2.9
4/7/17	FW	35/1	247	2.67				16	1.8	3.6	2.4	2.6
4/20/17	FW	48/14	137	2.76	4/24/17	4/24/17	-	12	2.1	1.6	1.1	1.6
5/2/17	FW	60/26	199	2.67	-	-	-	16	2.1	1.6	1.4	1.7
5/5/17	FW	63/29	199	2.67	5/5/17	5/5/17	-	16	2.1	1.6	1.4	1.7
5/9/17	FW	67/33	144	2.74	5/9/17	5/9/17	5/9/17	10	2.3	2.0	1.0	1.8
5/12/17	FW	70/36	210	2.83	-	-	-	16	2.0	1.5	1.1	1.5
5/15/17	FW	73/39	204	2.73	-	-	-	16	2.2	1.9	1.4	1.8
5/24/17	FW	82/48	231	2.76	-	-	5/24/17	16	2.5	1.7	1.9	2.0
5/30/17	FW	88/54	242	2.73	-	-	5/30/17	16	2.2	2.1	1.0	1.8
6/2/17	FW	91/57	235	2.75	-	-	6/2/17	16	2.3	2.4	1.1	1.9
6/6/17	FW	95/61	235	2.75	-	-	-	16	2.5	2.2	1.8	2.2
6/9/17	FW	98/64	233	2.80	-	-	-	16	2.2	2.3	1.0	1.8
6/12/17	FW	101/67	235	2.76	-	-	-	16	2.6	1.8	2.2	2.2
6/16/17	FW	105/71	242	2.74	-	-	-	16	2.3	2.0	1.8	2.0
6/23/17	FW	112/78	234	2.76	-	-	-	16	2.4	2.4	1.9	2.2
6/29/17	FW	118/84	233	2.71	-		-	16	1.8	3.1	2.2	2.4
7/13/17	FW	132/98	235	2.72	-	-	-	12	1.9	1.9	2.1	2.0
7/25/17	FW	144/110	240	2.72	-	-	-	14	1.9	2.6	1.2	1.9

† FW: Fixed wing; RW: Rotary wing.

‡ DAS: Days after sowing; Number on left refers to early plantings (G2FE and DG2F) and right refers to late planting (G2LA).

§ Number on left refers to FW and right refers RW if flights occurred on the same date.

Appendix A2. Summary of UAS P95 height estimates summarized as the mean of the plot-based estimates across UAS platforms and experimental trials (DG2F: optimal planted, non-irrigated trial; G2FE: optimal planted, irrigated trial; G2LA: delay planted, irrigated trial).

Fixed wing				Rotary wing			
DAS†‡	**G2FE**	**DG2F**	**G2LA**	**DAS†‡**	**G2FE**	**DG2F**	**G2LA**
-- (36)	**-**	**-**	**0.31**	**34 (35)**	**0.33**	**0.33**	**0.50**
-- (39)	**-**	**-**	**0.53**	**41 (43)**	**0.62**	**0.66**	**0.98**
48 (48)	**0.87**	**0.98**	**1.09**	**48 (48)**	**1.03**	**1.13**	**1.42**
-- (54)	**-**	**-**	**1.50**	**55 (54)**	**1.49**	**1.51**	**1.66**
60 (61)	**1.39**	**1.49**	**1.98**	**-- (60)**	**-**	**-**	**2.16**
63	**1.46**	**1.56**	**--**	**63**	**1.79**	**1.81**	**--**
67	**1.69**	**1.78**	**--**	**--**	**--**	**--**	**--**
$\frac{\sum \Delta_{\mu_{P95}}}{n}$ §	**0.27**	**0.27**	**0.42**	$\frac{\sum \Delta_{\mu_{P95}}}{n}$ §	**0.37**	**0.37**	**0.41**
$\frac{\sum \Delta_{\mu_{P95}}/\Delta_{DAS}}{n}$ ¶	**0.04**	**0.06**	**0.07**	$\frac{\sum \Delta_{\mu_{P95}}/\Delta_{DAS}}{n}$ ¶	**0.05**	**0.05**	**0.07**

† DAS; Days after sowing.

‡ Numbers in parenthesis indicate DAS for the delayed planting, G2LA.

§ Average of change in mean P95 across DAS during the exponential growth phase.

¶ Average per day rate of growth during the exponential growth phase.

Appendix A3. Summary statistics of logistic function fit to plot level temporal UAS P95 data across UAS platforms (fixed wing and rotary wing) and trials (DG2F: Optimal planted, non-irrigated trial; G2FE: Optimal planted, irrigated trial; G2LA: Delay planted, irrigated trial).

	Fixed wing			**Rotary wing**		
	G2FE	**DG2F**	**G2LA**	**G2FE**	**DG2F**	**G2LA**
N	**589**	**499**	**500**	**594**	**500**	**495**
Mean RMSE (m)	**0.061**	**0.061**	**0.101**	**0.095**	**0.086**	**0.131**
Std. Dev. RMSE (m)	**0.014**	**0.017**	**0.032**	**0.030**	**0.035**	**0.053**
Mean R^2	**0.991**	**0.991**	**0.989**	**0.987**	**0.989**	**0.981**
Std. Dev. R^2	**0.004**	**0.004**	**0.006**	**0.007**	**0.010**	**0.015**

Appendix A4. Table presents the best model identified for predicting yield using four sets of input predictor variables: (i) manual terminal plant height (PHT), (ii) logistic function parameters (3PLogistic), (iii) pedigree BLUPs by flight date (UAS heights), and (iv) a combination of logistic function parameter and pedigree BLUPs by flight date (UAS+3P). Models were fit by platform and by G2F trial.

Trial†	Platform§	Model	RMSE (t/ha)	R^2	df	Stepwise direction‡	Model term	Estimate	Std error	t Ratio	Prob>|t|	VIF¶
Optimal Planting Non-irrigated Trial (DG2F)												
DG2F	Manual	PHT	1.04	0.08	2	NA	Intercept	-42.17	48.24	-0.87	0.38	.
DG2F	Manual	PHT	1.04	0.08	2	NA	Pht	88.95	19.97	4.45	<.0001	1.00
DG2F	FW	3PLogistic	0.92	0.34	3	F/B	Intercept	-316.20	49.73	-6.36	<.0001	.
DG2F	FW	3PLogistic	0.92	0.34	3	F/B	Asymptote	77.90	15.58	5.00	<.0001	1.27
DG2F	FW	3PLogistic	0.92	0.34	3	F/B	Inflection point	7.30	1.18	6.18	<.0001	1.27
DG2F	FW	UAS heights	0.92	0.38	3	F/B	Intercept	56.22	26.16	2.15	0.03	.
DG2F	FW	UAS heights	0.92	0.38	3	F/B	2017-04-20	-133.16	19.42	-6.86	<.0001	1.05
DG2F	FW	UAS heights	0.92	0.38	3	F/B	2017-06-23	136.08	12.55	10.84	<.0001	1.05
DG2F	FW	UAS+3P	0.92	0.35	3	F	Intercept	-315.25	49.40	-6.38	<.0001	.
DG2F	FW	UAS+3P	0.92	0.35	3	F	Inflection point	7.50	1.14	6.55	<.0001	1.21
DG2F	FW	UAS+3P	0.92	0.35	3	F	2017-06-23	73.08	13.75	5.32	<.0001	1.21
DG2F	FW	UAS+3P	0.92	0.37	3	B	Intercept	56.22	26.16	2.15	0.03	.
DG2F	FW	UAS+3P	0.92	0.37	3	B	2017-04-20	-133.16	19.42	-6.86	<.0001	1.05
DG2F	FW	UAS+3P	0.92	0.37	3	B	2017-06-23	136.08	12.55	10.84	<.0001	1.05
DG2F	RW	3PLogistic	0.92	0.33	3	F	Intercept	-527.87	65.97	-8.00	<.0001	.
DG2F	RW	3PLogistic	0.92	0.33	3	F	Asymptote	158.06	27.28	5.79	<.0001	1.23
DG2F	RW	3PLogistic	0.92	0.33	3	F	Inflection point	7.97	1.43	5.59	<.0001	1.23
DG2F	RW	UAS heights	0.92	0.35	4	F	Intercept	-557.21	140.61	-3.96	<.0001	.
DG2F	RW	UAS heights	0.92	0.35	4	F	2017-04-27	-97.99	18.15	-5.40	<.0001	1.06

Appendix A4. Continued.

Trial†	Platform§	Model	RMSE (t/ha)	R^2	df	Stepwise direction‡	Model term	Estimate	Std error	t Ratio	Prob>|t|	VIF¶
DG2F	RW	UAS heights	0.92	0.35	4	F	2017-06-29	260.07	54.33	4.79	<.0001	1.03
DG2F	RW	UAS heights	0.92	0.35	4	F	2017-07-14	124.66	15.44	8.08	<.0001	1.07
DG2F	RW	UAS heights	0.92	0.35	4	B	Intercept	-557.21	140.61	-3.96	<.0001	.
DG2F	RW	UAS heights	0.92	0.35	4	B	2017-04-27	-97.99	18.15	-5.40	<.0001	1.06
DG2F	RW	UAS heights	0.92	0.35	4	B	2017-06-29	260.07	54.33	4.79	<.0001	1.03
DG2F	RW	UAS heights	0.92	0.35	4	B	2017-07-14	124.66	15.44	8.08	<.0001	1.07
DG2F	RW	UAS+3P	0.92	0.37	5	F	Intercept	-462.72	139.74	-3.31	0	.
DG2F	RW	UAS+3P	0.92	0.37	5	F	Asymptote	199.26	26.79	7.44	<.0001	1.25
DG2F	RW	UAS+3P	0.92	0.37	5	F	2017-04-06	-212.14	85.52	-2.48	0.01	1.55
DG2F	RW	UAS+3P	0.92	0.37	5	F	2017-04-20	-70.26	23.85	-2.95	0	1.58
DG2F	RW	UAS+3P	0.92	0.37	5	F	2017-06-29	146.52	57.24	2.56	0.01	1.19
DG2F	RW	UAS+3P	0.92	0.35	4	B	Intercept	-557.21	140.61	-3.96	<.0001	.
DG2F	RW	UAS+3P	0.92	0.35	4	B	2017-04-27	-97.99	18.15	-5.40	<.0001	1.06
DG2F	RW	UAS+3P	0.92	0.35	4	B	2017-06-29	260.07	54.33	4.79	<.0001	1.03
DG2F	RW	UAS+3P	0.92	0.35	4	B	2017-07-14	124.66	15.44	8.08	<.0001	1.07
Optimal planting irrigated trial (g2fe)												
G2FE	Manual	PHT	1.04	0.06	2	NA	Intercept	9.36	40.03	0.23	0.82	.
G2FE	Manual	PHT	1.04	0.06	2	NA	Pht	69.95	16.65	4.20	<.0001	1.00
G2FE	FW	3PLogistic	0.98	0.26	3	F/B	Intercept	-180.13	41.81	-4.31	<.0001	.
G2FE	FW	3PLogistic	0.98	0.26	3	F/B	Asymptote	63.56	13.53	4.70	<.0001	1.32
G2FE	FW	3PLogistic	0.98	0.26	3	F/B	Inflection point	5.11	0.99	5.15	<.0001	1.32
G2FE	FW	UAS heights	0.98	0.35	4	F	Intercept	68.67	22.49	3.05	0	.
G2FE	FW	UAS heights	0.98	0.35	4	F	2017-04-20	-121.03	18.10	-6.69	<.0001	1.03
G2FE	FW	UAS heights	0.98	0.35	4	F	2017-06-29	125.00	`11.21	11.15	<.0001	1.03

Appendix A4. Continued.

Trial†	Platform§	Model	RMSE (t/ha)	R^2	df	Stepwise direction‡	Model term	Estimate	Std error	t Ratio	Prob>|t|	VIF¶
G2FE	FW	UAS heights	0.98	0.37	4	B	Intercept	62.94	22.43	2.81	0.01	.
G2FE	FW	UAS heights	0.98	0.37	4	B	2017-04-20	-123.45	17.97	-6.87	<.0001	1.04
G2FE	FW	UAS heights	0.98	0.37	4	B	2017-06-06	49.20	20.40	2.41	0.02	4.11
G2FE	FW	UAS heights	0.98	0.37	4	B	2017-06-29	78.79	22.15	3.56	0	4.10
G2FE	FW	UAS+3P	0.92	0.28	3	F	Intercept	-196.97	41.54	-4.74	<.0001	.
G2FE	FW	UAS+3P	0.92	0.28	3	F	Inflection point	5.42	0.93	5.81	<.0001	1.20
G2FE	FW	UAS+3P	0.92	0.28	3	F	2017-06-29	65.42	12.52	5.23	<.0001	1.20
G2FE	FW	UAS+3P	0.98	0.35	3	B	Intercept	68.67	22.49	3.05	0	.
G2FE	FW	UAS+3P	0.98	0.35	3	B	2017-04-20	-121.03	18.10	-6.69	<.0001	1.03
G2FE	FW	UAS+3P	0.98	0.35	3	B	2017-06-29	125.00	11.21	11.15	<.0001	1.03
G2FE	RW	3PLogistic	0.98	0.32	4	F/B	Intercept	-812.08	115.15	-7.05	<.0001	.
G2FE	RW	3PLogistic	0.98	0.32	4	F/B	Asymptote	172.58	26.64	6.48	<.0001	1.19
G2FE	RW	3PLogistic	0.98	0.32	4	F/B	Growth rate	782.06	357.40	2.19	0.03	1.39
G2FE	RW	3PLogistic	0.98	0.32	4	F/B	Inflection point	11.28	1.65	6.84	<.0001	1.41
G2FE	RW	UAS heights	0.98	0.30	4	F	Intercept	-63.54	42.24	-1.50	0.13	.
G2FE	RW	UAS heights	0.98	0.30	4	F	2017-04-13	-179.70	27.32	-6.58	<.0001	1.03
G2FE	RW	UAS heights	0.98	0.30	4	F	2017-05-19	104.70	23.42	4.47	<.0001	2.09
G2FE	RW	UAS heights	0.98	0.30	4	F	2017-06-16	72.73	27.28	2.67	0.01	2.05
G2FE	RW	UAS heights	0.98	0.33	5	B	Intercept	-327.01	96.76	-3.38	0	.
G2FE	RW	UAS heights	0.98	0.33	5	B	2017-04-20	-170.62	22.05	-7.74	<.0001	1.51
G2FE	RW	UAS heights	0.98	0.33	5	B	2017-05-11	113.22	24.17	4.68	<.0001	2.25
G2FE	RW	UAS heights	0.98	0.33	5	B	2017-06-16	67.33	25.77	2.61	0.01	1.90
G2FE	RW	UAS heights	0.98	0.33	5	B	2017-06-29	143.51	46.64	3.08	0	1.39
G2FE	RW	UAS+3P	0.98	0.33	3	F	Intercept	-703.50	75.46	-9.32	<.0001	.

Appendix A4. Continued.

Trial†	Platform§	Model	RMSE (t/ha)	R^2	df	Stepwise direction‡	Model term	Estimate	Std error	t Ratio	Prob>|t|	VIF¶
G2FE	RW	UAS+3P	0.98	0.33	3	F	Inflection point	14.48	1.39	10.40	<.0001	1.02
G2FE	RW	UAS+3P	0.98	0.33	3	F	2017-05-11	112.89	16.26	6.94	<.0001	1.02
G2FE	RW	UAS+3P	0.98	0.31	3	B	Intercept	-176.60	53.24	-3.32	0	.
G2FE	RW	UAS+3P	0.98	0.31	3	B	Asymptote	231.90	24.68	9.40	<.0001	1.00
G2FE	RW	UAS+3P	0.98	0.31	3	B	2017-04-06	-373.48	58.91	-6.34	<.0001	1.00
Delayed planting irrigated trial (g2la)												
G2LA	Manual	PHT	0.67	0.07		NA	Intercept	5.35	22.08	0.24	0.81	.
G2LA	Manual	PHT	0.67	0.07		NA	Pht	36.87	8.87	4.16	<.0001	1.00
G2LA	FW	3PLogistic	0.61	0.27	4	F/B	Intercept	289.38	59.12	4.90	<.0001	.
G2LA	FW	3PLogistic	0.61	0.27	4	F/B	Asymptote	54.90	8.13	6.76	<.0001	2.13
G2LA	FW	3PLogistic	0.61	0.27	4	F/B	Growth rate	-407.42	99.21	-4.11	<.0001	2.46
G2LA	FW	3PLogistic	0.61	0.27	4	F/B	Inflection point	-4.86	1.11	-4.39	<.0001	3.41
G2LA	FW	UAS heights	0.61	0.28	3	F	Intercept	9.12	9.89	0.92	0.36	.
G2LA	FW	UAS heights	0.61	0.28	3	F	2017-05-15	68.17	13.45	5.07	<.0001	1.02
G2LA	FW	UAS heights	0.61	0.28	3	F	2017-07-25	34.20	3.98	8.60	<.0001	1.02
G2LA	FW	UAS heights	0.61	0.28	3	B	Intercept	9.12	9.89	0.92	0.36	.
G2LA	FW	UAS heights	0.61	0.28	3	B	2017-05-15	68.17	13.45	5.07	<.0001	1.02
G2LA	FW	UAS heights	0.61	0.28	3	B	2017-07-25	34.20	3.98	8.60	<.0001	1.02
G2LA	FW	UAS+3P	0.61	0.28	3	F	Intercept	9.12	9.89	0.92	0.36	.
G2LA	FW	UAS+3P	0.61	0.28	3	F	2017-05-15	68.17	13.45	5.07	<.0001	1.02
G2LA	FW	UAS+3P	0.61	0.28	3	F	2017-07-25	34.20	3.98	8.60	<.0001	1.02
G2LA	FW	UAS+3P	0.61	0.27	10	B	Intercept	85.09	16.40	5.19	<.0001	.
G2LA	FW	UAS+3P	0.61	0.27	10	B	Growth rate	-503.01	65.13	-7.72	<.0001	1.08
G2LA	FW	UAS+3P	0.61	0.27	10	B	2017-05-30	69.83	9.93	7.03	<.0001	1.08

Appendix A4. Continued.

Trial†	Platform§	Model	RMSE (t/ha)	R^2	df	Stepwise direction‡	Model term	Estimate	Std error	t Ratio	Prob>|t|	VIF¶
G2LA	FW	3PLogistic	0.61	0.25	4	F/B	Intercept	166.16	75.38	2.20	0.03	.
G2LA	FW	3PLogistic	0.61	0.25	4	F/B	Asymptote	81.07	10.07	8.05	<.0001	1.64
G2LA	FW	3PLogistic	0.61	0.25	4	F/B	Growth rate	-483.70	192.21	-2.52	0.01	2.52
G2LA	FW	3PLogistic	0.61	0.25	4	F/B	Inflection point	-4.17	1.46	-2.86	0	3.49
G2LA	FW	UAS heights	0.61	0.26	3	F	Intercept	-48.64	20.53	-2.37	0.02	.
G2LA	FW	UAS heights	0.61	0.26	3	F	2017-05-09	128.05	37.60	3.41	0	1.00
G2LA	FW	UAS heights	0.61	0.26	3	F	2017-07-14	45.90	5.41	8.48	<.0001	1.00
G2LA	FW	UAS heights	0.61	0.26	3	B	Intercept	-48.64	20.53	-2.37	0.02	.
G2LA	FW	UAS heights	0.61	0.26	3	B	2017-05-09	128.05	37.60	3.41	0	1.00
G2LA	FW	UAS heights	0.61	0.26	3	B	2017-07-14	45.90	5.41	8.48	<.0001	1.00
G2LA	FW	UAS+3P	0.61	0.26	3	F	Intercept	-48.64	20.53	-2.37	0.02	.
G2LA	FW	UAS+3P	0.61	0.26	3	F	2017-05-09	128.05	37.60	3.41	0	1.00
G2LA	FW	UAS+3P	0.61	0.26	3	F	2017-07-14	45.90	5.41	8.48	<.0001	1.00
G2LA	FW	UAS+3P	0.61	0.26	2	B	Intercept	-100.51	24.50	-4.10	<.0001	.
G2LA	FW	UAS+3P	0.61	0.26	2	B	Asymptote	64.98	7.82	8.31	<.0001	1.00
G2LA	FW	UAS+3P	0.61	0.26	2	B	2017-05-09	117.53	37.78	3.11	0	1.00

† Manual: Manually collected terminal plant height; FW: fixed wing; RW: rotary wing.
§ DG2F: Optimal planted, non-irrigated trial; G2FE: Optimal planted, irrigated trial; G2LA: Delay planted, irrigated trial.
‡ B: Backwards regression; F: Forward regression; F/B: mode was consistent across forward and backward regression.
¶ VIF: Variance inflation factor.

Appendix A5. Selection accuracy of hybrid grain perform based on relative ranks utilizing manual terminal plant height (PHT_{TRML}), fixed wing logistic parameters (FW), or rotary wing logistic parameters (RW) across the G2F trials.

	DG2F			G2FE			G2LA			Combined trials		
	PHT_{TRML} †	**FW‡**	**RW§**	**PHT_{TRML} †**	**FW‡**	**RW§**	**PHT_{TRML} †**	**FW‡**	**RW§**	**PHT_{TRML} †**	**FW‡**	**RW§**
MAE[#] in relative ranking¶	**63**	**55**	**53**	**78**	**66**	**67**	**59**	**52**	**52**	**33**	**57**	**26**
Selection accuracy	**0.21**	**0.50**	**0.54**	**0.21**	**0.36**	**0.36**	**0.21**	**0.32**	**0.36**	**0.25**	**0.32**	**0.36**

† PHT: Selection accuracy using manual plant height as predictor.
‡ FW: Selection accuracy using logistic parameters of high altitude fixed wing as the predictors.
§ RW: Selection accuracy using logistic parameters of low altitude rotary wing as the predictors.
¶ The average of the absolute difference between grain yield rank and the predicted grain yield by prediction model (PHT, FW, RC).
# MAE: Mean absolute error.

Appendix A6. Summary of 2018 UAS flight dates of the fields containing the Tx740xNC356, Ki3xNC356, and LH82xLAMA populations, including: days after sowing (DAS), the number of images captured, the number of calibrated images, spatial resolution of the mosaic image and mean errors of the GCP geo-referencing.

						GCP Geolocation details				
Flight date	**UAS Platform†**	**DAS‡**	**Number Images**	**Calibrated Images**	**Resolution (cm/pix)**	**No. GCP**	**Mean RSME(X) (m)**	**Mean RSME(Y) (m)**	**Mean RSME(Z) (m)**	**Mean RMSE (m)**
3/14/18	RW	0	822	822	1.12	8	0.24	0.25	0.03	0.17
3/30/18	RW	16	505	505	1.04	8	0.13	0.12	0.01	0.08
4/08/18	RW	25	473	473	1.02	8	6.17	2.12	0.08	2.60
4/11/18	RW	28	555	555	1.05	8	0.13	0.11	0.01	0.08
4/18/18	RW	35	539	539	1.13	8	0.16	0.15	0.02	0.11
4/26/18	RW	43	520	518	1.03	7	0.09	0.09	0.01	0.06
5/10/18	RW	57	513	513	1.07	30	0.05	0.05	0.05	0.05
5/15/18	RW	62	535	513	1.10	26	5.48	9.41	0.06	4.98
5/18/18	RW	65	515	485	1.06	25	0.05	0.06	0.03	0.04
5/22/18	RW	69	786	786	0.62	28	0.03	0.03	0.01	0.02
5/25/18	RW	72	1484	1315	0.65	30	0.03	0.04	0.03	0.03
5/29/18	RW	76	512	463	1.06	26	0.78	0.91	1.11	0.78
6/01/18	RW	79	521	448	1.04	8	0.01	0.01	<0.01	<0.01
6/05/18	RW	83	-	-	-	-	-	-	-	-
6/07/18	RW	85	-	-	-	-	-	-	-	-
6/13/18	RW	91	513	289	1.04	10	<0.01	<0.01	<0.01	<0.01
6/22/18	RW	100	492	303	1.08	22	0.03	0.02	0.03	0.03
7/03/18	RW	111	290	232	1.10	17	0.19	0.20	0.03	0.14
7/20/18	RW	128	-	-	-	-	-	-	-	-

Appendix A6. Continued.

						GCP Geolocation details				
Flight date	**UAS Platform†**	**DAS‡**	**Number Images**	**Calibrated Images**	**Resolution (cm/pix)**	**No. GCP**	**Mean RSME(X) (m)**	**Mean RSME(Y) (m)**	**Mean RSME(Z) (m)**	**Mean RMSE (m)**
Tuffwing UAV Mapper										
5/17/18	FW	64	67	67	2.70	39	0.02	0.04	0.01	0.04
5/21/18	FW	68	66	66	2.68	39	0.02	0.04	0.01	0.04
5/24/18	FW	71	65	65	2.59	10	0.01	0.01	<0.01	0.01
6/05/18	FW	83	61	61	2.75	10	0.05	0.06	<0.01	0.08
6/08/18	FW	86	66	66	2.71	10	0.06	0.06	<0.01	0.08
6/14/18	FW	92	56	56	2.79	10	0.05	0.05	<0.01	0.07
6/18/18	FW	96	66	66	2.72	10	0.01	0.02	<0.01	0.03
6/22/18	FW	100	68	68	2.72	10	0.05	0.06	<0.01	0.08
7/09/18	FW	117	67	67	2.77	10	0.01	0.01	0.01	0.02
7/16/18	FW	124	-	-	-	-	-	-	-	-
7/25/18	FW	133	-	-	-	-	-	-	-	-

† FW: Fixed wing; RW: Rotary wing.

‡ DAS: Days after sowing.

Appendix A7. Summary of significant QTL for flowering time.

Population	Trt†	Trait‡	Chr§	Position (cM)	Left Marker	Right Marker	LOD¶	PVE#	Add†† (d)	Left CI‡‡ (bp)	Right CI‡‡ (bp)
Ki3xNC356	I	DTA	2	24	AgR_02478	AgR_04085	6.77	5.08	0.63	10603658	11134513
Ki3xNC356	I	DTA	2	30	AgR_00649	AgR_00650	15.01	12.09	-0.98	13342033	13342154
Ki3xNC356	D	DTA	2	34	AgR_14537	AgR_10838	2.09	4.05	-0.42	15125786	15246819
Ki3xNC356	I	DTS	2	35	AgR_02349	AgR_14540	5.58	10.68	-0.76	15580072	15979202
Ki3xNC356	D	DTS	6	24	AgR_05809	AgR_16068	2.02	4.10	-0.49	89403767	89687544
Ki3xNC356	I	DTS	6	87	AgR_07216	AgR_05955	2.17	3.98	0.46	162645223	163665243
Ki3xNC356	D	DTA	9	60	AgR_01594	AgR_16910	2.07	4.03	0.42	133886762	133897924
LH82xLAMA	I	DTS	1	129	AgR_03912	AgR_01056	2.03	3.91	-0.49	223165736	224078702
LH82xLAMA	D	DTA	1	168	AgR_00790	AgR_00109	4.46	10.11	-0.62	275833355	277585472
LH82xLAMA	I	DTA	1	169	AgR_10766	AgR_10769	7.42	15.25	-0.73	278195980	278603093
LH82xLAMA	D	DTS	1	181	AgR_00413	AgR_00912	3.75	7.01	-0.56	287290866	287291452
LH82xLAMA	I	DTS	1	182	AgR_17266	AgR_07760	5.43	11.64	-0.84	287335033	287586834
LH82xLAMA	D	DTS	2	28	AgR_00736	AgR_10834	3.94	7.22	-0.57	11299939	11946310
LH82xLAMA	I	DTA	3	68	AgR_15093	AgR_02600	2.69	5.22	0.43	154076377	154660873
LH82xLAMA	D	DTS	3	68	AgR_15093	AgR_02600	2.52	4.53	0.46	154076377	154660873
LH82xLAMA	I	DTS	8	62	AgR_09615	AgR_13174	6.11	13.27	-0.90	120610321	122427978
LH82xLAMA	D	DTS	8	62	AgR_09615	AgR_13174	8.58	16.71	-0.87	120610321	122427978
LH82xLAMA	I	DTA	9	36	AgR_06613	AgR_06616	2.69	5.23	-0.44	15307137	15409063
LH82xLAMA	D	DTA	9	74	AgR_06777	AgR_01799	3.11	6.93	-0.52	110916495	130918887
LH82xLAMA	I	DTS	9	103	AgR_13529	AgR_16949	3.78	7.94	-0.70	149276973	149426980
LH82xLAMA	I	DTA	9	104	AgR_16951	AgR_09895	2.70	5.24	-0.43	149747320	149897954
LH82xLAMA	D	DTS	9	106	AgR_09895	AgR_09897	3.99	7.26	-0.57	149897954	149971831
Tx740xNC356	I	DTA	8	60	AgR_09612	AgR_06423	2.07	9.45	0.55	117761454	118224127

Appendix A7. Continued.

Population	Trt†	Trait‡	Chr§	Position (cM)	Left Marker	Right Marker	LOD¶	PVE#	Add†† (d)	Left CI‡‡ (bp)	Right CI‡‡ (bp)
Tx740xNC356	D	DTS	10	85	AgR_07121	AgR_13974	2.28	11.23	-0.65	144462556	145465473
Tx740xNC356	I	DTS	10	89	AgR_13777	AgR_17166	2.94	14.03	-0.72	145795322	145934793

† Trt: Treatment; I: Irrigated; D: Non-Irrigated.
‡ DTADays to anthesis; DTS: Days to silking.
§ Chr: Chromosome.
¶ LOD: $-\log_{10}$(p-value).
# PVE: Percent variation explained.
†† Additive effect estimate.
‡‡ CI: Confidence interval.

Appendix A8. Summary of significant QTL for functional parameters of the Weibull sigmoid function.

Population	Trt†	Trait‡	Chr§	Position (cM)	LOD¶	PVE#	Add††	Left marker (bp)	Right marker (bp)	Closest candidate gene	Gene function	Distance from gene (bp)
Ki3xNC356	I	Asym	2	59	2.46	4.45	-0.02	48405262	48664915	GRMZM2G017187	auxin response factor 1; auxin response factor 9, putative, expressed	1026060
Ki3xNC356	D	IP	3	94	3.57	6.27	0.36	212692256	212698619	GRMZM2G126260	Auxin efflux carrier family protein; auxin efflux carrier component, putative, expressed	2206613
Ki3xNC356	I	Asym	4	61	4.92	9.23	0.03	156384593	156517564	GRMZM2G134023	brassinosteroid-responsive RING-H2; zinc finger, C3HC4 type domain containing protein, expressed	259336.5
Ki3xNC356	I	IP	4	61	2.21	4.28	0.22	156384593	156517564	GRMZM2G134023	brassinosteroid-responsive RING-H2; zinc finger, C3HC4 type domain containing protein, expressed	259336.5
Ki3xNC356	I	IP	4	119	2.66	5.39	0.25	237391404	237610499	AC196708.3_FG006	SAUR-like auxin-responsive protein family ; OsSAUR5 - Auxin-responsive SAUR gene family member, expressed	187124.5
Ki3xNC356	D	IP	4	119	3.12	5.41	0.33	237391404	237610499	AC196708.3_FG006	SAUR-like auxin-responsive protein family ; OsSAUR5 - Auxin-responsive SAUR gene family member, expressed	187124.5
Ki3xNC356	I	Asym	5	38	2.28	3.93	0.02	21893133	21893252	GRMZM2G113135	SAUR-like auxin-responsive protein family ; CPuORF40 - conserved peptide uORF-containing transcript, expressed	1105270
Ki3xNC356	D	Asym	7	27	13.04	7.35	0.04	25781951	26153406	GRMZM2G075715	auxin response factor 6; auxin response factor, putative, expressed	13766771
Ki3xNC356	D	Asym	7	32	21.45	13.37	-0.05	95447274	96847624	GRMZM2G391795	alpha/beta-Hydrolases superfamily protein; gibberellin receptor GID1L2, putative, expressed	11778171
Ki3xNC356	D	IP	8	19	2.65	4.63	-0.30	8731594	9875920	GRMZM2G000489	alpha/beta-Hydrolases superfamily protein; gibberellin receptor GID1L2, putative, expressed	5630336
Ki3xNC356	D	IP	10	41	3.37	5.90	-0.34	84071836	86777777	GRMZM2G072632	Auxin efflux carrier family protein; auxin efflux carrier component, putative, expressed	4860010
LH82xLAMA	I	GR	1	135	4.03	7.36	-0.27	229187847	229850714	GRMZM2G153233	auxin response factor 16; auxin response factor 18, putative, expressed	1200114

Appendix A8. Continued.

Population	Trt†	Trait‡	Chr§	Position (cM)	LOD¶	PVE#	Add††	Left marker (bp)	Right marker (bp)	Closest candidate gene	Gene function	Distance from gene (bp)
LH82xLAMA	D	IP	1	145	3.23	7.65	-0.39	251713072	252736144	GRMZM2G341460	2-oxoglutarate (2OG) and Fe(II)-dependent oxygenase superfamily protein; gibberellin 20 oxidase 2, putative, expressed	2399240
LH82xLAMA	I	Asym	1	173	2.04	5.35	-0.02	280634097	281590394	vp8	viviparous8; small plant	5211076
LH82xLAMA	I	IP	1	176	4.31	11.58	-0.41	283600596	284011134	vp8	viviparous8; small plant	2517456
LH82xLAMA	I	GR	2	117	4.78	8.77	0.29	212246084	212544633	GRMZM2G064941	Auxin efflux carrier family protein; auxin efflux carrier component, putative, expressed	254540.5
LH82xLAMA	I	GR	3	62	3.62	6.56	0.25	140845175	142249525	GRMZM2G116204	endoplasmic reticulum auxin binding protein 1; auxin-binding protein 4 precursor, putative, expressed	7656087
LH82xLAMA	I	IP	3	67	2.66	6.98	0.32	151971786	154075136	GRMZM2G338259	auxin response factor 2; auxin response factor, putative, expressed	3461005
LH82xLAMA	D	IP	3	69	3.12	7.78	0.39	154668842	155959968	GRMZM2G338259	auxin response factor 2; auxin response factor, putative, expressed	1170061
LH82xLAMA	D	Asym	3	72	2.08	3.37	0.02	158668137	159817878	sdw2	short plant	830009.5
LH82xLAMA	D	Asym	3	96	2.14	3.42	0.02	176562816	177536662	na1	dwarf plant	1942864
LH82xLAMA	I	GR	5	28	3.55	6.41	0.25	7996372	8175228	GRMZM2G130675	SAUR-like auxin-responsive protein family ; OsSAUR1 - Auxin-responsive SAUR gene family member, expressed	2835967
LH82xLAMA	D	Asym	8	10	2.26	3.86	-0.02	5024449	5024479	GRMZM2G000489	alpha/beta-Hydrolases superfamily protein; gibberellin receptor GID1L2, putative, expressed	9909629
LH82xLAMA	D	IP	8	81	5.38	13.02	-0.51	151312347	151664188	clt1	dwarf plant	1752094
LH82xLAMA	I	GR	8	117	3.08	5.60	-0.23	172351557	172463767	GRMZM2G031724	Arabidopsis thaliana gibberellin 2-oxidase 1; gibberellin 2-beta-dioxygenase, putative, expressed	1441662
LH82xLAMA	D	GR	9	14	2.45	6.87	-0.20	5289590	6124392	GRMZM2G307440	alpha/beta-Hydrolases superfamily protein; gibberellin receptor GID1L2, putative, expressed	873137
LH82xLAMA	D	Asym	10	20	2.09	3.48	-0.02	5874629	6537612	cr4	Crinkly4; short plant	616213.5
LH82xLAMA	D	GR	10	20	2.32	6.20	0.20	5874629	6537612	cr4	Crinkly4; short plant	616213.5
LH82xLAMA	I	Asym	10	58	4.11	12.23	-0.03	136083608	136247247	GRMZM2G397684	brassinosteroid-responsive RING-H2; zinc finger, C3HC4 type domain containing protein, expressed	158067.5

Appendix A8. Continued.

Population	Trt†	Trait‡	Chr§	Position (cM)	LOD¶	PVE#	Add††	Left marker (bp)	Right marker (bp)	Closest candidate gene	Gene function	Distance from gene (bp)
LH82xLAMA	D	Asym	10	58	2.19	3.59	-0.02	136083608	136247247	GRMZM2G397684	brassinosteroid-responsive RING-H2; zinc finger, C3HC4 type domain containing protein, expressed	158067.5
Tx740xNC356	I	GR	1	167	2.19	9.24	-0.23	273833874	274877616	GRMZM5G899865	SAUR-like auxin-responsive protein family ; OsSAUR24 - Auxin-responsive SAUR gene family member, expressed	6791261
Tx740xNC356	D	IP	2	87	2.35	10.64	0.40	182727527	183505515	GRMZM2G045243	SAUR-like auxin-responsive protein family ; OsSAUR37 - Auxin-responsive SAUR gene family member, expressed	502507
Tx740xNC356	I	GR	5	119	3.01	15.02	-0.30	205748909	206263616	GRMZM2G074267	Auxin efflux carrier family protein; auxin efflux carrier component, putative, expressed	722594.5
Tx740xNC356	D	Asym	6	67	3.20	14.31	0.02	141909772	143997309	dwil1	dwarf & irregular leaf1	346506.5

† Trt: Treatment; I: Irrigated; D: Non-Irrigated.
‡ Asym: Asymptote; IP: Inflection Point; GR: Growth Rate.
§ Chr: Chromosome.
¶ LOD: $-\log_{10}$(p-value).
# PVE: Percent variation explained.
†† Additive effect estimate; Asym (m); IP (DAS); GR (DAS^{-1}).

Appendix A9. Summary of significant temporal QTL for height estimates imputed from Weibull sigmoid curve.

Population	Trt †	Chr ‡	Pos (cM)	Sig. DAS§	Peak LOD¶ DAS††	LOD ¶	PVE #	Add (m) ††	Left marker (bp)	Right marker (bp)	Closest candidate gene	Gene function	Distance from gene (bp)
LH82xLAMA	I	1	52	57-58	58	2.77	5.96	0.02	38250642	38633093	GRMZM2G331638	Auxin-responsive family protein; auxin-responsive protein-related, putative, expressed	13698348
LH82xLAMA	I	1	53	56-57	57	2.18	4.76	0.02	39742242	40356668	GRMZM2G423851	O-fucosyltransferase family protein; auxin-independent growth promoter protein, putative, expressed	13899169
Tx740xNC356	D	1	73	65-67	65	2.41	10.86	-0.02	79236413	80698058	AC204821.3_FG004	auxin response factor 10; indole-3-acetate beta-glucosyltransferase, putative, expressed	12058770
Tx740xNC356	D	1	74	64-67	67	2.32	10.43	-0.02	81440994	81549504	AC204821.3_FG004	auxin response factor 10; indole-3-acetate beta-glucosyltransferase, putative, expressed	10530756
LH82xLAMA	I	1	108	55-58	58	4.31	9.79	-0.02	198779072	198817809	GRMZM2G031065	alpha/beta-Hydrolases superfamily protein; gibberellin receptor GID1L2, putative, expressed	943009
LH82xLAMA	I	1	132	26-59	58	5.60	12.54	0.02	225044054	226136399	GRMZM2G414727	SAUR-like auxin-responsive protein family ; CPuORF40 - conserved peptide uORF-containing transcript, expressed	1217180
LH82xLAMA	I	1	134	20-59	55	5.38	13.59	0.03	229073049	229187847	GRMZM2G382393	Auxin efflux carrier family protein; auxin efflux carrier component, putative, expressed	1317326
LH82xLAMA	I	1	135	20-57	55	5.22	13.19	0.03	229187847	229850714	GRMZM2G153233	auxin response factor 16; auxin response factor 18, putative, expressed	1200114
LH82xLAMA	D	1	168	68	68	2.02	5.18	-0.02	275833355	277585472	GRMZM5G899865	SAUR-like auxin-responsive protein family ; OsSAUR24 - Auxin-responsive SAUR gene family member, expressed	0
Ki3xNC356	D	1	167	70-73	71	2.49	4.49	-0.02	298277113	298497315	AC203966.5_FG005	gibberellin 20 oxidase 2; gibberellin 20 oxidase 1, putative, expressed	1141378
Tx740xNC356	D	2	55	20-42	21	2.73	12.40	0.00	38192289	41023316	GRMZM2G121700	2-oxoglutarate (2OG) and Fe(II)-dependent oxygenase superfamily protein; gibberellin 20 oxidase 2, putative, expressed	1414534
Ki3xNC356	D	2	67	48-69	61	2.59	5.32	-0.01	80271334	80586731	GRMZM5G848945	auxin signaling F-box 3; OsFBL16 - F-box domain and LRR containing protein, expressed	15391130
Ki3xNC356	D	2	68	51-67	66	2.29	4.65	-0.01	83187294	87042364	GRMZM2G451037	SAUR-like auxin-responsive protein family ; OsSAUR4 - Auxin-responsive SAUR gene family member, expressed	19614474
LH82xLAMA	I	2	117	32-43	37	2.28	5.14	0.00	212246084	212544633	GRMZM2G064941	Auxin efflux carrier family protein; auxin efflux carrier component, putative, expressed	254541
LH82xLAMA	D	2	124	63-65	64	2.16	5.96	0.02	217637431	219258619	GRMZM2G062019	carboxyesterase 18; gibberellin receptor GID1L2, putative, expressed	708484
LH82xLAMA	I	3	62	20-47	37	2.59	6.30	0.00	140845175	142249525	GRMZM2G116204	endoplasmic reticulum auxin binding protein 1; auxin-binding protein 4 precursor, putative, expressed	7656087
LH82xLAMA	D	3	72	77-85	85	2.08	5.31	0.02	158668137	159817878	sdw2	short plant	830010
LH82xLAMA	D	3	96	69-85	70	2.18	5.53	0.02	176562816	177536662	na1	dwarf plant	1942864

Appendix A9. Continued.

Population	Trt †	Chr ‡	Pos (cM)	Sig. DAS§	Peak LOD¶ DAS††	LOD ¶	PVE #	Add (m) ††	Left marker (bp)	Right marker (bp)	Closest candidate gene	Gene function	Distance from gene (bp)
Ki3xNC356	I	4	61	63-85	82	5.03	10.29	0.03	156384593	156517564	GRMZM2G134023	brassinosteroid-responsive RING-H2; zinc finger, C3HC4 type domain containing protein, expressed	259337
Ki3xNC356	I	4	62	63-69	69	4.13	8.45	0.02	156998152	157879556	GRMZM2G134023	brassinosteroid-responsive RING-H2; zinc finger, C3HC4 type domain containing protein, expressed	1247112
Ki3xNC356	D	4	104	65-67	67	2.23	4.54	0.01	218940880	219145633	GRMZM2G326114	2-oxoglutarate (2OG) and Fe(II)-dependent oxygenase superfamily protein; gibberellin 20 oxidase 2, putative, expressed	15224555
Ki3xNC356	I	4	120	48-54	52	2.11	4.40	-0.01	237391404	237610499	AC196708.3_FG006	SAUR-like auxin-responsive protein family ; OsSAUR5 - Auxin-responsive SAUR gene family member, expressed	187125
LH82xLAMA	I	5	17	21-52	39	2.65	6.48	-0.01	5105202	5211414	GRMZM2G130675	SAUR-like auxin-responsive protein family ; OsSAUR1 - Auxin-responsive SAUR gene family member, expressed	91525
Ki3xNC356	D	5	36	63-65	64	2.11	4.06	0.01	17344330	18452570	GRMZM2G060940	2-oxoglutarate (2OG) and Fe(II)-dependent oxygenase superfamily protein; gibberellin 20 oxidase 2, putative, expressed	273100
Ki3xNC356	I	5	38	63	63	2.08	4.33	0.01	21893133	21893252	GRMZM2G113135	SAUR-like auxin-responsive protein family ; CPuORF40 - conserved peptide uORF-containing transcript, expressed	1105270
Ki3xNC356	D	5	68	54-57	56	2.02	3.95	0.01	170416302	171276656	GRMZM2G702026	auxin response factor 1; auxin response factor 7, putative, expressed	2961382
Tx740xNC356	I	5	118	24-63	63	2.19	9.94	0.02	204585691	205239681	GRMZM5G885274	GRAS family transcription factor; gibberellin response modulator protein, putative, expressed	171258
Tx740xNC356	I	5	119	23-63	56	4.90	20.89	0.03	205748909	206263616	GRMZM2G074267	Auxin efflux carrier family protein; auxin efflux carrier component, putative, expressed	722595
Tx740xNC356	D	6	0	54-64	60	2.62	11.66	0.02	1338837	3573312	GRMZM2G070500	nodulin MtN21 /EamA-like transporter family protein; auxin-induced protein 5NG4, putative, expressed	37898001
Tx740xNC356	I	6	30	64-65	65	2.30	10.48	0.02	94418426	95940965	GRMZM2G462760	SAUR-like auxin-responsive protein family ; OsSAUR25 - Auxin-responsive SAUR gene family member, expressed	2782579
Tx740xNC356	I	6	35	64-74	68	2.53	11.40	0.02	96558982	96880264	GRMZM2G462760	SAUR-like auxin-responsive protein family ; OsSAUR25 - Auxin-responsive SAUR gene family member, expressed	4322506
Tx740xNC356	D	6	67	64-85	84	3.20	14.11	0.02	141909772	143997309	dwil1	dwarf & irregular leaf1	346507
Tx740xNC356	I	6	75	42-62	56	2.50	9.25	0.02	154194879	154326722	GRMZM2G140805	nodulin MtN21 /EamA-like transporter family protein; auxin-induced protein 5NG4, putative, expressed	1385932

Appendix A9. Continued.

Population	Trt †	Chr ‡	Pos (cM)	Sig. DAS§	Peak LOD¶ DAS††	LOD ¶	PVE #	Add (m) ††	Left marker (bp)	Right marker (bp)	Closest candidate gene	Gene function	Distance from gene (bp)
Tx740xNC356	I	6	76	51-62	62	2.28	9.12	0.02	154345260	155647497	GRMZM2G140805	nodulin MtN21 /EamA-like transporter family protein; auxin-induced protein 5NG4, putative, expressed	650354
Ki3xNC356	D	7	23	72-73	73	6.46	11.68	0.03	13980271	14905605	GRMZM2G320298	alpha/beta-Hydrolases superfamily protein; gibberellin receptor GID1L2, putative, expressed	7324200
Ki3xNC356	D	7	27	74-85	85	13.02	24.16	0.04	25781951	26153406	GRMZM2G075715	auxin response factor 6; auxin response factor, putative, expressed	13766771
Ki3xNC356	D	7	32	71-85	85	21.42	44.01	-0.05	95447274	96847624	GRMZM2G391795	alpha/beta-Hydrolases superfamily protein; gibberellin receptor GID1L2, putative, expressed	11778171
Ki3xNC356	D	8	3	64-85	85	3.58	6.08	-0.02	2792594	2901121	GRMZM2G000489	alpha/beta-Hydrolases superfamily protein; gibberellin receptor GID1L2, putative, expressed	12087236
LH82xLAMA	D	8	10	72-85	85	2.26	6.08	-0.02	5024449	5024479	GRMZM2G000489	alpha/beta-Hydrolases superfamily protein; gibberellin receptor GID1L2, putative, expressed	9909629
LH82xLAMA	D	8	84	35-43	43	3.08	8.40	0.01	157963615	157970345	GRMZM2G116557	auxin response factor 2; auxin response factor, putative, expressed	2134364
LH82xLAMA	D	8	96	51-61	54	4.26	11.35	0.03	165542954	165556999	GRMZM2G431066	SAUR-like auxin-responsive protein family ; OsSAUR24 - Auxin-responsive SAUR gene family member, expressed	349596
LH82xLAMA	D	8	97	44-50	50	3.97	10.62	0.02	166105809	166240043	GRMZM2G431066	SAUR-like auxin-responsive protein family ; OsSAUR24 - Auxin-responsive SAUR gene family member, expressed	972545
LH82xLAMA	D	9	14	24-34	24	2.23	5.71	0.00	5289590	6124392	GRMZM2G307440	alpha/beta-Hydrolases superfamily protein; gibberellin receptor GID1L2, putative, expressed	873137
LH82xLAMA	D	9	84	69-71	69	2.17	5.18	-0.02	139931280	139961881	GRMZM2G031447	carboxyesterase 17; gibberellin receptor GID1L2, putative, expressed	1592902
LH82xLAMA	I	9	94	61-62	62	2.28	5.68	-0.02	145282309	145505072	GRMZM2G028039 _gras45	GRAS family transcription factor; gibberellin response modulator protein, putative, expressed	3773603
LH82xLAMA	D	10	20	44-85	44	2.13	5.59	-0.01	5874629	6537612	cr4	Crinkly4; short plant	616214
LH82xLAMA	D	10	22	44-50	44	2.31	6.21	-0.01	5874629	6537612	cr4	Crinkly4; short plant	616214
LH82xLAMA	D	10	23	44-50	44	2.26	5.81	-0.01	5874629	6537612	cr4	Crinkly4; short plant	616214
LH82xLAMA	D	10	26	24-50	24	2.50	6.84	0.00	8451245	10196681	GRMZM2G346110	SAUR-like auxin-responsive protein family ; OsSAUR15 - Auxin-responsive SAUR gene family member	663550
LH82xLAMA	D	10	45	45-64	64	2.09	5.75	-0.02	82042041	82850420	GRMZM2G072632	Auxin efflux carrier family protein; auxin efflux carrier component, putative, expressed	7838586

Appendix A9. Continued.

Population	Trt †	Chr ‡	Pos (cM)	Sig. DAS Int. §	Peak DAS #	Peak LOD ¶	Peak PVE ††	Peak Add ‡‡	Left marker (bp)	Right marker (bp)	Closest candidate gene	Gene function	Distance from gene (bp)
LH82xLAMA	I	10	46	51-60	58	4.72	10.43	-0.02	88270397	88401043	GRMZM2G072632	Auxin efflux carrier family protein; auxin efflux carrier component, putative, expressed	1949096
LH82xLAMA	I	10	47	61-62	62	4.65	12.75	-0.02	92823460	95666918	GRMZM2G072632	Auxin efflux carrier family protein; auxin efflux carrier component, putative, expressed	3960373
LH82xLAMA	D	10	48	62-66	62	2.60	7.07	-0.02	99931137	101933970	GRMZM2G137451	auxin signaling F-box 2; OsFBL16 - F-box domain and LRR containing protein, expressed	10066214
LH82xLAMA	D	10	51	33-66	34	2.54	7.08	0.00	127261630	127988227	GRMZM2G007481	Auxin efflux carrier family protein; auxin efflux carrier component, putative, expressed	828343
LH82xLAMA	D	10	57	23-85	27	2.55	6.96	0.00	135609157	136083608	GRMZM2G397684	brassinosteroid-responsive RING-H2; zinc finger, C3HC4 type domain containing protein, expressed	160978
LH82xLAMA	I	10	58	63-85	64	4.38	12.29	-0.03	136083608	136247247	GRMZM2G397684	brassinosteroid-responsive RING-H2; zinc finger, C3HC4 type domain containing protein, expressed	158068
LH82xLAMA	D	10	58	23-85	27	2.46	6.80	0.00	136083608	136247247	GRMZM2G397684	brassinosteroid-responsive RING-H2; zinc finger, C3HC4 type domain containing protein, expressed	158068
LH82xLAMA	D	10	65	20-22	20	2.65	7.22	0.00	140049011	140268347	GRMZM2G456644	SAUR-like auxin-responsive protein family ; OsSAUR20 - Auxin-responsive SAUR gene family member, expressed	1394099

† Trt: Treatment; I: Irrigated; D: Non-Irrigated.
‡ Chr: Chromosome.
§ Day interval where the QTL has a LOD>2 and PVE>3.
# Day which QTL has the greatest LOD score within the significant day interval.
¶ LOD: $-\log_{10}$(p-value).
†† PVE: Percent variance explained.
‡‡ Additive effect estimate (m).

APPENDIX B

SUPPLEMENTAL FIGURES

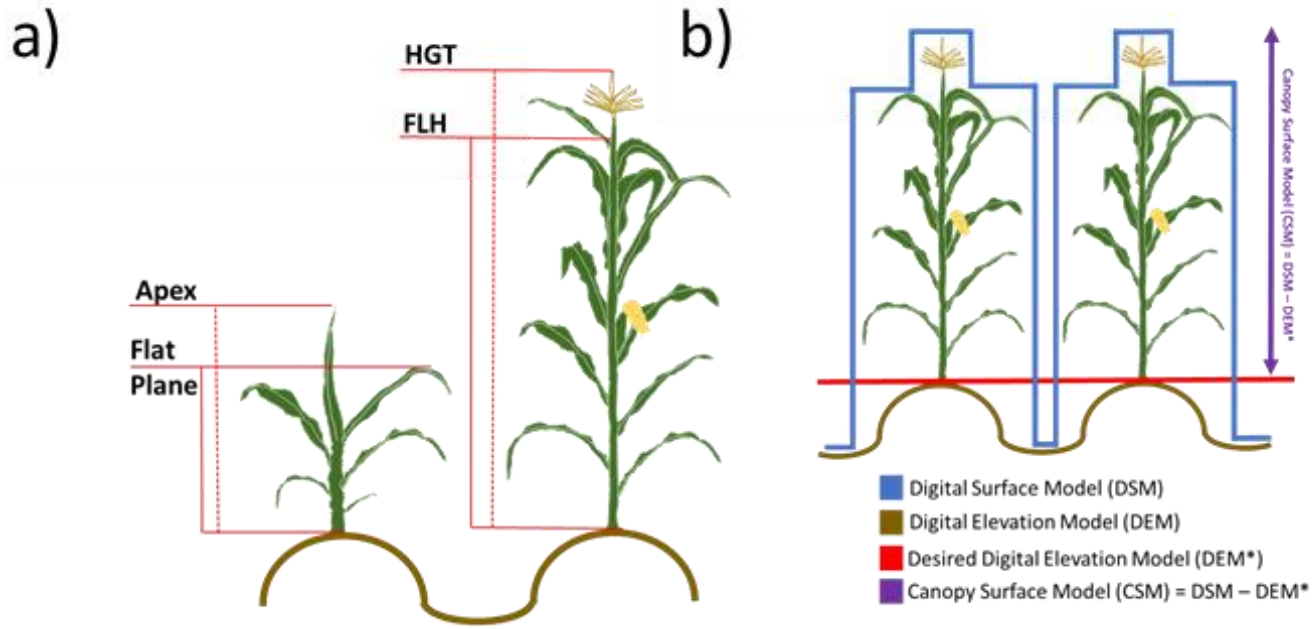

Appendix B1. [a] Illustration of locations in which manual height measurements were collected during vegetative (left) and reproductive (right) growth periods in maize from the top of the planted rows, separated by furrows. **[b]** Diagram demonstrating the different elevation models and what they are intended to model.

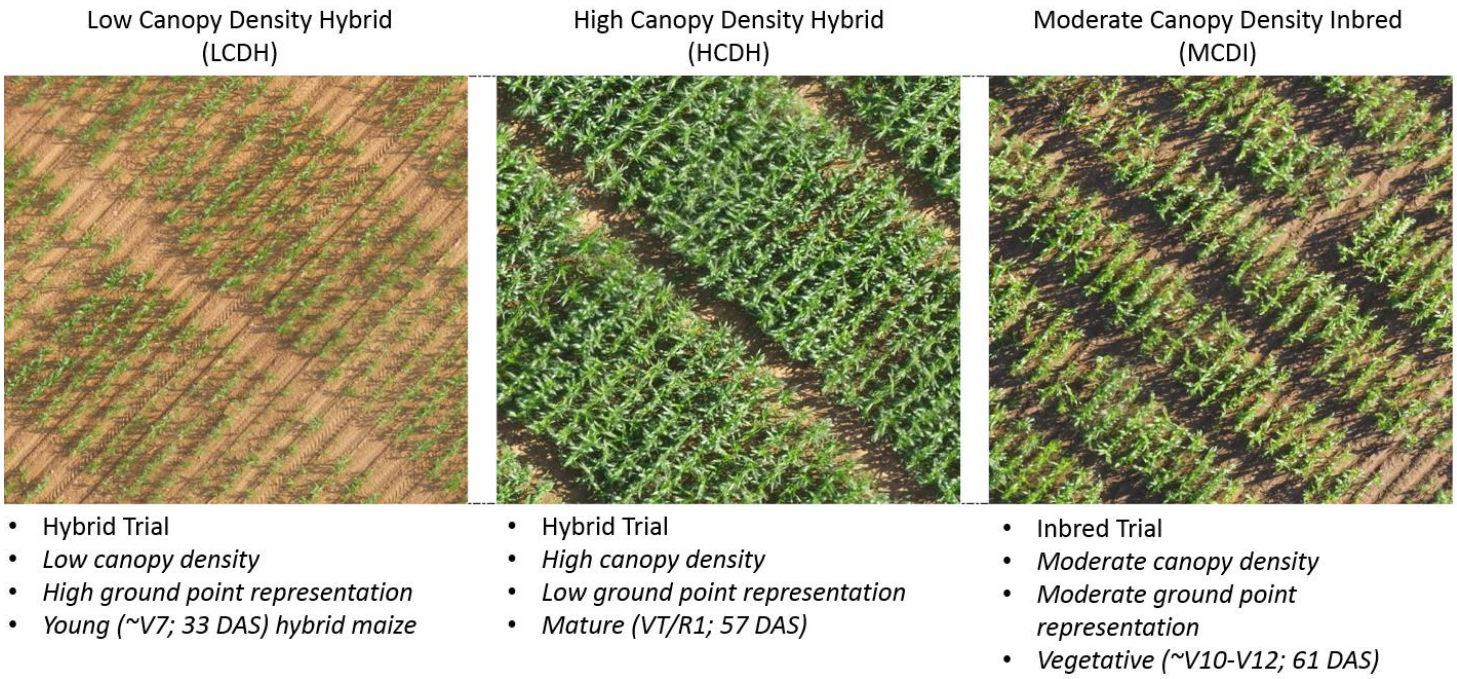

Appendix B2. Descriptions of study sites for comparison of ground filtering methods.

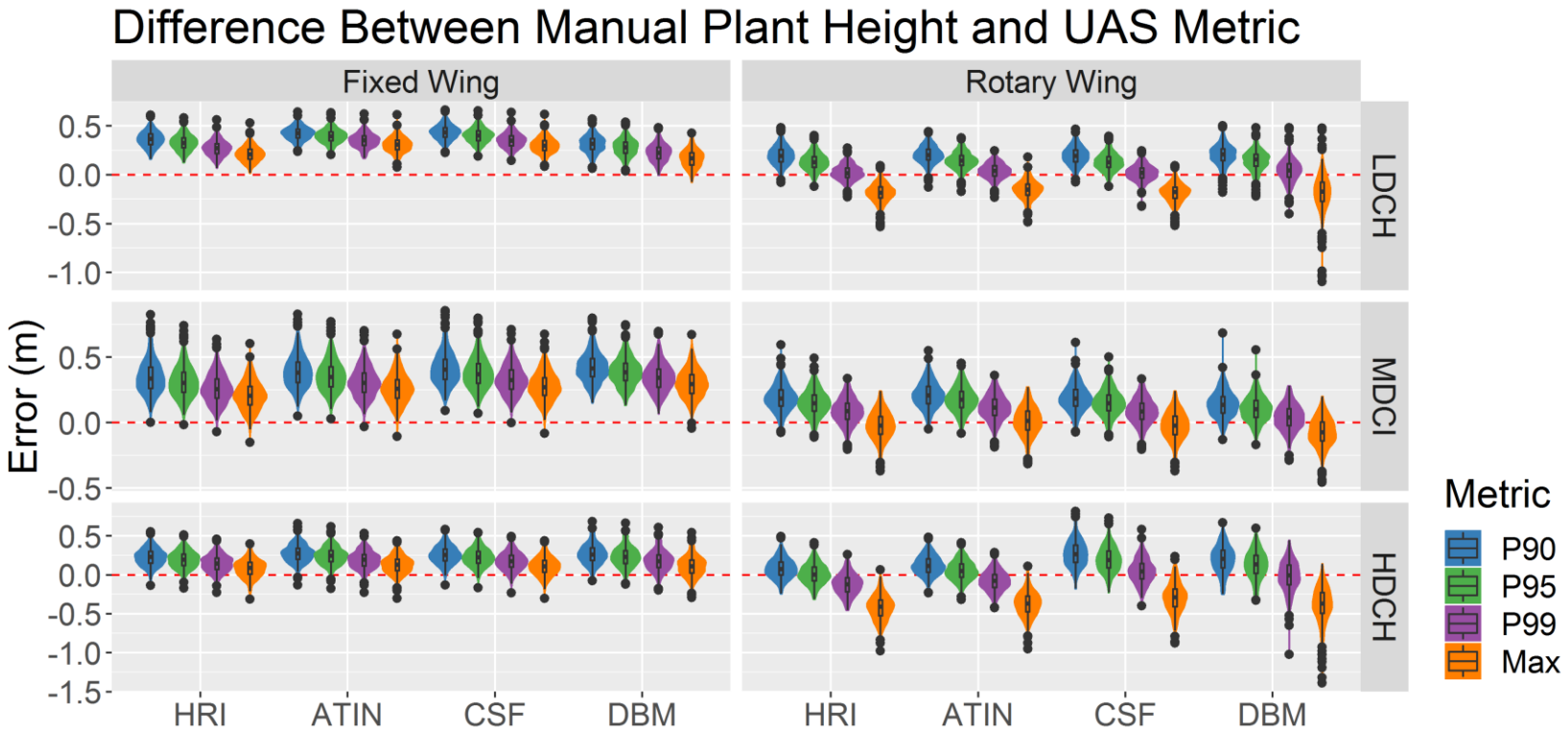

Appendix B3. Violin plots comparing distribution of the difference between ground truth measurements and UAS height metrics (PHT – UAS) across UAS platforms (fixed wing and rotary wing) and study sites (LCDH: Low Canopy Density Hybrids, MCDI: Medium Canopy Density Inbred, and HCDH: High Canopy Density Hybrids) for each of the ground filtering methods (HRI: Hierarchical Robust Interpolation, ATIN: Adaptive Triangulated Irregular Network, CSF: Cloth Simulation Filter, DBM: Difference Based Method). Violin plots provide summary statistics typical of boxplot accompanied with a visualization of the probability density of the data. Red dashed line indicates zero error.

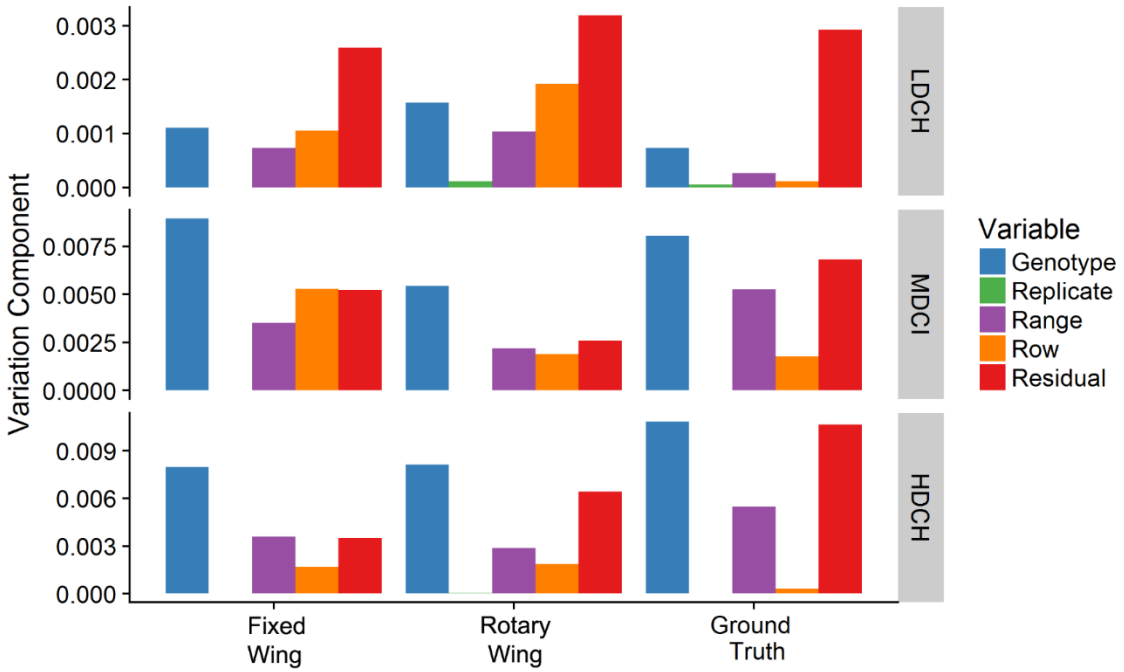

Appendix B4. Comparison of variance component estimates between UAS platforms (fixed wing and rotary wing) and terminal ground truth plant height (ground truth) across study sites (LCDH: Low Canopy Density Hybrids), MCDI: Medium Canopy Density Inbred, and HCDH: High Canopy Density Hybrids).

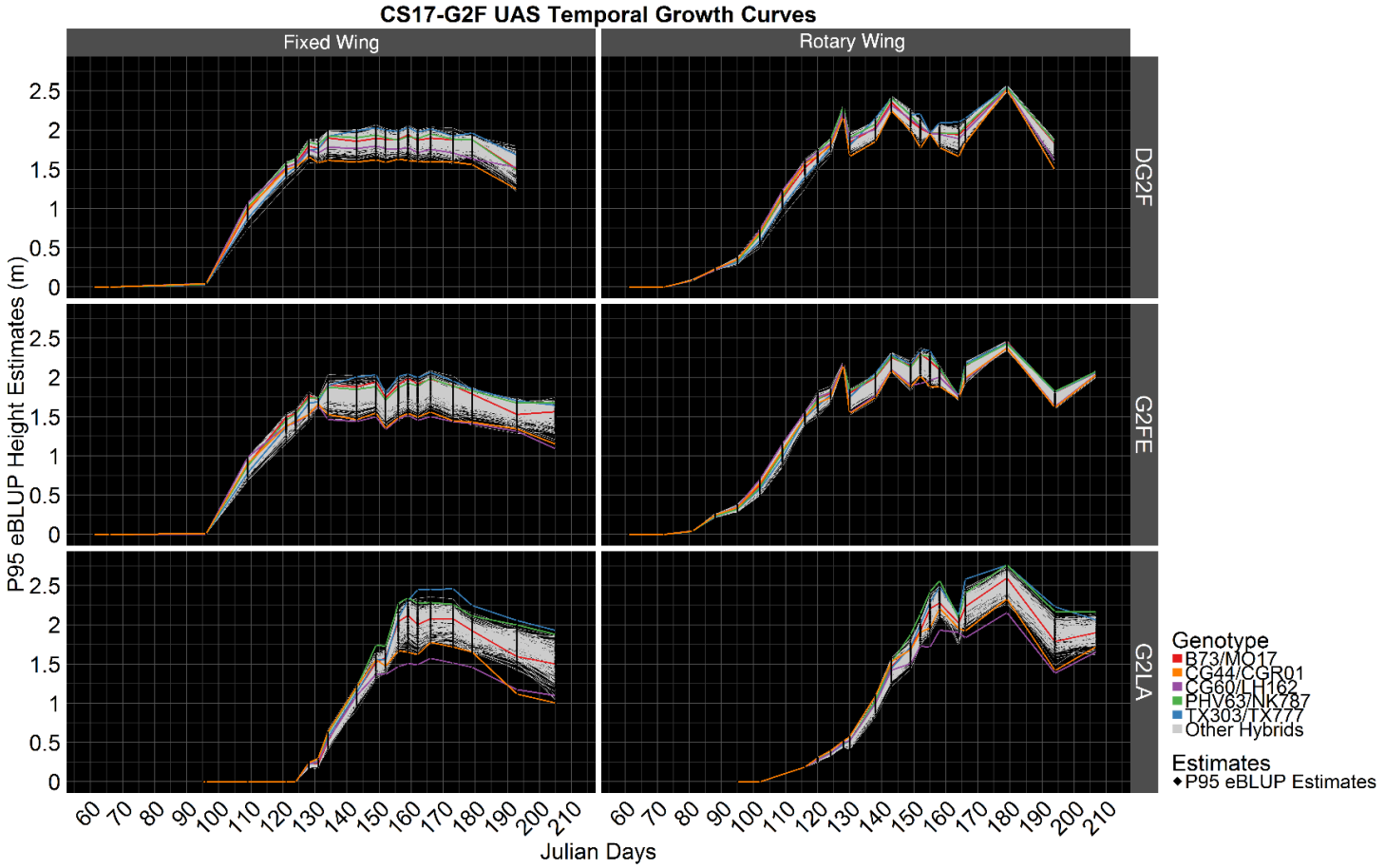

Appendix B5. Temporal growth models of the P95 pedigree BLUPS by UAS platform (fixed wing and rotary wing) and trials (DG2F: Optimal planted, D trial; G2FE: Optimal planted, irrigated trial; G2LA: Delay planted, irrigated trial) of the 2017 G2F trials in College Station, TX. All flight dates are independent by Julian day and connecting lines are for visualization purposes to follow the growth pattern of specific pedigrees.

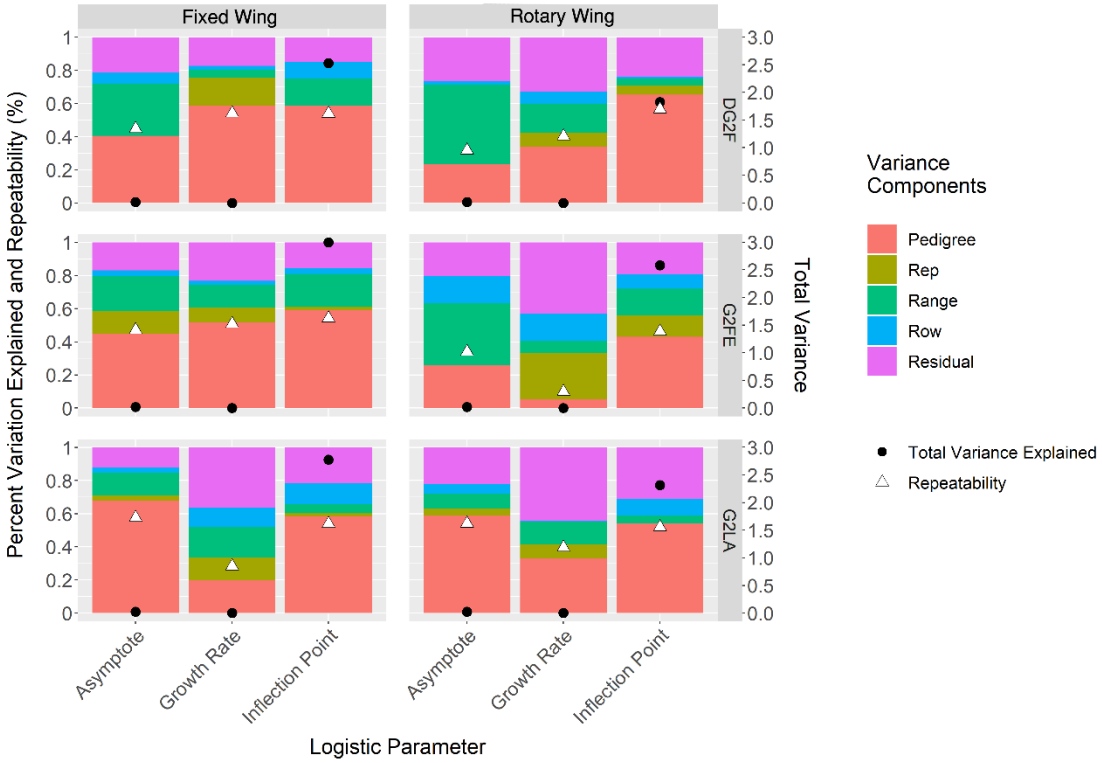

Appendix B6. Stack bar graphs of percent variation explained by variables of Eq. 3 for logistic curve parameter for individual UAS platforms (fixed wing and rotary wing) and experimental trials (DG2F: Optimal planted, D trial; G2FE: Optimal planted, irrigated trial; G2LA: Delay planted, irrigated trial). Total variance captured (black circle) per image set, defined by the right y-axis, puts repeatability and genetic variance explained into perspective of other flight dates. Repeatability is indicated by the white triangles.

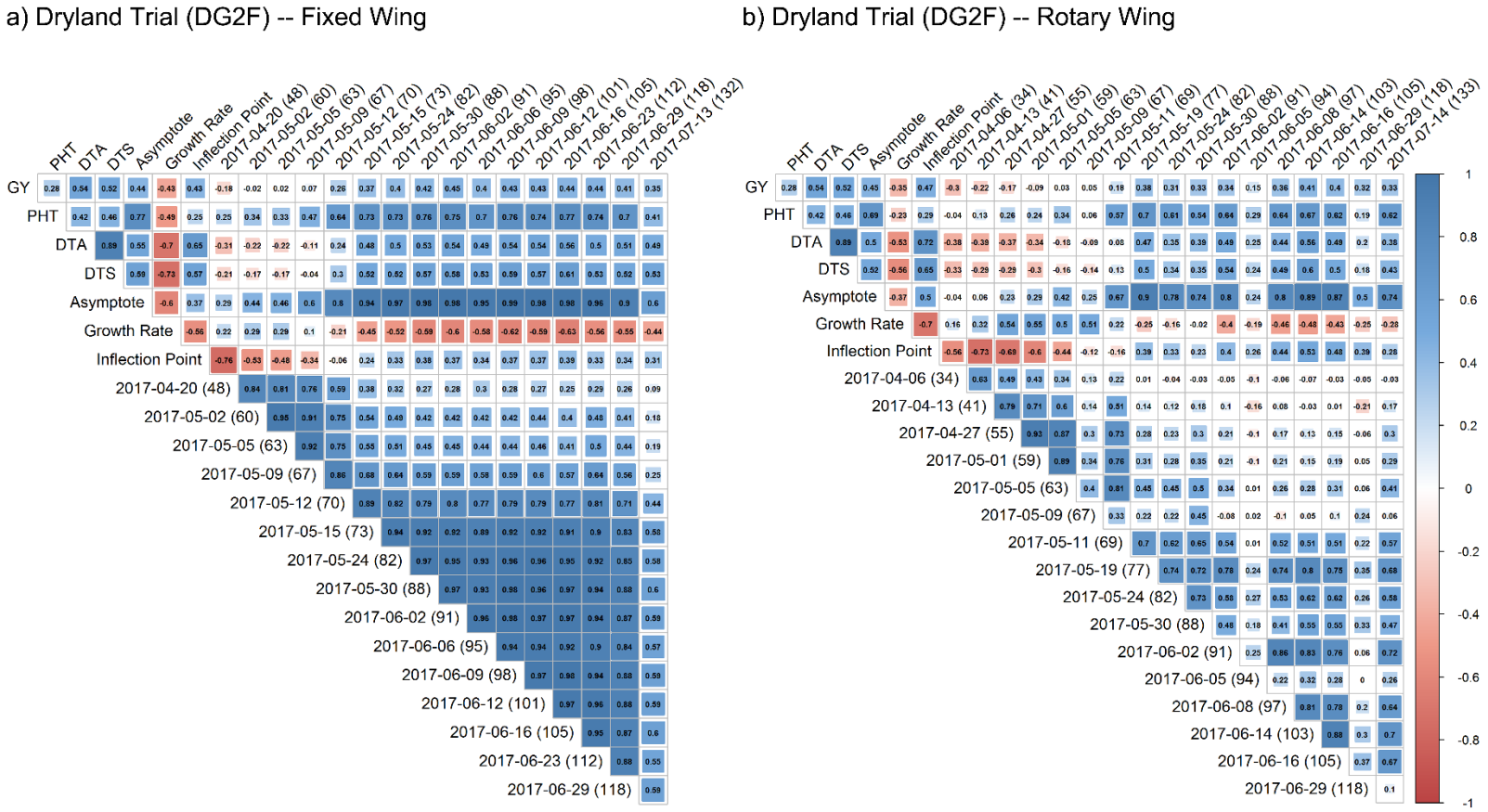

Appendix B7. Heat map comparing correlations between grain yield (GY), manual terminal plant height (PHT), flowering time (DTA/DTS), logistic parameters (asymptote, growth rate, inflection point), and UAS P95 estimates by flight date for the DG2F trial surveyed by the [a] fixed wing and [b] rotary wing.

a) Irrigated Optimal Trial (G2FE) -- Fixed Wing

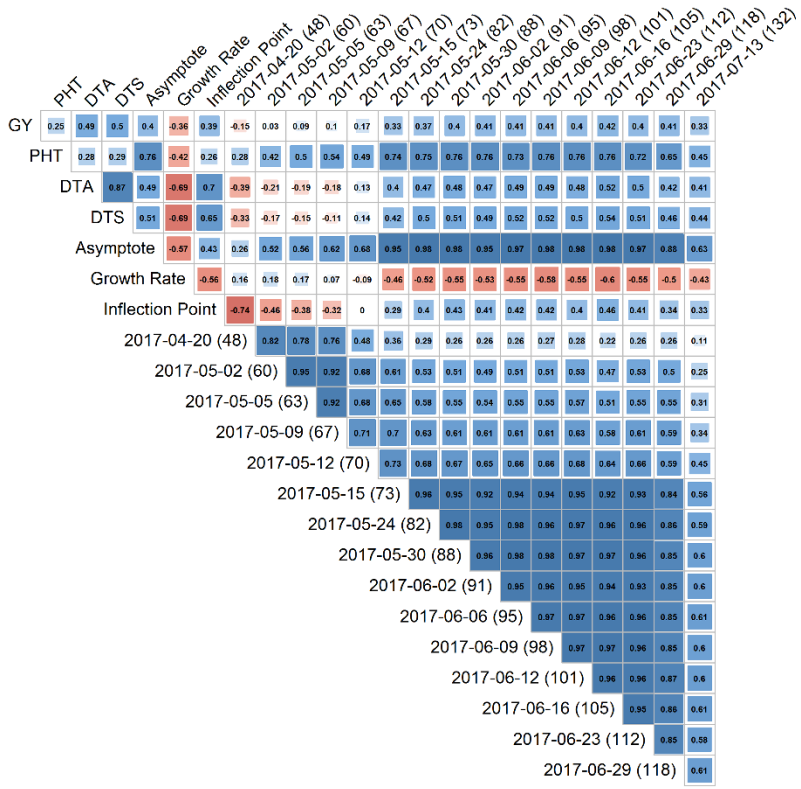

b) Irrigated Optimal Trial (G2FE) -- Rotary Wing

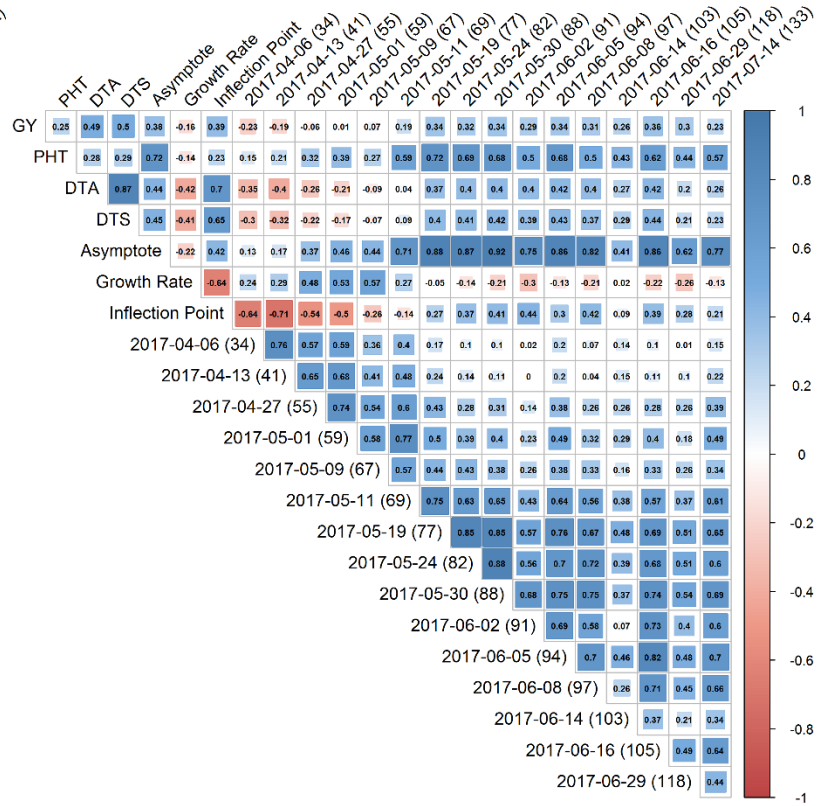

Appendix B8. Heat map comparing correlations between grain yield (GY), manual terminal plant height (PHT), flowering time (DTA/DTS), logistic parameters (asymptote, growth rate, inflection point), and UAS P95 estimates by flight date for the G2FE trial surveyed by the **[a]** fixed wing and **[b]** rotary wing.

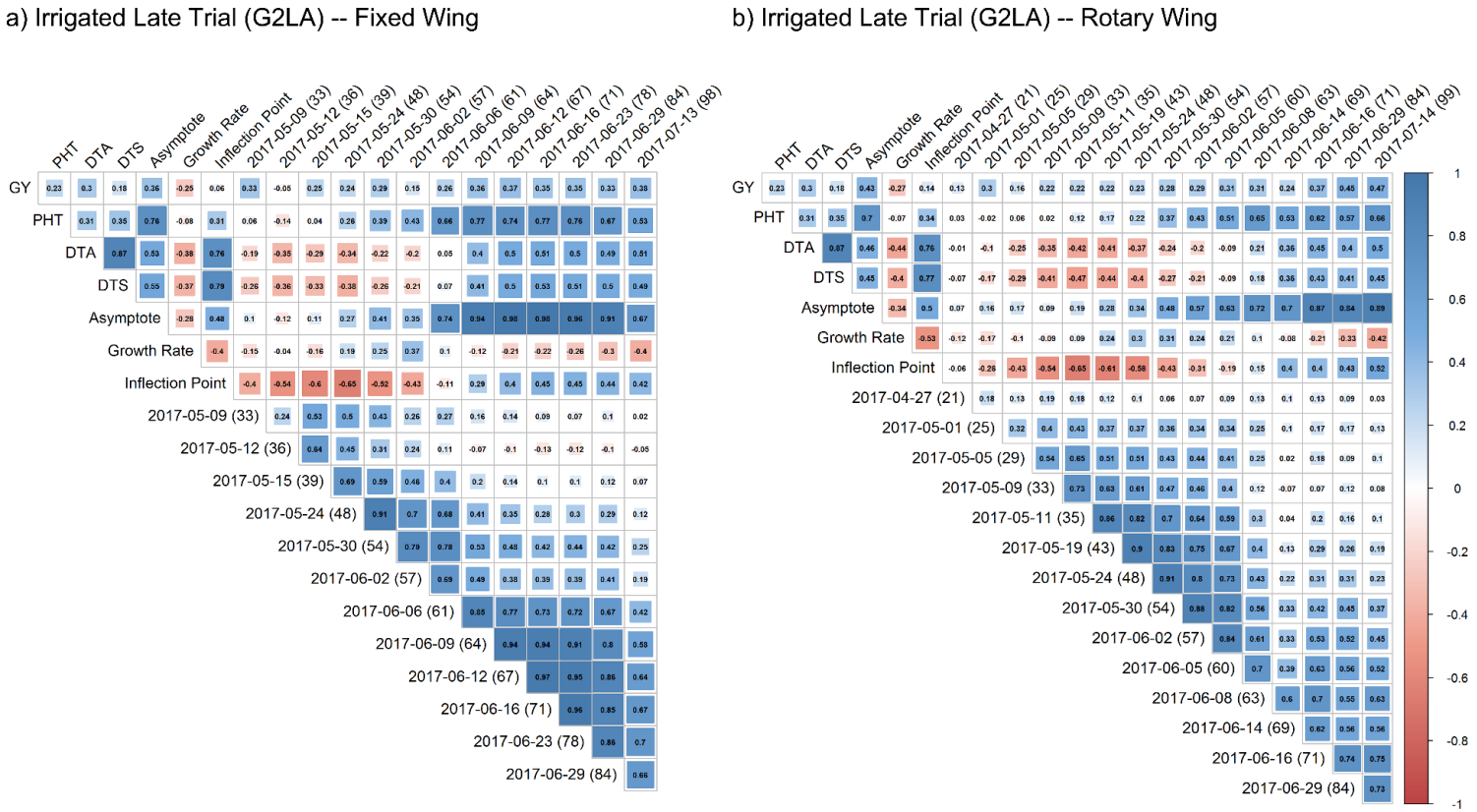

Appendix B9. Heat map comparing correlations between grain yield (GY), manual terminal plant height (PHT), flowering time (DTA/DTS), logistic parameters (asymptote, growth rate, inflection point), and UAS P95 estimates by flight date for the G2LA trial surveyed by the **[a]** fixed wing and **[b]** rotary wing.

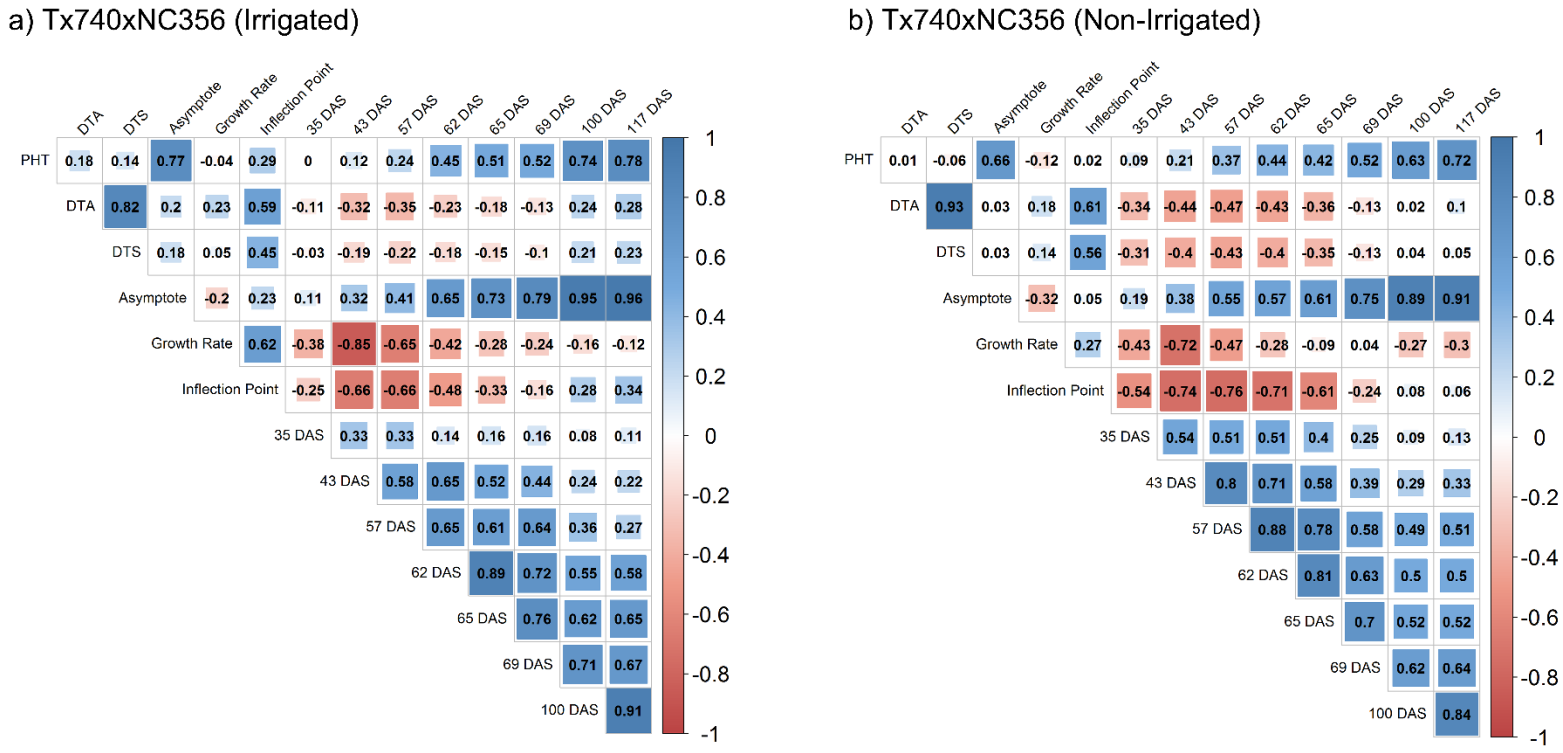

Appendix B10. Heat map comparing correlations between manual terminal plant height (PHT), flowering time (DTA/DTS), functional parameters (asymptote, growth rate, inflection point), and UAS P95 estimates by flight date for the Tx740xNC356 population under **[a]** irrigated and **[b]** non-irrigated watering regimens.

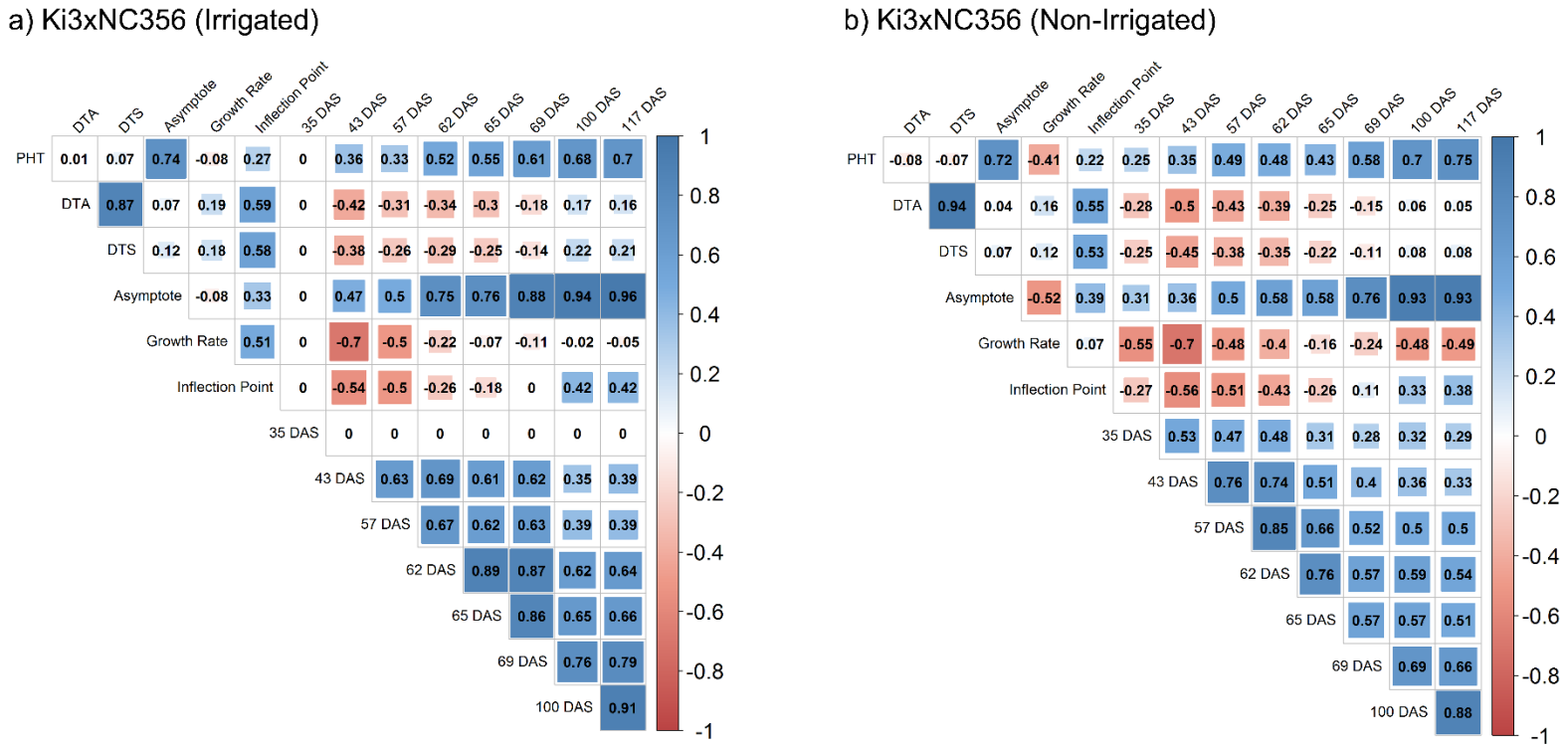

Appendix B11. Heat map comparing correlations between manual terminal plant height (PHT), flowering time (DTA/DTS), functional parameters (asymptote, growth rate, inflection point), and UAS P95 estimates by flight date for the Ki3xNC356 population under **[a]** irrigated and **[b]** non-irrigated watering regimens.

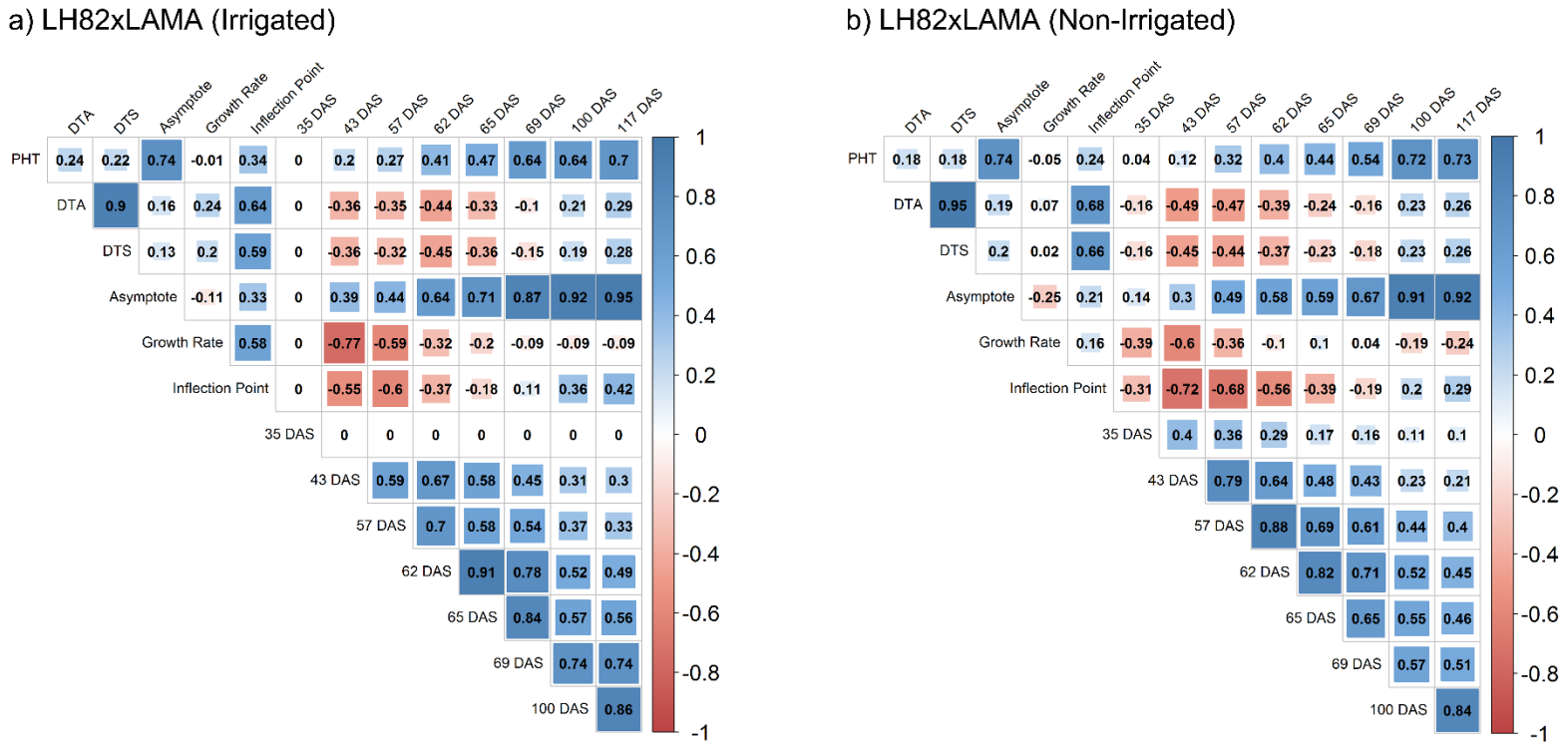

Appendix B12. Heat map comparing correlations between manual terminal plant height (PHT), flowering time (DTA/DTS), functional parameters (asymptote, growth rate, inflection point), and UAS P95 estimates by flight date for the LH82xLAMA population under **[a]** irrigated and **[b]** non-irrigated watering regimens.

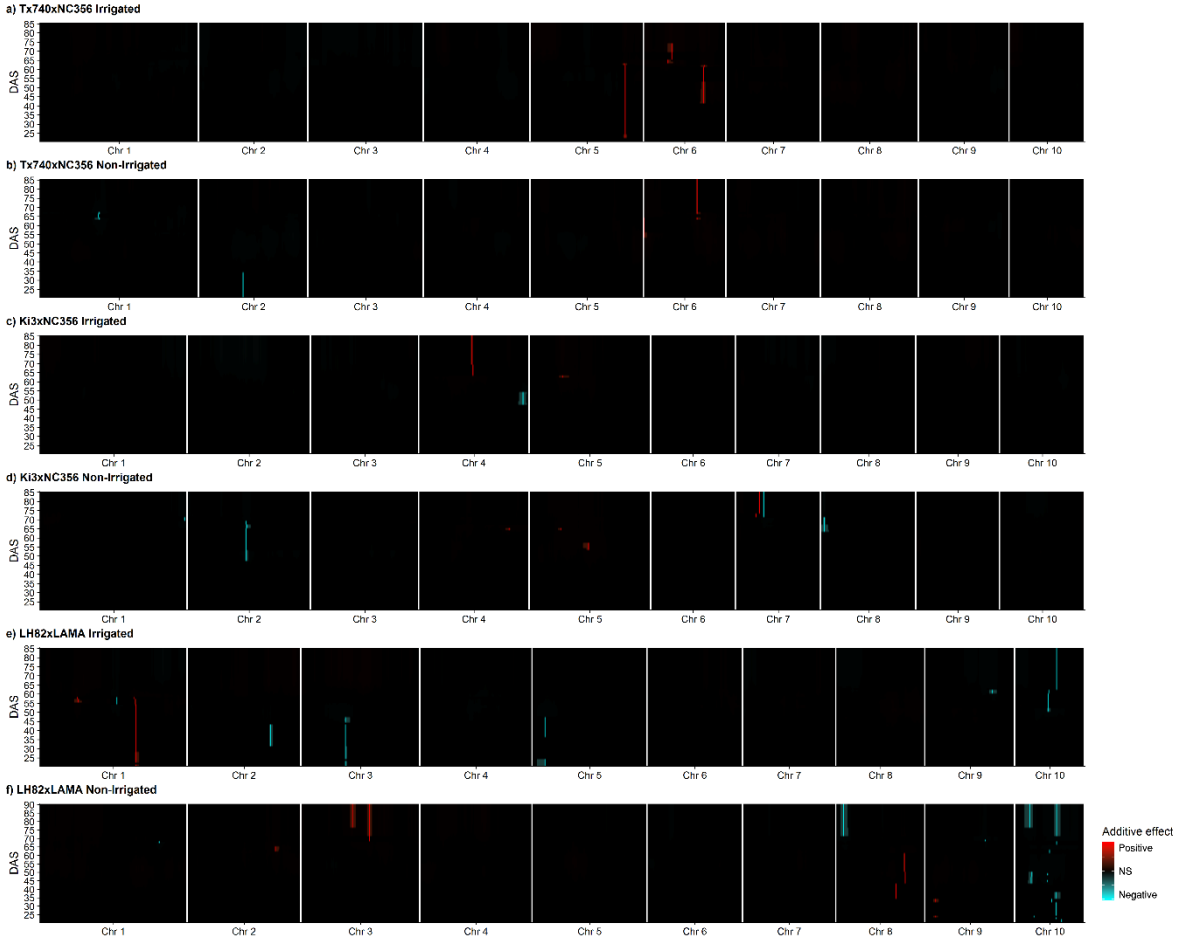

Appendix B13. Significant temporal height QTL. Red indicates positive allelic effect estimates, blue indicates negative allelic effect estimates, and black indicate non-significant (NS) genomic regions.

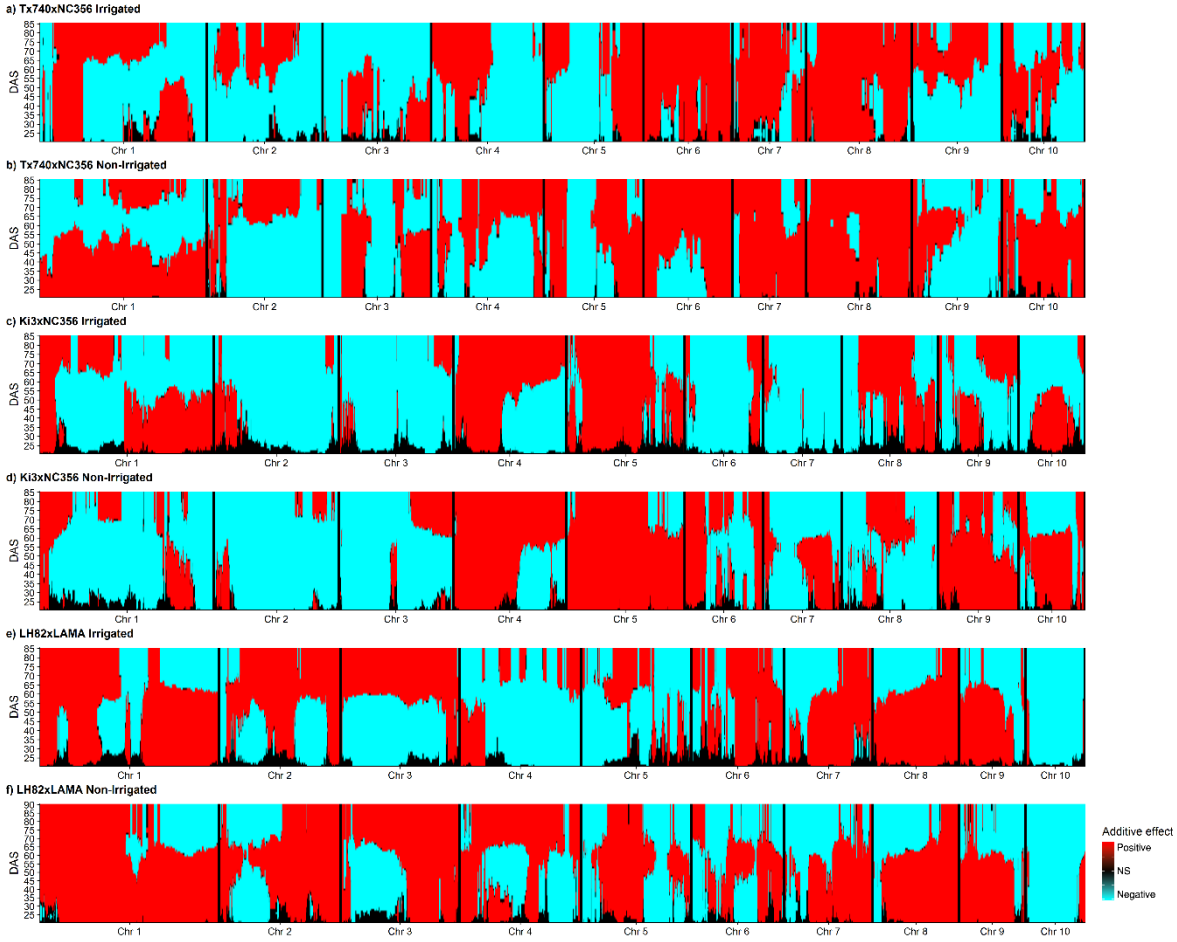

Appendix B14. Visual representation of temporal single marker analysis of the Weibull imputed height estimates.

APPENDIX C

SUPPLEMENTAL MATERIALS AND METHODS

Appendix C1. Description of point cloud based ground filtering algorithms.

Hierarchical Robust Interpolation (HRI)

The hierarchical robust interpolation (HRI) algorithm (GroundFilter.exe) implemented in FUSION/LDV (McGaughey, 2009) software utilizes linear least-squares with equal point weighting to define the initial surface followed by adaptive weight functions of the residual distances from the surface model to iteratively fine tune refine the ground points (Kraus and Pfeifer, 2001; Kraus and Rieger, 1999). The HRI begins by equally weighting all of the points as one, followed by the interpolation of an intermediate surface based on all of the points. Utilizing the shift parameters (g & w) point are assigned a weight between zero (object) and one (ground). Points lying (g) below the intermediate surface are assigned a weight of one, point's with residuals (g + w) above the intermediate surface are

Appendix C1 Table 1. Optimized parameters for HRI ground filter based on minimization of absolute error between UAS height estimates and manual measured height.

Parameters	Rotary wing	Fixed wing
Cell size (m)	25	25
g (m)	-0.25	-0.25
g + w (m)	0.1	0.1
a	1	1
b	25	25

assigned weighs of zero and excluded from the next iterative interpolation of an intermediate surface. All intermediate point are assigned weights based on their distance from the

intermediate surface. After the final iteration all remaining point with weights less than one are classified as ground points. Parameter "b" can be adjusted to set the steepness of the weight function and parameter "a" shifts the weight function.

Cloth Simulation Filter (CSF)

The cloth simulation filter (CSF) (Zhang, et al., 2016) was implemented within R via the RCSF package (https://github.com/Jean-Romain/RCSF). A flat surface (i.e. cloth) is place upon the surface of the inverted point cloud and the shape of the cloth is adjusted based on intersections between the cloth points and the point cloud points, generating an approximation of the ground surface. The CSF has f iveparameters that must be set: grid resolution of the cloth grid (GR), time step (*d*T), cloth rigidness (RI), post processing slope smoothing (ST), and classification threshold (h_{cc}). The *d*T was left at 0.65 as advised by

Appendix C1 Table 2. Optimized parameters for CSF ground filter based on minimization of absolute error between UAS height estimates and manual measured height.

Parameters	Rotary wing	Rotary wing	Fixed wing	Fixed wing
Grid rigidness	1L	1L	1L	1L
Cloth resolution (m)	1	25	1	25
Class threshold (m)	0.1	0.5	0.1	0.1
Time step	0.65	0.65	0.65	0.65
Rigidness	1	1	1	1

the creator of the CSF due to the minimization of classification error. The RI was set to three for flat terrains and the ST was set to false, as our agricultural study site is flat and lacks large elevation shifts. Optimization of the CSF was complete through iteration of the of the h_{cc} and GR parameters.

Adaptive Triangulated Irregular Network (ATIN)

The adaptive triangulated irregular network (ATIN) (Axelsson, 1999) was implemented within the LAStools (Isenburg, 2015) software suite with the LASground script. The algorithm first generates a TIN face below the point cloud by sub-randomly distributed local minimum points. Using threshold parameters, the surface is iteratively densified if the point lies within the filtering parameters: step size, offset, bulge, spike, and standard deviation. The standard deviation was set to zero to help reduce algorithm inconsistencies (i.e. algorithm doesn't classify points effectively). The spike param`eter

Appendix C1 Table 3. Optimized parameters for ATIN ground filter based on minimization of absolute error between UAS height estimates and manual measured height.

Parameters	Rotary wing	Fixed wing
Step size (m)	25	25
Bulge (m)	0	0
Offset (m)	0.5	0.2
Spike	0.05	0.05
Std. Dev.	0	0

was set to 0.05 m to remove low vegetation from the ground classification. Iterative tuning of the step size, offset, and bulge parameters were evaluated to set the optimal parameters (Supplemental 3 Table S3).

Discussion on Tuning of Filtering Algorithms

In general, preference was set to cell size of 25 meters to find parameters that performed consistently across varying levels of ground point representation. With plots sizes ranging from 3.8 to 7.6 meters, a cell size of 25 meters ensured that whole plots are evaluated in the filtering algorithms and not mistakenly represented as ground while also being large

enough to have adequate ground representation with the cell in the high canopy density point clouds.

The CSF algorithm is computationally efficient and requires four parameters (cloth resolution, class threshold, time step, and rigidness) to be implemented. Our results suggest that adjustments to the cloth resolution as the density of ground points is necessary to obtain adequate ground filtering. The CSF is simple to implement, but is highly affected by negative blunders as it creates the cloth mesh on the bottom of the point cloud.

Like CSF, the ATIN method is highly affected by negative blunders when randomly sampling the minimum points within a cell as the seed points to begin building the TIN. The relative inefficiency of the ATIN combined with the large number of parameters (offset, bulge, spike, and standard deviation) made optimizing this algorithm time intensive and unfavorable. Our results indicate that blunders should not be present at distance greater that the upward spike parameter to ensure that the coarsest TIN can incorporate representative ground points. The LASground documentation indicates that fine tuning the bulge algorithms can result in highly accurate ground representation, but we did not see any improvement from including bulge parameters.

In contrast, the HRI algorithms progressively creates surface models based on the average of the points in question, which means the algorithms works from the top down. This has significant impact in reducing the effect of positive and negative blunders on the algorithms performance. The HRI requires four parameters to be tuned (g, w, a, and b) and is computationally superior to ATIN. The greater the b parameter the greater the slope of the weight function resulting in stricter definition of ground versus no ground points. The a-parameter has little effect on the weight function and can be set to the default value in most

situations. The g-parameter, should be large enough to progressively work through the canopy within the allotted iterations, but the w-parameter seems to be the most important of the parameters as it defines the distance above the intermediate surface in which points can be considered ground. This has a significant impact upon the differentiating low growth vegetation from ground and can greatly improve your early season height estimates.